Ultra-Coherent Electro-Mechanics in the Quantum Regime

by

Yannick Seis

Niels Bohr Institute
Faculty of Science
University of Copenhagen
Denmark

This thesis has been submitted to the PhD School of Science at the University of Copenhagen.
October 2021

Academic Supervisor:	Prof. Albert Schließer
External referees:	Prof. Gary Steele Assoc. Prof. Samuel Deléglise
Local referee:	Assoc. Prof. Ferdinand Kuemmeth
Thesis submission:	22 October 2021
Thesis defense:	16 December 2021

Abstract

Over the last twenty years, the study of mechanical oscillators for sensing and quantum applications has gained great interest. The versatility of possible couplings of mechanics to other system such as optical, microwave, solid-state spin systems, all of which can already be operated in the quantum regime, makes them important candidates for hybrid interconnects in quantum devices and networks.

In this work we consider one such interface between a mechanical oscillator and a microwave circuit. The fragility of quantum states to their environment necessitates the development high-quality materials and devices to preserve the quantum nature of the studied interactions. Our group has pioneered ultra-coherent mechanical oscillators which we here integrate into a low-loss superconducting resonator such that mehanical motion can be manipulated and read-out by microwave light.

We describe the cleanroom fabrication flow of a NbTiN superconducting resonator, an Al-metallised patterned SiN membrane and their assembly into a flip-chip electro-mechanical device. Then we characterise microwave, mechanical and interaction parameters at millikelvin temperatures: with mechanical quality factor of $1.5 \cdot 10^9$ at $2\pi \cdot 1.5\,\mathrm{MHz}$, deep sideband resolution with total cavity decay rate of $2\pi \cdot 230\,\mathrm{kHz}$ and modest single-photon coupling of $2\pi \cdot 0.87\,\mathrm{Hz}$. The main result of this work is the cavity-assisted cooling of the mechanics into its quantum ground state of motion, that is with an average occupancy less than a single quantum.

Ultra-coherent mechanical oscillators integrated into quantum devices can serve as long-lived memories for quantum states manipulated in superconducting qubits. A simultaneous interfacing of mechanical elements with microwave and optical resonators can establish electro-opto-mechanical transduction between superconducting quantum computers and long-distance optical communication networks.

Sammenfatning

I løbet af de sidste tyve år har studier af mekaniske oscillatorer, med henblik på sensor- og kvantefysiske anvendelser, tiltrukket stor opmærksomhed. Mangfoldigheden af mulige systemer som mekaniske systemer kan koble til, såsom optiske, mikrobølge, faststof spin systemer, der alle allerede kan opereres i kvanteregimet, gør dem til vigtige kandidater for hybridbindeled i kvanteapparater og netværk.

I dette værk betragter vi et sådant bindeled mellem en mekanisk oscillator og et mikrobølgekredsløb. Skrøbeligheden af kvantetilstande overfor deres miljø nødvendiggør udviklingen af højkvalitetsmaterialer og -apparater for at bevare kvanteegenskaberne af de undersøgte interaktioner. Vores gruppe har pioneret ultrakohærente mekaniske oscillatorer som vi her integrerer i en lavtabs superledende resonator sådan at mekanisk forskydelse kan manipuleres og læses ud med mikrobølgelys.

Vi beskriver rentrumsfabrikationen af en NbTiN superledende resonator, en Al-metalliseret mønstret SiN membran og deres samling til et flip-chip elektromekanisk apparat. Så karakteriserer vi mikrobølge-, mekanik- og vekselvirkningsparametre ved millikelvin temperaturer: med mekanisk kvalitetsfaktor på $1.5 \cdot 10^9$ ved $2\pi \cdot 1.5\,\text{MHz}$, dyb sidebåndsopløsning med total kavitetshenfaldsrate på $2\pi \cdot 230\,\text{kHz}$ og beskeden enkelt-foton kobling på $2\pi \cdot 0.87\,\text{Hz}$. Hovedresultatet af dette værk er den kavitetsassisterede køling af mekanikken ind i dens kvantemekaniske grundtilstand af bevægelse, hvilket vil sige med en gennemsnitlig befolkning under et enkelt kvant.

Ultrakohærente mekaniske oscillatorer integreret i kvanteapparater kan bruges som langlivede hukommelser for kvantetilstande der manipuleres i superledende qubits. En simultan sammenkobling af mekaniske elementer med mikrobølge og optiske resonatorer kan etablere elektro-opto-mekanisk transduktion mellem superledende kvantecomputere og langdistance optiske kommunikationsnetværker.

Acknowledgements

I would like to thank all the persons who have been around me during the time of this PhD project.

Academically closest, I would like to thank Albert Schließer for offering me the project and the possibility of working in his group. My formative years in the cleanroom are very much indebted to Anders Simonsen and Yeghishe Tsaturyan for the knowledge they shared. Thanks to Eric Langman and Thibault Capelle for their help in the cleanroom and lab, contributing when the project needed it the most and without whom this project was somewhat solitary.

Thanks to Red Elmahdi for the most wonderful friendship. And to Rodrigo Thomas, for going for a beer on my first day and much beyond.

Thanks to all the members of the quantum optics section who I have been around in the last six years. I hope I was able and will continue to show you my gratitude every day. Thanks to the staff at the DTU cleanroom, for all their help.

Thanks to my family and my friends.

With your permission, I present to you my PhD thesis.

Publications

Posters

During the course of this PhD project, we presented our original research in the format of posters at two major conferences:

- International Conference on Quantum Technologies ICQT2017 in Moscow, Russia (2017),
- Heraeus Seminar 749. "Photonic Links for Quantum Technology Platforms", Online (2021).

Journal Paper

A written publication was uploaded to the arXiv repository with the reference https://arxiv.org/abs/2107.05552v4 and published at the journal Nature Communications:

Y. Seis *et al.* "Ground State Cooling of an Ultracoherent Electromechanical System", Nat Commun **13**, 1507 (2022).
https://doi.org/10.1038/s41467-022-29115-9

Abbreviations

AWG - Arbitrary waveform generator

BHF - Buffered hydro-fluoric acid

DBA - Dynamical back-action

CPWR - Coplanar waveguide resonator

DR - Dilution refrigerator

DRIE - Deep-reactive ion etching

EMIR - Electro-mechanically induced reflection

FEM - Finite element method (simulation solver)

FSR - Free spectral range

HEMT amplifier - High electron mobility transistor amplifier

IDC - Inter-digitated capacitor

KI - Kinetic inductance

LGR - Loop-gap resonator

LO - Local oscillator

LPCVD - Low-pressure chemical vapor deposition

MW - Microwave

MXC - Mixing chamber of the DR

OFHC copper - Oxygen-free high-conductivity copper

PECVD - Plasma-enhanced chemical vapor deposition

PT - Pulse tube of the DR

RF - Radio frequency

SA - Spectrum analyser

SEM - Scanning electron microscope

SG - Signal generator

TLS - Two-level systems

UV - Ultra-violet

VNA - Vector network analyser

Contents

Abstract **i**

Sammenfatning **iii**

Acknowledgements **v**

Publications **vii**
Posters vii
Journal Paper vii

Abbreviations **ix**

Contents **xi**

List of Figures **xiv**

1 Introduction and Motivation **1**
1.1 Overview of the Field 1
1.2 Goals of the Research 3
1.3 Structure of the Thesis 4

2 Circuit and Electromechanics Theory **7**
2.1 Readout of a Resonant Circuit 7
2.2 Mechanically Compliant Capacitor 10
Simulation of the microwave resonance 12
2.3 The Electro-Mechanical Coupling 14
Participation ratio in the literature 15
Strategies to increase the participation ratio 16
2.4 The Mechanical Oscillator 17
The phononically-shielded SiN membranes 18
Mechanical figures of merit 21
2.5 Theoretical Opto-Mechanical Treatment 22

Mechanical manipulation via light 24
Electro-mechanically induced reflection 25

3 Device Fabrication **27**
3.1 Chronology of Device Fabrication 27
3.2 Initial Devices and Fabrication Processes 29
Moderate success at depositing NbTiN in Lesker 29
Microwave resonators with IDCs 30
Electro-mechanical device with IDC dielectric coupling . . . 32
3.3 Fabrication of the Loop-Gap Resonator 33
Fabrication flow 35
3.4 Phononic Membrane Device Fabrication and its Metallisation 37
Fabrication flow for the membrane and its metallisation . . . 38
Fabrication flow for the shadow mask 41
Metallisation with NbTiN 43
3.5 Flip-Chip Bonding 44
3.6 Fabrication Failures and Modifications in the Process Flow . 48
Deposition of superconducting MgB_2 48
Deposition of superconducting Nb 49
Etching NbTiN from Cl_2 to SF_6 49

4 Device Characterisations **51**
4.1 Microwave Hardware and Cryogenic Setup 51
Microwave Equipment 51
Flow Cryostat 52
Dilution Refrigerator 54
4.2 Microwave Reflection Measurements 57
LGR characterisation at 4K and millikelvin 58
4.3 Mechanical Characterisation 60
Mechanical Ringdown Measurements 61
Mechanical quality at millikelvin temperatures 62
Mechanical Spectrum and Frequency Stability at millikelvin temperatures 64
4.4 Electro-Mechanical Interaction Calibration 65
Calibration of the Single-Photon Coupling Using the Gorodetsky Method 66
Calibration of the multi-photon coupling, wiring loss and amplification 68
4.5 Supplementary Devices 69
Dielectrical Coupling 69
Double Defect Membrane 69

Thinnest Membrane of 20 nm 71

5 Ground State Cooling 73

6 Outlook 79
6.1 Superconducting Microwave Filter Design 79
Tuning mechanism: Superconducting Kinetic Inductance . . 80
Filter design 80
Design Parameters 82
Noise Estimations 83
6.2 Towards Electro-Opto-Mechanics 84

A Circuit Analysis 87
A.1 Impedance transformation of the mutually coupled inductors 87

B Hamiltonian and equations of motion 89
B.1 Hamiltonian in the rotating frame 89
B.2 Equations of motion 91
B.3 Dynamical Backaction 93
B.4 Electro-Mechanically Induced Reflection 94
Special Cases 96
Mechanical Characterisation 97

C Samples Summary 99
C.1 Flipchip v2 - Dielectric Coupling 99
C.2 Flipchip v6 - Double Defect Membrane 99
C.3 Flipchip v20 - Single Defect Membrane 100
C.4 Flipchip v24 - Single Defect 20 nm Membrane 100
C.5 Flipchip v26 - Highest Participation Ratio Flip-chip 100
C.6 Flipchip v27 - Ground State Cooling 101

D Published Paper 103

Bibliography 119

List of Figures

2.1 Diagram of transmission line and resonator 8
2.2 Sketch of RLC model 10
(a) LRC resonator coupled to an electrical port via a mutual inductance. 10
(b) Equivalent circuit where the mutual inductance is replaced by a T-piece of inductances. 10
2.3 Sketch of Mechanical Capacitor 11
2.4 Sketch of full Circuit Model 12
2.5 FEM simulation for microwave resonance 13
(a) Finite element model geometry for MW resonator. . . . 13
(b) Geometry of the loop-gap resonator. 13
(c) Simulated E-field norm of the MW resonance. 13
(d) Simulated MW mode frequencies. 13
2.6 Sketch of Mechanical Oscillator 18
2.7 Metallised Mechanical Oscillator 19
(a) Optical image of a metallised membrane. 19
(b) Simulated normalised mode shape of the fundamental defect mode. 19
(c) Simulated normalised mode curvature of the fundamental defect mode. 19
(d) Simulated frequency spectrum showing a bandgap. . . . 19
2.8 Metallised Double Defect Membrane 20
(a) Metallised double defect membrane. 20
(b) Simulated mode shapes of coupled modes. 20
2.9 Illustration of DBA 25
2.10 Illustration of EMIR 26
(a) EMIR feature against frequency. 26
(b) EMIR feature in the complex plane. 26

3.1 Images of superconducting H-antenna 31
(a) Picture of H-antenna chip in 3D box 31
(b) Image of the H-antenna on chip 31

(c) Close-up of NbTiN IDC . . . 31
(d) Image of a patterned membrane over IDC . . . 31
(e) Sketch of the dielectric coupling scheme . . . 31
3.2 Resonance frequency tuning with IDC size . . . 32
(a) MW spectrum of RT resonances . . . 32
(b) Fit resonance to circuit model . . . 32
3.3 Images of superconducting resonator with recess . . . 34
(a) Optical image LGR chip . . . 34
(b) SEM zoom of LGR . . . 34
(c) SEM close-up LGR gap . . . 34
(d) SEM close-up of resonator recess . . . 34
(e) Spacing pillars after recess etching . . . 34
(f) NbTi incoupling loop . . . 34
3.4 Fabrication flow LGR . . . 35
3.5 Images of the membrane metallisation . . . 39
(a) Optical image membrane . . . 39
(b) Optical zoom-in of alignment holes . . . 39
(c) Optical image shadow mask . . . 39
(d) Zoom-in of alignment pillar on mask . . . 39
(e) Close-up of shadow mask opening . . . 39
(f) Metallised membrane . . . 39
3.6 Images of the membrane metallisation . . . 40
(a) Mounting in e-beam deposition tool . . . 40
(b) Carrier for annealing of Al metallisations . . . 40
3.7 Fabrication flow membrane . . . 40
3.8 Fabrication flow shadow mask . . . 42
3.9 Images of NbTiN metallisation . . . 44
(a) Compressive stress of NbTiN metallisation . . . 44
(b) NbTiN metalisation without substrate rotation . . . 44
3.10 Photographs of the flip-chip bonder . . . 45
(a) Overview of the bonder tool . . . 45
(b) Close-up of the vertical vacuum holder . . . 45
3.11 Images of epoxy bonding . . . 46
(a) Applying the epoxy . . . 46
(b) Epoxy pulled-in to the membrane . . . 46
3.12 Interference patter between membrane and resonator . . . 47
(a) Interference colour gradient is a distance gradient . . . 47
(b) Colour of a collapsed membrane . . . 47
(c) Colour of a resist residue . . . 47

4.1 Microwave setup . . . 52

(a) MW setup for direct detection 52
(b) MW setup for homodyne detection 52
4.2 Janis cryostat for characterisation 53
(a) Picture of Janis flow cryostat 53
(b) Janis MW line sketch 53
4.3 DR setup 55
(a) DR MW line sketch 55
(b) Mechanical isolation stage 55
4.4 Cavity frequency vibrational noise 56
4.5 Fit to reflection coefficient 59
(a) Cavity fit for flipchipv27 in Janis 59
(b) Cavity fit for flipchipv27 in DR 59
4.6 Mechanical bandgap 61
4.7 Measurement of ringdown sequence 62
4.8 Ringdown power series 63
(a) Ringdown series in time 63
(b) Fit of the power series 63
4.9 Ringdown temperature series on flipchipv27 at millikelvin 64
(a) First bandgap mode 1.485 MHz 64
(b) Second bandgap mode 2.671 MHz 64
4.10 Mechanical frequency spectrum at 30 mK 65
(a) Frequency spectrum with 1 mHz resolution 65
(b) Ringdown corresponding to frequency spectrum 65
4.11 Calibration of phase modulation 66
4.12 Gorodetsky calibration of g_0 67
4.13 DBA calibration of the multi-photon coupling g 68
4.14 Double defect characterisation 70
(a) Double defect interferometer spectrum 70
(b) Double defect mode ringdown in DR 70

5.1 Thermal calibration series 74
(a) Mechanical mode thermalisation at millikelvin. 74
(b) Cavity parameters at millikelvin. 74
5.2 Ground state cooling series 75
5.3 Cavity power series 76

6.1 Operation of the superconducting microwave filter 81
6.2 Microwave filter tuning by kinetic inductance 82
6.3 Electro-opto-mechanical assembly 85
(a) Electro-opto-mechanical assembly sketch 85
(b) Picture of the initial machined EOM cavity. 85

A.1 Impedance transformation of inductances 87
(a) Two inductances coupled by their mutual inductance. . . 87
(b) Equivalent impedance in a T-piece topology. 87

Chapter 1

Introduction and Motivation

The here-presented PhD thesis explores the possibility of precision measurements of mechanical motion with light in the microwave range of the electro-magnetic spectrum ($\sim$4 GHz to $\sim$9 GHz). This research resides at the intersection of several academic and industrial fields all with their own long traditions, from which we can pull knowledge and know-how. Let us first explore the broader context of our work.

1.1 Overview of the Field

The idea of light exerting a pressure on objects has been theorised as far back as the 17th century by Kepler by the shape of comet tails pointing away from the Sun and has been measured over a century ago in lab experiments. Science fiction literature and movies have also made use of the concept of solar sail for interstellar propulsion, and real-world spacecrafts are designed with this technology.

The first considerations of the radiation-pressure force in the context of opto-mechanics are attributed to Braginsky in the analysis of the light-induced modification of the mechanical frequency and damping rate[BM67; BMT70] and the establishment of the Standard Quantum Limit of measurement precision on a mechanical oscillators position[Mas+19], which is a fundamental limitation relevant for gravitational wave detection[Cav80; Abb+16].

In the last twenty years, research in superconducting circuits operated at cryogenic temperatures has enabled the coherent control of quanta of light at microwave frequencies (in the Gigahertz range)[Kja+20]. Starting with the first realisations of superconducting qubits[NPT99] based on the Josephson effect[Jos62], quantum superpositions of electrical current

or charge states are now routinely manipulated on chip with the goal of processing information in the new paradigm of quantum computing[NC10]. To make full use of the computational advantage of manipulating quantum information over classical computing, processors must reach a sufficiently large size and preserve the information integrity during the entirety of computation.

Progress towards longer qubit coherence has been made both by a better understanding of material limitations [MM14] and design geometry, with the transmon qubit[Koc+07] being the currently most widely used design, also in commercial quantum computers. The manipulating of electron spins in Silicon via microwave cavities[Mi+17] opens up the possibility of leveraging the industrial infrastructure of CMOS technology for the fabrication of chips for quantum information processing[Ans+20]. While for the long-range connections of quantum nodes, the storage of microwave quanta in long-lived memories[Rea+16; Cha+21] could enable the distribution of entanglement as a resource for the quantum internet[Kim08].

In the same two decades, major steps have been made to control mechanical motion with light. The first experimental realisation of the cooling of a mechanical object by laser light[CHP99] using a feedback approach (where the mechanical displacement is measured and the light pressure is actively modulated to counter it) was then followed by cavity-assisted cooling schemes [Sch+06] (where the light stored in the cavity can act as a passive viscous force) enabling cooling of a mechanical mode to its quantum ground state[Teu+11].

However the electro- and opto-mechanical systems referred to so far tend to co-localise mechanical and light modes, which can lead to large coupling rates[Cha+11] but makes any separate improvement of mechanical or light modes (for example improving their quality factor) more difficult. The separation of mechanics and optics [Tho+08] led to the rising popularity of high-stress Silicon Nitride membranes due to their high intrinsic mechanical quality[NMG16; YPR12] and broad design flexibility to define the protection of mechanical modes[Tsa+17; Gha+18]. At the same time, new cavity designs can be explored[FJ+12; Jan+17; Roc+21], or the mechanical mode can even be optically [BMS16] or electrostatically [HBY19] defined.

A popular vision for a distributed quantum network uses microwave superconducting error-protected quantum processors[Kel+15] (with a large number of qubits) as its nodes that are connected via optical links, for long-distance propagation. This architecture requires components that are already difficult to achieve on their own: such as high-fidelity information manipulation at the nodes[Tuc+20], a microwave-to-optics transduction on the level of single photons with high efficiency and low added noise[Zeu+20],

and optical propagation amplified by quantum repeaters based on distributed entanglement[Liu+21; LR+21].

Research on quantum microwave-to-optics transducers has expanded rapidly in the last five years: initially attempted on membrane-based electro-opto-mechanical systems[Bag+14; And+14], experiments expanded to include piezoelectric coupling[Han+20; Mir+20; Sha+19], direct electro-optic coupling[Hea+20; Hol+20], or that via Rydberg atoms[Vog+19]. However demonstration of transduction with efficiency above 50% and added noise of much less than a single quantum, required for maintaining the quantum nature of the converted information, remains a challenge.

1.2 Goals of the Research

This PhD research project was oriented towards the integration of ultra-high quality factor Silicon Nitride membranes into superconducting resonators, and to operate this electromechanical system at cryogenic temperatures. Later a combination with the already well established opto-mechanics experiments is envisioned to realise a mechanically-mediated microwave-to-optical link.

The first step in the work involved learning how to simulate a microwave resonator in a finite element method (FEM) solver: we simulated the designs in the commercial software COMSOL to understand the geometry dependence on the microwave resonance frequency and how the displacement of the mechanical element modifies this resonance. These simulations gave us insights into the fabrication requirements ahead in order to reach high coupling between the microwave and mechanical resonators.

In parallel, we needed to develop a fabrication process that would allow us to work with superconducting materials with high critical temperature so as to be as flexible as possible in the cryogenic requirements. Since there was no prior knowledge of fabricating with superconducting materials in the group or at the cleanroom of the Danish Technical University, we needed to explore different materials for their ease of fabrication and superconducting properties. The availability of vacuum cryogenic equipment in the lab in particular informed the choice of superconductor: before the arrival of our dilution refrigerator, the choice was restricted to materials with critical temperature significantly above approx. 4 K of our Helium flow cryostat; with the dilution refrigerator, more conventional superconductors were also within reach.

The fabrication flow needed to take into account both the complexity of all the materials involved and their compatibility issues, as well as the

extreme cleanliness of the processing that would allow to maintain the very high quality of the microwave and mechanical resonances, once the final device was assembled. The cleanliness of processed surfaces also impacted the coupling, since any processing residue would compromise the sub-micron proximity needed between the two resonators.

Operating the device at millikelvin temperatures finally asked for an improved understanding of material properties close to absolute zero. The most important factor was ensuring high thermal conductivity from the cooling head to the sample, implying the use of high-purity copper where possible. Device manipulation and read-out asked for extensive computer-based scripting and interfacing with high-end microwave equipment, to conduct our measurement protocols. As for the data analysis, a solid knowledge of opto-mechanics theory enabled quantitative statements to be extracted, that supported our claims.

The work presented in this thesis is a building block for future research in the opto-mechanics group around applications of ultra-high quality electro-mechanical devices at cryogenic temperatures. The system we demonstrate has potential as a component in a larger quantum information processing chip or network, where its very low mechanical energy dissipation makes it a candidate for a quantum-state-preserving memory in the microwave range. A more complete characterisation of its memory capability will establish its usefulness and required improvements for interfacing with already existing quantum hardware.

Finally the full integration of an electro-opto-mechanical device for quantum transduction is the next big step in the lab's development. Now that the microwave and optical interfaces to the long-lived membranes have been established, we look towards bringing these technologies together, that were traditionally separate in the quantum realm. The broader connectivity of disparate quantum systems into hybrid devices and networks opens up the development of new technologies, new scientific instruments and a deeper understanding of the foundations and applications of quantum physics.

1.3 Structure of the Thesis

This thesis is structured as follows. In Chapter 2, we review the theoretical underpinnings of the work presented in this thesis: a derivation of the input-output formalism adapted to our microwave cavity system and the perturbation to the cavity dynamics due to a mechanically movable capacitor. We support theoretical calculations with computer simulations. We review the core features of the ultra-coherent mechanical resonators

in use in our research group, and lay down some of the standard results in the field of opto-mechanics used in the characterisation of our electro-mechanical system. More complete derivations of standard results are laid out in Appendix A for the electrical circuit analysis and in Appendix B for the system Hamiltonian.

In Chapter 3, we present the efforts that went into the fabrication of the superconducting electro-mechanical devices. We explicate the fabrication flows, supplemented with pictures, for the superconducting resonator chip, the phononically-shielded membrane chip and its metallisation, and the assembly of these two chips into a flip-chip device. We also include some initial fabrication attempts and microwave circuit designs that were later abandoned, as well as fabrication failures.

In Chapter 4, we first describe the microwave instrumentation used for device characterisation, and the vacuum cryostat and dilution refrigerator in which the devices are cooled to near absolute zero temperature. We present the measurement of microwave cavity and mechanical parameters as well as quality factors, and the calibration of the electro-mechanical interaction for our main device 'flipchipv27' (the device for which we demonstrate mechanical ground state cooling). In Appendix C, we summarise other important devices characterised throughout this research project.

In Chapter 5, we show the main result of our research project: the cavity-assisted sideband cooling of an ultra-high quality mechanical mode of our main electro-mechanical device into its quantum ground state. We include the full arXiv pre-print version of our publication in App. D.

In the outlook Chapter 6, we propose a design of a tunable superconducting narrow-band on-chip filter to reduce the sideband noise of our microwave signal generator. We finally look out onto the future integration of the opto-mechanics and electro-mechanics efforts in our lab.

Chapter 2

Circuit and Electromechanics Theory

In this chapter, we derive theoretical expressions for the system composed of a mechanical element coupled to a microwave cavity, the mechanical element being part of a capacitor in the circuit. We first look at a generic resonant electrical circuit coupled to a transmission line and write expressions for the resonance frequency and losses in terms of the electrical components. Then we decompose the total capacitance into a constant and mechanically-compliant parts, and extract how the motion of the mechanical element modulates the parameters of the microwave circuit.

We present the main equations needed for the research topic of the thesis, such as dynamical backaction and mechanically induced reflection. Most of them are stardard results in the field, found for example in the Opto-Mechanics Review[AKM14] and for which some full derivations are given in App. A and B.

2.1 Readout of a Resonant Circuit

We start with a *resonator* terminating a *transmission line*. As depicted in Fig. 2.1, electromagnetic energy circulates in the resonator. Due to the coupling to the transmission line, some of the energy leaks out into the transmission line, and energy can also be injected into the resonator. Moreover, some energy is lost to the environment, due to electrical loss in the resonator. Simplistically, we may say that the resonator has a *resonance frequency* at which electromagnetic energy will coherently build up inside the resonator and be stored. This corresponds to the rate at which the energy in the resonator cycles between electrical and magnetic forms.

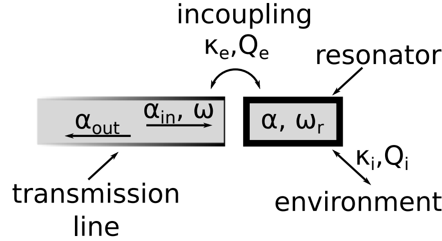

Figure 2.1: Diagram of transmission line (left) and resonator (right), where we depict the leaking in and out of the cavity characterised by the external quality factor, as well as the loss to the environment characterised by the internal quality factor.

Coupling to the environment and to the transmission line leaks energy out of the resonator at rates which we call the *internal loss rate* and the *external coupling rate* respectively; the sum of these two is the *total loss rate*. By comparing these rates to the resonance frequency, we can define the quality factors of these channels. We can develop the following intuition: the *internal quality factor* is the number of cycles the resonator can undergo before the energy is significantly lost to the environment (if that were the only loss channel); similarly the *external quality factor* is the number of cycles before the energy significantly leaks out into the transmission line (if there were no loss to the environment); the *loaded quality factor* is then the number of cycles before the energy is lost through the sum of all the coupling channels.

So far we have given an intentionally simplistic explanation. The above coupling to a resonator can be quantitatively characterised by input-output relations for classical fields. A signal α_{in} with angular frequency $\omega = 2\pi f$ and amplitude α_0 travels down the transmission line, reaches the resonator and partially enters the resonator. It is partially reflected, giving the outgoing field α_{out}. The field in the resonator α can be related to α_{in} and α_{out} by the expression:

$$\alpha_{\text{out}} = \alpha_{\text{in}} - \sqrt{\kappa_e}\alpha, \tag{2.1}$$

where κ_e is the external coupling rate. Energy enters the resonator from, and exits into, the transmission line port at a rate κ_e. In the frame rotating at the frequency of the incoming field, the field inside the cavity follows the

equation of motion:

$$\frac{d\alpha}{dt} = -\frac{\kappa}{2}\alpha + i\Delta\alpha + \sqrt{\kappa_e}\alpha_{\text{in}}, \tag{2.2}$$

where κ is the total resonator energy decay rate and $\Delta = \omega - \omega_r$ is the detuning of the input field ω from the resonance frequency ω_r.

The steady-state field in the resonator is found by solving Eq. 2.2 for $d\alpha/dt = 0$:

$$\alpha = \frac{\sqrt{\kappa_e}\alpha_{\text{in}}}{\kappa/2 - i\Delta}. \tag{2.3}$$

Then the output field, making use of Eqs. 2.1 and 2.3, is:

$$\alpha_{\text{out}} = \alpha_{\text{in}} - \frac{\kappa_e}{\kappa/2 - i\Delta}\alpha_{\text{in}}. \tag{2.4}$$

Finally, we write the complex *reflection coefficient* of the field returned from the resonator

$$S_{11,\text{ideal}}(\omega) = \frac{\alpha_{\text{out}}}{\alpha_{\text{in}}}(\omega) = 1 - \frac{2}{1 + \kappa_i/\kappa_e - 2i(\omega - \omega_r)/\kappa_e}, \tag{2.5}$$

where we used $\kappa = \kappa_e + \kappa_i$ with κ_i the internal loss rate. Real-world transmission lines add a phase shift s and delay τ as well as attenuation a (a can be larger than unity if there is an amplifier). Reflections along the cables can cause interferences between standing waves in the transmission line and the cavity mode characterised by an angle ϕ. A realistic reflection coefficient is then:

$$S_{11}(\omega) = ae^{is}e^{-i\tau(\omega-\omega_r)}\left[1 - \frac{2e^{i\phi}}{1 + \kappa_i/\kappa_e - 2i(\omega - \omega_r)/\kappa_e}\right]. \tag{2.6}$$

As the reflection coefficient is a quantity that can easily be measured using a vector network analyser (VNA), this expression for S_{11} can be used to fit experimental data to extract a resonator frequency and decay rates as well as to calibrate any loss, gain or phase delay in a measurement setup, due to for example cable loss, amplifier gain etc., as shown in Refs. [Pro+15; Gee+12].

We may relate this to the reflection of a signal travelling in a the transmission line with impedance Z_0 and arriving at a resonator with frequency-dependent impedance $Z_R(\omega)$[Cle+10]:

$$S_{11}(\omega) = \frac{Z_R - Z_0}{Z_R + Z_0} = 1 - \frac{2}{1 + Z_R/Z_0}. \tag{2.7}$$

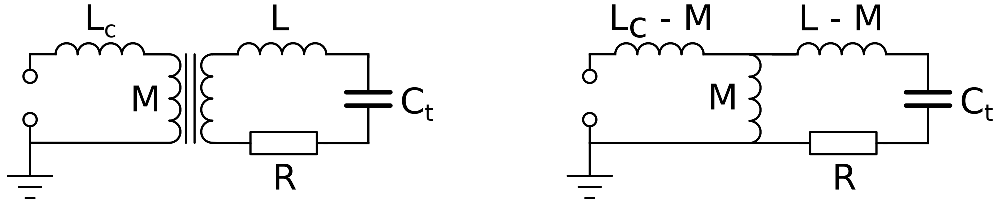

(a) LRC resonator coupled to an electrical port via a mutual inductance.

(b) Equivalent circuit where the mutual inductance is replaced by a T-piece of inductances.

Figure 2.2: Model of the microwave resonant circuit read out by a port, to which we connect e.g. a vector network analyser.

The superconducting microwave (MW) resonator used in this thesis is modelled as a circuit with series components the inductance L, capacitance C_{t} and resistance R. The circuit is coupled to a coaxial cable by its mutual inductance M to the coil with inductance L_c which terminates the cable. A sketch is presented in Fig.2.2(a). For analysis we can transform the two mutually coupled inductances into a three inductance T-shape, as depicted in Fig. 2.2(b) (see App. A.1 for derivation). Equating Eqs. 2.6 and 2.7 would then allow us to express the cavity parameters ω_r, κ_i and κ_e in terms of the circuit elements.

2.2 Mechanically Compliant Capacitor

Next, we complete the model of the MW resonator with a mechanical element as follows. The electrically-conducting mechanical element is part of a parallel plate capacitor, of which the motion modulates the capacitance. A sketch of the geometry of the mechanical capacitor is given in Fig. 2.3. We have:

- A: the overlap area of one half of the capacitor,
- d: the distance of the upper (mechanically moving) plate to the lower electrodes.

From the parallel plate geometry in Fig. 2.3, we effectively have two capacitors in series. We can thus write the capacitance of the mechanical

Figure 2.3: Sketch of a parallel plate capacitor, where one plate is mechanically moving. We present a side (left) and top view (right), visualising the relevant geometric parameters, where the extremities fading away lead to the remainder of the circuit.

element:

$$C_m(x) = \frac{\epsilon_0}{2} \frac{A}{d + x}, \tag{2.8}$$

where ϵ_0 is the vacuum permittivity and x is the amplitude of mechanical motion. This capacitance is typically on the order of 10 fF and changes due to the motion are in the attofarad region. Since even the best capacitance meters have difficulty measuring the femtofarad region, we cannot measure mechanical modulation of the capacitance directly, but instead include it in a resonant circuit by adding an inductance L in series. The resonator has an additional capacitance which is not due to the mechanical element, such as the self-capacitance of the conductor making up the inductor or the electrically conducting surfaces nearby: this we call the parasitic capacitance C_p, placed in parallel to C_m, and the total capacitance is $C_\mathrm{t} = C_\mathrm{p} + C_\mathrm{m}(x)$. Finally all conducting elements (also superconductors at microwave frequencies) will exhibit a certain amount of electrical loss which we model as a series resistor R. Again we measure the MW resonator by coupling it to the outside world via a coil antenna which has a mutual inductance with the inductor of the resonator. In summary we have the circuit in Fig. 2.4.

The electro-magnetic field inside the resonator containing information about the mechanical element can now leak out into the coaxial cable, connected to the coil antenna, and be measured by a vector network analyser or a spectrum analyser. We can say that the resonator has two loss channels: the 'good' channel into the cable which we can measure, and the 'bad' channel into the environment which we do not have access to. How much of the intra-cavity field we are able to extract from the resonator is quantified by the coupling efficiency $\eta_c = \kappa_e/(\kappa_e + \kappa_i)$.

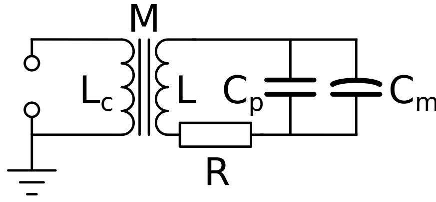

Figure 2.4: Sketch of the full circuit model where we explicitly separated the capacitance that is mechanically compliant.

Simulation of the microwave resonance

We can gain some insight about the MW mode of interest by simulating the geometry in the commercial finite element solver COMSOL. We show the model geometry in Fig. 2.5 of a conductive loop on a Silicon substrate. The loop is interrupted by a a gap with large electrodes, over the gap we hover a conductive pad forming a parallel plate capacitor. The distance d of the pad to the electrode plane influences the MW resonance frequency leading to the coupling of electrical and mechanical modes: for a distance ranging from 2000 nm down to 300 nm, the resonance frequency ranges from 9.4 GHz to 7.8 GHz. When removing the conductive membrane pad, the loop resonance increases to 9.8 GHz showing that the loop itself has a parasitic capacitance C_p. We fit the simulated data with the model in Fig. 2.4[1] and extract a value of $C_\mathrm{p} = 75\,\mathrm{fF}$ for the geometry fabricated in Sec. 3.3. As a consistency check of the simulation, we remove the conductive element representing the membrane metallisation and find a resonance frequency (red horizontal line in Fig. 2.5d) in very good agreement with the limit $d \to \infty$ of the fit (dashed blue curve).

We study the effect of substrate material in the vicinity of the conductor: in the fabricated samples the Si substrate is partially etched away near the conductor giving a lower C_p. In contrast, not removing the substrate increases the parasitic capacitance to $C_\mathrm{p} = 100\,\mathrm{fF}$.

[1] We fit $\omega_\mathrm{r} = 1/\sqrt{[C_\mathrm{m} + C_\mathrm{p}]L}$.

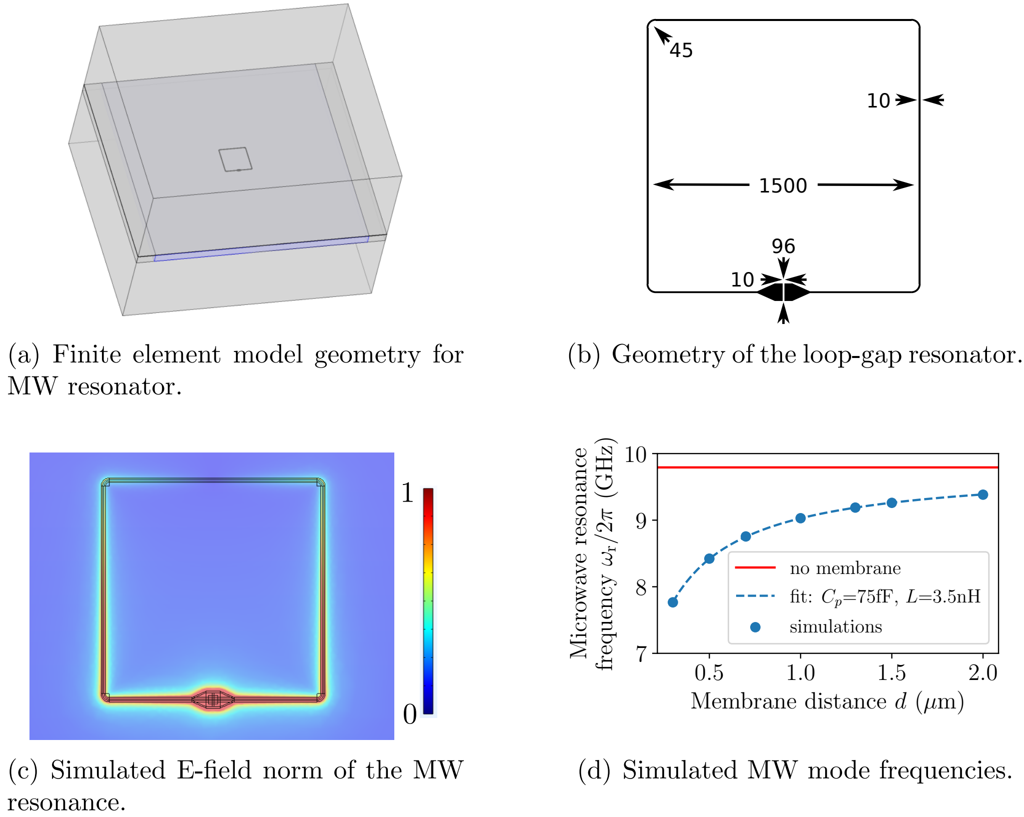

(a) Finite element model geometry for MW resonator.

(b) Geometry of the loop-gap resonator.

(c) Simulated E-field norm of the MW resonance.

(d) Simulated MW mode frequencies.

Figure 2.5: a) Geometry of the microwave chip simulated in COMSOL. Highlighted in blue is the Silicon chip held in the middle of a hollow volume (see Fig. 3.1(a) for the physical realisation). On the Si substrate, we place an electrically conducting loop-gap resonator (LGR) where the gap electrodes are bridged by a conductive pad hovering above it by a distance d ranging from 300 nm to 2000 nm. b) Dimensions in microns for the simulation and fabrication of the LGR (see Fig. 3.3 for the fabricated LGR chip). c) Simulated normalised electric field for the fundamental mode of the LGR. The highest field is located across the electrodes and mechanically compliant capacitance, to maximise the coupling between MW mode and mechanical displacement. d) Simulation of the MW resonance frequency as function of membrane gap, with a fit to the model in Fig. 2.4.

2.3 The Electro-Mechanical Coupling

The coupling between mechanics and MW cavity is determined by the mechanically induced frequency shift:

$$G = \frac{d\omega_r}{dx}. \tag{2.9}$$

With the expression for the resonance of a low-loss RLC resonator,

$$\omega_r = \frac{1}{\sqrt{LC_t}}, \tag{2.10}$$

and with Eq. 2.8, we can rewrite:

$$\begin{aligned} G &= \frac{d\omega_r}{dC_t} \cdot \frac{dC_t}{dC_m} \cdot \frac{dC_m}{dx} \\ &= \frac{-\omega_r}{2C_t} \cdot \frac{dC_t}{dC_m} \cdot \frac{-C_m}{d} = \eta_{C-C}\frac{\omega_r}{2d} \end{aligned} \tag{2.11}$$

Here we highlight the quantity $\eta_{C-C} = \frac{dC_t}{dC_m}\frac{C_m}{C_t}$, the participation ratio of capacitances. It quantifies how the parasitic capacitance modifies/reduces the electro-mechanical coupling. Ideally it is unity, but the presence of appreciable parasitic capacitance can reduce it down to the percent level. It can be understood as the electrical energy being split between the two capacitors and since only one is mechanically compliant, the mechanical motion has a reduced effect on the dynamics of the cavity. In the case of C_m and C_p being in parallel, η_{C-C} reduces to the ratio $\frac{C_m}{C_t}$, but for other circuits it may take a more complex form.

At this point, it can be instructive to point out that other analogous participation ratios can also be defined such that for the capacitance-to-resonance-frequency or mechanics-to-capacitance transductions. These are:

$$\eta_{RF-C} = \frac{d\omega_r}{dC_t}\frac{C_t}{\omega_r} = -\frac{1}{2} \tag{2.12}$$

$$\eta_{C-x} = \frac{dC_m}{dx}\frac{d}{C_m} = -1 \tag{2.13}$$

Since the expressions for η_{RF-C} and η_{C-x} are derived from Eq. 2.10 and Eq. 2.8, it does not look like any optimisation is possible here. We can however have a look at the literature to find other mechanics-to-circuit-component transductions to see if improvements are possible.

Other proposed and realised electro-mechanical implementations have mechanical transductions that are either fixed by the fabricated geometry or

tunable by electric/magnetic fields. The dielectric coupling of a nanobeam to MW electrodes[Fau+12; Per+14] or the dielectric coupling presented in Fig. 3.1 give rise to a transduction parameter G which is about four orders of magnitude lower than for a parallel-plate configuration. Tunable setups include a proposed parallel-plate capacitor coupled to a Josephson junction qubit[Hei+14] and a nanobeam coupled to a SQUID loop[RBS19], where the tuning of the mechanics-resonator coupling is achieved by a charge-biasing of the qubit and the flux-biasing of the SQUID loop.

Participation ratio in the literature

Here we briefly review electro-mechanical devices found in the literature based on Silicon Nitride (SiN) membranes partially metallised by a deposited metal thin film. We analyse three papers from the Steele (Delft, Netherlands)[Yua+15], Nakamura (Tokyo, Japan)[Nog+16] and Regal/Lehnert (Boulder, USA)[Hig+18; And15][2] groups, as well as a PhD thesis from the Deléglise group (Paris, France)[Cap20][3]. We compare the sizes of the mechanical capacitance, parasitic capacitances and resulting participation ratios of capacitances in order to assess a preferred MW circuit geometry.

We estimate the participation ratio and parasitic capacitance for these devices as follows. From the figures found in the publications, we can estimate the size and area A of the capacitor plates which together with quoted plate distance d is used to compute the mechanically modulated parallel-plate capacitance C_m in each case[4] Then we use the quoted MW resonance frequency ω_r, single-photon coupling g_0 and mechanical displacement zero-point fluctuations x_{zpf} to calculate $G = g_0/x_{zpf}$ and thus η_{C-C} using Eq. 2.11. From the participation ratio, we then extract the parasitic capacitance C_p assuming $\eta_{C-C} = C_m/(C_p + C_m)$. We report our findings in Table 2.1.

It is worth pointing out that two rather different MW circuits were used in these publications. In Nakamura's and Steele's works a device chip patterned with electrodes is used, which connect (capacitively for Steele and galvanically for Nakamura) to the wall of a superconducting 3D box, where the inductance is formed by the conductor on the chip and the walls of the box. On the other hand, in the work done by the Regal/Lehnert

[2]We only use the PhD thesis by Andrews for the geometry of the membrane metallisation, all other parameters are in the paper by Higginbotham et al.

[3]Certain parameters not available in the thesis were provided by the Thibault Capelle in private communication.

[4]Note again as in Sec. 2.2, we take A to be the overlap area of one half of the capacitor.

Group	$\omega_r/2\pi$ GHz	$g_0/2\pi$ Hz	x_{zpf} fm	$G/2\pi$ Hz/fm	d μm	η_{C-C} 1	A μm^2	C_m fF	C_p fF
Steele	5.066	0.22	0.6	0.35	3	0.45	850×350	45	55
Nakamura	5.343	7	3.3	2	0.3	0.25	$\pi/4 \cdot 45^2$	25	75
Regal/Lehnert	6.16	3.8	0.5	8	0.3	0.80	200×200	590	115
Deléglise	7.4	5.5	1.2	4.6	0.12	0.15	55×55	110	620

Table 2.1: Geometric parameters and experimental values from the literature and extracted parameters to estimate and compare the participation ratios.
Note that for work by the Steele, Regal/Lehnert and Deléglise groups, the overlap area A is rectangular, square and square respectively, whereas for the work by Nakamura's group it is circular with diameter 45 µm. For the Nakamura entry, x_{zpf} for the fundamental mode is calculated taking the dimensions of the SiN membrane to estimate $m_{eff} = 10\,\text{ng}$, together with its resonance frequency $\omega_m = 764\,\text{kHz}$; similarly for the Deléglise entry, we use $m_{eff} = 79\,\text{ng}$ and $\omega_m = 481\,\text{kHz}$

and Deléglise groups, the circuit is a 'loop-gap resonator' (LGR) where the inductor is all defined by a loop on the same chip. Indeed this leads to the most important difference between these devices: LGR designs tend to have higher parasitic capacitance, an issue which we have also struggled with since it significantly reduces the single-photon coupling. In the device of Regal/Lehnert, the mechanical capacitance is fabricated to be much larger in order to overcome the larger parasitic capacitance.

Strategies to increase the participation ratio

Since $\eta_{C-C} \sim \frac{C_m}{C_t} = \frac{C_m}{C_p+C_m}$, we aim to design MW circuits which minimise C_p. This is however not quite straightforward. A difficulty for us has been that any conducting wire or loop has its own capacitance (self-capacitance), approximately proportional to its length. The inductance of a loop scales with the enclosed area, we have the constraint that any increase in inductance (which we use to reduce the MW resonance frequency into the working range of our equipment) is accompagnied by an increase in parasitic capacitance.

The conceptually easier way out is to have a large mechanical capacitance (larger than C_p), such that we can use a smaller inductor loop. Two difficulties can arise here: firstly that this requires a small capacitor vacuum distance (membrane to electrodes) which is difficult to reliably fabricate,

secondly large membrane metallisations are needed for large capacitor areas. If the metallisation is too large, we may be depositing metal on the nodes of the membrane's displacement profile: indeed adding metal at a displacement node does not contribute to the electro-mechanical coupling while adding mass and mechanical loss. The strategy of having a large capacitor area combined with a small vacuum gap allowed the Regal/Lehnert device to reach such high coupling rates.

A second strategy would be to place the mechanical element as the in-coupling element to the MW cavity (as done in an earlier publication of the Steele group[Sin+14]). Then we would have more freedom in the design of the MW resonator. In particular we can design a resonator with large impedance ($Z_c = \sqrt{L/C}$), which recently gained interest in the literature[Per+20; Sam+16], separately from the mechanical element, and later add the mechanics 'perturbatively'. Then we may be able to design a resonator with a capacitance (that will become the parasitic capacitance) much smaller than the mechanical one.

2.4 The Mechanical Oscillator

In its most basic form, a harmonic mechanical oscillator in one dimension is a mass m_{eff} which moves along an axis, say the x-axis, and is restored towards its resting, equilibrium[5] position d by a force (the 'spring') proportional to the distance of the oscillator from $\vec{d}$ that is $\vec{F} = -k_{\text{eff}}(\vec{x} - \vec{d})$, where k_{eff} is the effective spring constant. The out-of-plane motion of 2D membranes can be decomposed into many mass-on-a-spring oscillators. For the membranes considered in this thesis, spectral isolation of the modes of interest allows us to consider them as decoupled from all other modes. The motion of each of these isolated modes can then be considered as a single mass-on-a-spring as suggested by the schematic depiction in Fig. 2.6.

The restoring force makes the mass oscillate back and forth around $\vec{d}$ at a constant angular frequency Ω_{m}. Within one such oscillation cycle, the energy of the oscillator is then transformed from potential to kinetic energy (when the oscillator velocity is in the same direction as the restoring force), and from kinetic to potential energy (when velocity and force are in opposite direction). The material of the oscillator can have internal friction and other loss mechanisms leading to dissipation of energy into the mechanical bath at a rate Γ_m. In the limit of small mechanical loss, we have $\Omega_m = \sqrt{k_{\text{eff}}/m_{\text{eff}}}$ and the high quality factor (Q-factor) is $Q_m = \Omega_m/\Gamma_m \gg 1$.

[5]The equilibrium $\vec{d}$ of the mechanics is the distance of the capacitor distance from Sec. 2.2

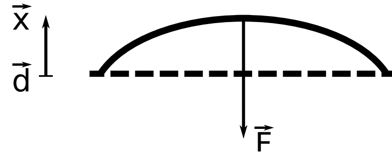

Figure 2.6: Sketch of a mechanical membrane oscillator displaced (to $\vec{x}$) from its resting position $\vec{d}$ and being pulled back towards its equilibrium by a mechanical restoring force $\vec{F}$.

Mechanical oscillators come in various forms with large ranges of effective masses and frequencies: Fig. 7 of Ref. [AKM14] gives a good overview. Generally, mechanical oscillators are 3-dimensional objects. However the oscillation mode that one typically considers only has a displacement in one direction, which we define as being the x-axis. From finite-element simulations, we can find the spatial distribution of the mechanical eigenmodes of our oscillator, and extract the resonance frequencies and effective masses of the different modes.

The phononically-shielded SiN membranes

Our mechanical system is a membrane made out of a highly stressed material, Silicon Nitride (SiN, with chemical composition Si_3N_4). A variety of experiments have used this material platform, with frequencies in the range 100 kHz to 10 MHz and masses 100 pg to 10 ng. We show a fabricated membrane with metallisation in the center and a simulated spatial profile of the mode where the displacement of the metallisation is highest in Fig. 2.7.

The perforation pattern of the membrane results from an in-depth study done in our group to minimise mechanical dissipation of energy to the environment. Important improvements have been done by developing a membrane with a phononic bandgap[Tsa+17] as well as strain engineering the pattern[Gha+18]. A simulated mode spectrum of the mechanical oscillator shown in Fig. 2.7(d) clearly shows a region empty of mechanical modes except for our mode of interest. The perforation pattern can be divided into two regions: the periodic lattice of unit cells in most of the membrane creates the phononic shield which exhibits a phononic bandgap: mechanical vibrations in the frequency range of the bandgap are damped exponentially with travelled distance. The central modification of the pattern constitutes the defect which hosts eigen-modes at frequencies inside the bandgap such that these vibrations may not leak out of the defect and disturbances from the outside cannot travel to the defect. The transition from defect to

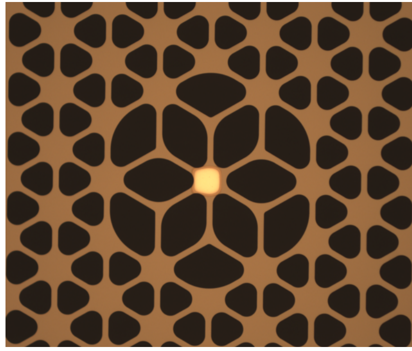

(a) Optical image of a metallised membrane.

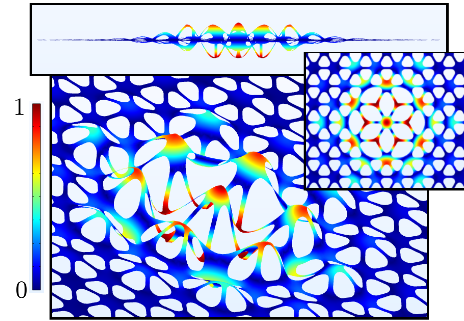

(b) Simulated normalised mode shape of the fundamental defect mode.

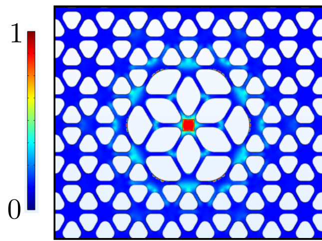

(c) Simulated normalised mode curvature of the fundamental defect mode.

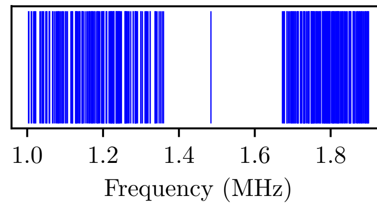

(d) Simulated frequency spectrum showing a bandgap.

Figure 2.7: a) Micrograph of a fabricated mechanical oscillator (brown) where the central defect has been metallised with a superconducting material (yellow) in order to integrated into a superconducting capacitor. b) Spatial profile of the out-of-plane motion of the fundamental defect mode for which the displacement of the central metallisation is largest. Pattern design and simulations are done with COMSOL using the Solid Mechanics module by Eric Langman. c) Spatial profile of the curvature of the same fundatmental mode. Regions of strong curvature lead to mechanical loss[YPR12]. d) Simulated mode spectrum revealing a phononic bandgap around the fundamental defect mode at 1.5 MHz.

phononic crystal occurs in the same material, such that the clamping to the frame happens in a region where the mechanical displacement has decayed.

Further research has lead to the development of phononically shielded membranes with multiple defects[CTS20; Kos+20]. One such metallised double-defect membrane is shown in Fig. 2.8(a). Each defect separately hosts a mode and placing defects next to each other couples their motion because of their overlapping spatial patterns. The coupling of the fundamental modes of two defects gives rise to two new eigen-modes: one where the defects move in unison and one in opposition to each other, as shown by the simulated modes in Fig. 2.8(b). Here the metallisation of the upper defect increases its mass leading to a reduced hybridisation of the double-defect mode, consequently the two modes have unequal amplitudes at the two defects.

Membranes with multiple defects open the possibility of integrating mechanical oscillators in to hybrid systems. Each defect can functionalised by a different type of coupling such as electro-mechanical, opto-mechanical[Bag+14; And+14; Hig+18], to a spin[Kos+20; Fis+19]. Multiply functionalised membranes have already been used in the classical transduction from RF to optical of nuclear magnetic resonance signals[Sim+19; Tak+18].

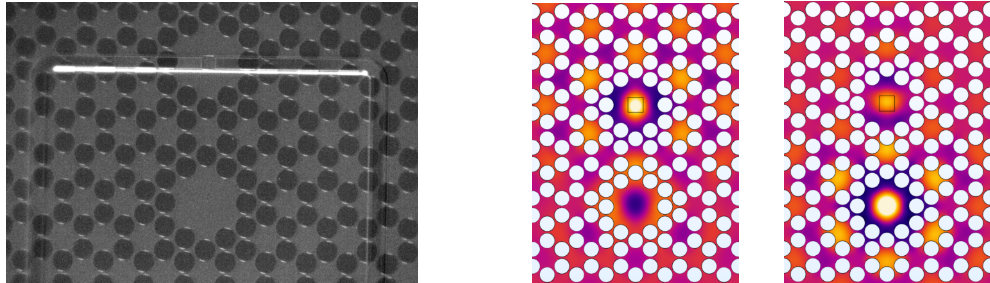

(a) Metallised double defect membrane.

(b) Simulated mode shapes of coupled modes.

Figure 2.8: a) Micrograph of a fabricated double defect membrane where the upper of the two defect has been metallised (the faintly visible square). An LGR is faintly visible underneath the membrane. b) Simulated displacement patterns of the coupled modes in blue: left mode dominated by the metallised defect (indicated by the square on the top defect) at ∼1.32 MHz, right mode dominated by the optics defect at ∼1.36 MHz. Light and dark colours indicate positive and negative out-of-plane displacement respectively.

A design difference is visible here between the "Dahlia"[6] defects (of the double-defect membrane in Fig. 2.8) and the "Lotus" defect (of the single defect membrane in Fig. 2.7). The "Dahlia" design was developed by Yeghishe Tsaturyan without metallisation initially in mind: as a consequence, the metal pad pulls the mode frequency down and closer to (and sometimes into) the phononic band, as seen in Fig. 4.14(a). On the other hand, Eric Langman's "Lotus" was designed and simulated specifically with metallisation in mind: its defect mode is designed in such a way as to place the mode's frequency at the center of the bandgap. See Sec. 4.3 for measured bandgaps and ringdowns on the single- and double-defect membranes.

Mechanical figures of merit

Since we are dealing with harmonic oscillators, we may rewrite the position operator of the mechanics $\hat{x}$ as $x_{zpf}(\hat{b}+\hat{b}^\dagger)$, where $\hat{b}$ is the phononic ladder operator. The mechanical *zero-point fluctuation* x_{zpf} is the mechanical root-mean-square displacement of the ground state, which is due to its finite, half-quanta energy $\hbar\Omega_m/2$. Therefore x_{zpf} satisfies:

$$2\cdot\frac{1}{2}m_{eff}\Omega_m^2x_{zpf}^2=\frac{\hbar\Omega_m}{2}, \tag{2.14}$$

where the factor of 2 on the left-hand side is due to the equi-partition of mechanical potential and kinetic energies. The expression for the zero-point fluctuation amplitude is therefore $x_{zpf}=\sqrt{\hbar/(2m_{eff}\Omega_m)}$.

For quantum applications, the size of the zero-point fluctuations is an important figure of merit. For maximal transduction of motion to capacitance modulation, we wish to place the metallisation in an area where the spatial mode is maximum. This can be seen as an extension to the optimisation of η_{C-x} in Eq. 2.13. In this way, we achieve larger capacitance fluctuations and in turn larger MW frequency fluctuations as a result of the mechanical zero-point motion.

Another important quantity is the quality factor of a mode which, similar to MW qualitity factors, relate the mechanical angular frequency Ω_m to the dissipation rate Γ_m by $Q_m=\Omega_m/\Gamma_m$ and sets the scale for the number of oscillations before mechanical energy is significantly lost. From a quantum perspective, Γ_m is the rate at which a single phonon enters or leaves the mechanical oscillator, thus if there are $\bar{n}_{\rm th}$ phonons in thermal environment

[6]The flower names for the different bandgap and defect designs were conceived by Eric Langman.

of the mechanics it takes an average time[Pal+13]

$$T_{\text{coh}} = \frac{1}{\bar{n}_{\text{th}}\Gamma_{\text{m}}}, \tag{2.15}$$

called the *mechanical coherence time*, before a phonon comes and disturbs the quantum state of the mechanics. In the above expression, $\bar{n}_{\text{th}}$ is given by the Bose-Einstein distribution:

$$\bar{n}_{\text{th}} = \frac{1}{e^{\hbar\Omega_{\text{m}}/k_B T} - 1} \approx \frac{k_B T}{\hbar\Omega_{\text{m}}}, \tag{2.16}$$

and the approximation is valid for $k_B T/\hbar\Omega_{\text{m}} \gg 1$, which is generally satisfied for MHz oscillators even at millikelvin temperatures.

2.5 Theoretical Opto-Mechanical Treatment

Now that we have had a look at the physical system, we can treat it more abstractly using the optomechanical formalism. We take the microwave and mechanical resonators to be described as harmonic oscillators with energies $\hbar\omega_r(\hat{a}^\dagger\hat{a}+1/2)$ and $\hbar\Omega_m(\hat{b}^\dagger\hat{b}+1/2)$ where $\hat{a}(\hat{a}^\dagger)$ and $\hat{b}(\hat{b}^\dagger)$ are the MW photon and mechanical phonon annihilation (creation) operators respectively.

As was already mentioned in Sec. 2.3, the resonance frequency of the microwave circuit is modified by the position of the mechanics, such that we write to first order in x:

$$\omega_r(x) \approx \omega_r + x\frac{\partial\omega_r}{\partial x} \tag{2.17}$$

Then the full Hamiltonian of the system is:

$$\hat{H} = \hbar\omega_r\hat{a}^\dagger\hat{a} + \hbar\Omega_m\hat{b}^\dagger\hat{b} - \hbar G x_{zpf}\hat{a}^\dagger\hat{a}(\hat{b} + \hat{b}^\dagger), \tag{2.18}$$

where $G = \frac{\partial\omega_r}{\partial x}$ is the frequency pull-in factor.

The interaction term of the form $\hat{a}^\dagger\hat{a}(\hat{b} + \hat{b}^\dagger)$ is due to the radiation pressure force: the number of photons $\hat{a}^\dagger\hat{a}$ in the MW cavity changes the position of the mechanics. This interaction has been at the center of optomechanical theory and experiments and has recently been demonstrated in superconducting circuits where the mechanical element has been replaced by a low-frequency radio-frequency (RF) resonator[EP18]. This radiation-pressure-type interaction not involving mechanical elements, novel for circuit QED architectures, opens up the way to exploring new phenomena in purely superconducting devices[Gel+19].

The most important parameter when it comes to quantum applications in opto-mechanical systems is the magnitude of the *single-photon coupling rate* $g_0 = Gx_{\mathrm{zpf}}$, the angular frequency shift of the cavity due to vacuum fluctuations of the mechanical resonator. Typically this is very small compared to the cavity linewidth: $g_0/\kappa \sim 10^{-4}$, and single-photon effects such as single-photon blockade[Rab11] remain elusive. However it has recently been experimentally observed that the single-photon coupling can exceed the mechanical frequency[Fog+19].

In order to increase the coupling, a strong bias tone, the *pump*, is applied at an angular frequency $\omega_{\mathrm{L}} = \omega_{\mathrm{r}} + \Delta$. This tone populates the cavity with a large coherent field with amplitude $\bar{\alpha}$ (see Eq. 2.3) and mean photon number $n_{cav} = |\bar{\alpha}|^2$. We now only look at small fluctuations of the cavity field around its average $\bar{\alpha}$, and we rewrite the cavity field operators $\hat{a} = \bar{\alpha} + \delta\hat{a}$ ($\hat{a}^\dagger = \bar{\alpha}^* + \delta\hat{a}^\dagger$). The linearised interaction term of the Hamiltonian is then, to first order in $\delta\hat{a}$ and $\delta\hat{a}^\dagger$:

$$\hat{H}_{\mathrm{lin}} = -\hbar G x_{zpf} \hat{a}^\dagger \hat{a}(\hat{b} + \hat{b}^\dagger) \tag{2.19a}$$

$$\approx -\hbar G x_{zpf}(|\bar{\alpha}|^2 + \bar{\alpha}^*\delta\hat{a} + \bar{\alpha}\delta\hat{a}^\dagger)(\hat{b} + \hat{b}^\dagger). \tag{2.19b}$$

The first term $|\bar{\alpha}|^2$ in Eq. 2.19b is a static displacement of the mechanical resting position, while the second term is a linearised opto-mechanical interaction $(\bar{\alpha}^*\delta\hat{a} + \bar{\alpha}\delta\hat{a}^\dagger)(\hat{b} + \hat{b}^\dagger)$, where the *multi-photon coupling rate* $g = Gx_{\mathrm{zpf}}|\bar{\alpha}|$ is enhanced by the presence of photons in the cavity[Pet+19]. Notice also that the interaction is now symmetric between operators of the cavity and mechanics.

Let us briefly explain the terms in the linearised interaction. The terms proportional to $\delta\hat{a}\hat{b}^\dagger$ and $\delta\hat{a}^\dagger\hat{b}$ correspond respectively to the absorption of a cavity photon with the creation of a phonon, and the annihilation of a phonon with the creation of a cavity photon. The energy difference is then carried away by a pump photon, since at its core this is a 3-quanta interaction, thus these terms can be seen as down- and up-conversion of a pump photon by a phonon respectively. The terms proportional to $\delta\hat{a}^\dagger\hat{b}^\dagger$ and $\delta\hat{a}\hat{b}$ correspond to the creation or annihilation of a cavity photon and phonon pair, where a pump photon is annihilated or created respectively.

The predominance of each of these four terms depends on the position of the pump with respect to the cavity resonance and the relative suppression of the processes by the cavity density of states. In the situation where the cavity is narrow with respect to the mechanical frequency, known as the *resolved sideband* regime, we may choose to enhance the $\delta\hat{a}\hat{b}^\dagger + \delta\hat{a}^\dagger\hat{b}$ or $\delta\hat{a}^\dagger\hat{b}^\dagger + \delta\hat{a}\hat{b}$ by placing the pump red-detuned from the resonance by Ω_{m} or blue-detuned by Ω_{m} respectively.

The classical equations of motion for cavity field and mechanics are (as derived in App. B.20):

$$\delta\dot{\alpha} = \left(-\frac{\kappa}{2} + i\Delta\right)\delta\alpha + iG\bar{\alpha}x - \sqrt{\kappa_{\mathrm{e}}}\delta\alpha_{\mathrm{in}} \tag{2.20a}$$

$$m_{\mathrm{eff}}\ddot{x} = -m_{\mathrm{eff}}\Omega_m^2 x - m_{\mathrm{eff}}\Gamma_{\mathrm{m}}\dot{x} + \hbar G(\bar{\alpha}^*\delta\alpha + \bar{\alpha}\delta\alpha^*). \tag{2.20b}$$

We can see mechanical motion being written onto the light: mechanical motion modulates the MW resonance frequency, creating modulation sidebands on the cavity light, which is then read out from the cavity via Eq. 2.1.

Mechanical manipulation via light

The interaction of light with the mechanics not only leads to the imprinting of the mechanical motion onto the light: the light input into the cavity also allows for the manipulation and modification of the mechanical dynamics. From the mechanics' point of view this interaction causes a steady-state *dynamical backaction* (DBA) which adds a light-induced frequency shift and damping/amplification of the mechanics. The expressions for the *'light-induced' spring effect*, where the mechanical frequency Ω_m is shifted by $\delta\Omega_m$, and the *'light-induced' damping*, where the mechanical linewidth is increased by Γ_{opt}, are given by:

$$\delta\Omega_{\mathrm{m}} = g^2\left(\frac{\Delta + \Omega_m}{(\Delta + \Omega_{\mathrm{m}})^2 + (\kappa/2)^2} + \frac{\Delta - \Omega_{\mathrm{m}}}{(\Delta - \Omega_{\mathrm{m}})^2 + (\kappa/2)^2}\right) \tag{2.21a}$$

$$\Gamma_{\mathrm{opt}} = g^2\left(\frac{+\kappa}{(\Delta + \Omega_{\mathrm{m}})^2 + (\kappa/2)^2} + \frac{-\kappa}{(\Delta - \Omega_{\mathrm{m}})^2 + (\kappa/2)^2}\right), \tag{2.21b}$$

where Γ_{opt} and $\Gamma_m + \Gamma_{opt}$ can assume negative values. We derive the above equations from the linearised interaction Eq. 2.19b in App. B.3.

In Fig. 2.9 we plot an example of DBA for parameters similar to our experimental ones. We see, as is well known, that a red-detuned pump ($\Delta < 0$) leads to broadening of the mechanical linewidth and cooling, whereas a blue pump leads to mechanical amplification.

Once the cavity parameters are known, measurements of $\delta\Omega_m$ and Γ_{opt} as function of Δ gives us a tool to measure the coupling g for a given input pump power (see Sec. 4.4 for measurements). Furthermore if we are able to calibrate n_{cav}, which may not be trivial, we can extract the single-photon or vacuum coupling rate g_0, such that the cavity angular frequency shift caused by the addition of a single phonon to the mechanics is $2g_0$.

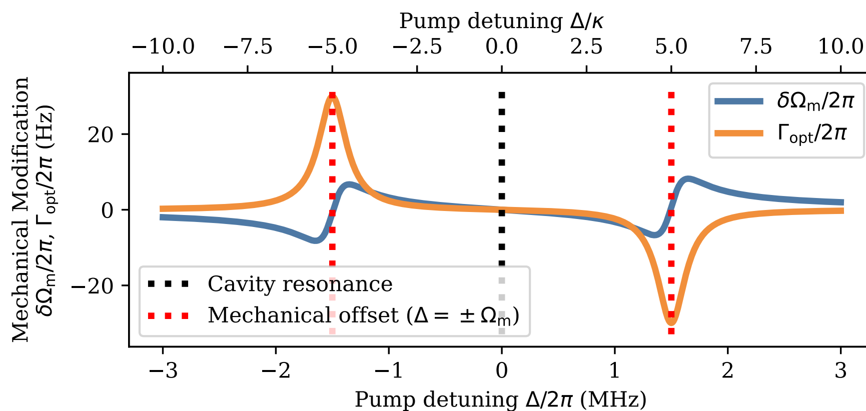

Figure 2.9: Light-induced modification of the mechanical frequency $\delta\Omega_m$ and induced broadening Γ_{opt}. We use $\kappa = 2\pi \cdot 300\text{kHz}$, $\Omega_m = 2\pi \cdot 1.5\text{MHz}$, $g_0 = 2\pi \cdot 1.5\text{Hz}$, and $n_{\text{cav}} = 10^6$: giving $\mathcal{C} = 15000$.

Electro-mechanically induced reflection

An important phenomenon in optomechanics is the appearance of mechanics-induced modifications to the cavity susceptibility, called *opto-* or *electro-mechanically induced transparency*[Sch09; AH10; Wei+10; SN+11; Zho+13]. More recently electro-mechanically induced optical absorption was also demonstrated in an opto-electro-mechanical device allowing for transduction between microwave and optics[Hig+18]. An electromechanically-induced reflection (EMIR) has been used to amplify MW light[Coh+20]. Non-reciprocal devices have also been developed using induced transparencies[Rue+18].

The electro-mechanical system now interacts with two MW tones: one strong *pump tone* which controls the mechanical mode (following the DBA equations 2.21), and one weak *probe tone* which measures the mechanics and for which the cavity reflection is modified in the presence of the mechanics.

In Appendix B.4, we reproduce the derivation for the reflection spectrum of a MW cavity and only present here the result for the case when the pump is red-detuned from cavity resonance by the mechanical frequency ($\Delta = \omega_L - \omega_c = -\Omega_m$). The reflection coefficient for the probe field (detuned by $\delta = \omega_p - (\omega_L + \Omega_m)$ from the pump's upper mechanical sideband) is

$$r_p(\delta) = 1 - 2\eta_c + 2\eta_c\mathcal{C}\frac{\Gamma_m}{\Gamma_m + \Gamma_{opt}}\left(1 + 2i\frac{\delta + \delta\Omega_m}{\Gamma_m + \Gamma_{opt}}\right)^{-1}, \tag{2.22}$$

with $\mathcal{C} = 4g^2/(\Gamma_m\kappa)$ is the (classical) electro-mechanical *cooperativity*, a comparison between interaction strength and energy loss channels in the

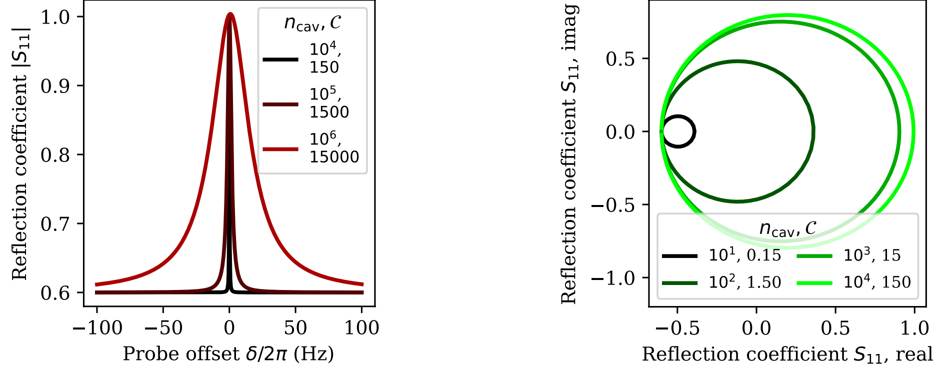

(a) EMIR feature against frequency.

(b) EMIR feature in the complex plane.

Figure 2.10: Computation of the EMIR feature with the same system parameters as in Fig. 2.9 and $\Delta = -\Omega_m$. a) As the pump power is increased, the EMIR feature increases in width and is slightly blue-shifted, as expected from the DBA equations. b) In the complex plane, the EMIR feature takes the shape of a circle. The circle's diameter reflects the interaction strength and is given by $2\eta_c \mathcal{C} \frac{\Gamma_m}{\Gamma_m + \Gamma_{opt}}$, in Eq. 2.22.

system. A cooperativity comparable or larger than unity enters the regime where electromechanical effects, such as DBA and EMIR, become visible. We compute an example of EMIR feature in Fig. 2.10.

For quantum applications the cooperativity must further be larger than the number n_{th} of quanta in the thermal bath as given by Eq. 2.16. Thus the *quantum cooperativity* $\mathcal{C}_q = \mathcal{C}/n_{\text{th}}$ comparable or larger than unity is the regime where quantum coherent interactions take place in the "quantum enabled" system.

Chapter 3

Device Fabrication

This chapter on device fabrication describes the steps we have gone through in the development of the cleanroom processes to fabricate the devices measured in Chapter. 4. We explain some of conceptual developments towards the fabrication of superconducting resonators, we show the main fabrication process flows, and discuss some of the processing failures and modifications along the way.

3.1 Chronology of Device Fabrication

First we look back at the time period of this PhD project and make out some larger sections, highlighting different directions in which the activities have gone. A number of different directions have been explored in this project (and are not reported here) and the final process and designs presented in this thesis are recent with respect to the time-span of this PhD. The author of this thesis not having any previous experience in cleanroom fabrication, the first year was spent learning to use the cleanroom tools with the guidance of Anders Simonsen, Yeghishe Tsaturyan and the staff of the DTU Nanolab cleanroom.

July 2015 - April 2016

- Deposition attempts of the first superconductor MgB_2, which should allow for experimental operation at approx. 4 K (see Sec. 3.6).
- Fabrication practise with Anders Simonsen's integrated room-temperature transducer process flow.
- Simulations of 3D microwave cavity systems in COMSOL.

April 2016 - March 2017

- Change to the deposition of Nb and NbN (see Sec. 3.6), as they are better understood superconductors than MgB_2 and avoid process contamination due to Mg.
- Improvements in deposition cleanliness of Nb and NbN: Ti gettering to reach lower base pressure and understanding N_2 reactive sputtering (monitoring the "target poisoning").
- January 2017: First measurements of the hollow Nb 3D box cavity.
- November 2017: Measurements of the NbSn coated 3D Nb box cavity, coated at Cornell University, showed quality a factor of 10^6 at approx. 4 K.

March 2017 - June 2019

- NbTiN reactive sputtering in Lesker, initially with Ti gettering.
- April 2017: Measurements of Gold metallised patterned membranes at room temperature (RT).
- March 2018: Measurements of Gold IDCs in Nb cavity at RT for participation ratio.
- July 2018: Correction of the N_2 gas flow calibration in the sputtering tool gives the correct value N_2 partial pressure for reactive sputtering.
- February 2019: Dielectrically coupled membrane electro-mechanics devices measured (H-antenna with IDC).

June 2019 - Present

- Commercially available NbTiN thin films, deposited by StarCryo Electronics in New Mexico, USA, lead to better superconducting resonators than any films deposited in the cleanroom.
- July 2019: Change to loop-gap resonators and vacuum-gap capacitors, Al metallisation of membranes, for increased coupling between membrane motion and superconducting resonator.
- January 2020: Change to low-power SF_6/O_2 based etch of NbTiN (instead of high-power Cl_2 etch), achieves very clean surfaces required for flip-chip assembly.

- March 2020: Flip-chip epoxy changed from Stycast 2850FT to Araldite 5 min for better control of the flip-chip gluing.

3.2 Initial Devices and Fabrication Processes

Moderate success at depositing NbTiN in Lesker

The main sputtering tool in the DTU cleanroom until now is a Lesker system with 6 targets of 2″ diameter and gas lines for reactive sputtering with O_2 and N_2. We started depositing NbTiN thin films by reactive sputtering from a NbTi target (67/33 at % by weight Nb/Ti, corresponding to equal molar quantity of Nb and Ti). To find the correct deposition parameters, we mainly varied the N_2 partial pressure: the fraction of the gas flow into the chamber which is N_2. In the tool, the sputtering pressure is stabilised by varying the Ar flow rate into the processing chamber, while the N_2 flow rate is set to a fixed percentage of the Ar flow rate. We always deposited at room temperature and quickly settled for a sputtering pressure of 2 mTorr after discussion with members of the Center for Quantum Devices (QDev) at the Niels Bohr Institute.

Unfortunately it took several months to find thin film deposition parameters allowing us to measure the first superconducting resonators: at the time we only had access to a 4 K flow cryostat and were 'in the dark' without any measurable superconducting film from which to improve the deposition parameters. In particular, it was realised about 6 months after starting to deposit NbTiN that the Lesker tool's N_2 flow rate measurement was not calibrated properly which meant that the actual flow rate was about 40% lower than displayed one. The lower effective nitrogen flow rate explained why we did not measure superconductivity at 4 K despite using deposition parameters on which authors in the literature agreed would work[MMN03; Dra14; Shi+10].

Once the N_2 flow rate was properly calibrated we were able to measure our NbTiN microwave resonators exhibiting a jump in quality factor at low temperatures and our measurements of the room temperature sheet resistivity of the films were in agreement with the literature: sheet resistivity is a good proxy for the quality of a NbTiN film where a minimum around 17% N_2 partial pressure (with respect to Ar pressure) should give high-quality films. We note however that the resistivity of our films were at least a factor 4 higher than commercially available films which meant we still needed to improved deposition parameters or that the tool was contaminated by

magnetic impurities. Films available from Star Cryoelectronics have a sheet resistivity around 12–16 $\Omega/\square$ (for a 100 nm thin film), whereas we measured resistivities around 60 $\Omega/\square$.

Microwave resonators with IDCs

For characterisation of our microwave circuit, we first fabricated Si chips with patterned superconducting thin films to be placed inside of a 3D superconducting Nb cavity. The first iteration inspired by other groups in the field[Yua+15; Nog+16]: we define a circuit where the mode is hybridly hosted on the conductor on the chip and on the walls of the 3D box. This is an interesting architecture since it in principle allows very high power handling with current running on the walls of the 3D box[Pet+19]. In the absence of a membrane, we used a planar inter-digitated capacitor (IDC)[ID04] to built the resonant circuit, where the inductor is the loop made by the 3D box walls. We show a fabricated IDC made of NbTiN on a Si substrate in Fig. 3.1. In these early generations, we also used fused silica, and sapphire substrates because we feared excess MW loss in Si substrates, but finally settled for high-resistivity Si: Si substrates have the advantages to be readily processed using standard cleanroom processing techniques, especially deep reactive ion etching (DRIE), and are more easily cut into chips than sapphire, using a dicing saw. High-resistivity Si had also been shown to exhibit low MW loss at cryogenic temperatures[Nie+14].

To ensure we understood the design, we measured IDC antennas made of a gold thin film (on a fused silica substrate) to determine the MW resonance frequency and check it with simulations. In Fig. 3.2, we show measurements where we place chips with different size IDCs to see how its capacitance C_{IDC} modifies the resonance. We can see that for increasing on-chip capacitance, the resonance frequency goes down as suggested by $\omega_c = 1/\sqrt{L(C_{IDC} + C_p)}$ which allows us to extract the capacitance in parallel C_p similar to the value found in the literature (see the “Steele” entry in Table 2.1).

We fabricated NbTiN antennas using a process flow similar to the final one layed out in Sec. 3.3. We were able to measure superconducting MW circuits at 4 K using this 3D architecture and used these results to attempt at optimising the superconductor deposition in the cleanroom. However the quality factors of the resonators where never even close to what had been reported in the literature for this choice of material or architecture: internal quality factors of $100,000$ should be possible[Bru+15; Bar+08], whereas we typically measured a few hundred to $3,000$. From private communications by the group of Yasunobu Nakamura, we found out that alignment of the two halves of the 3D cavity around the chip was very important for low loss:

(a) The antenna chip is placed in between two halves of a 3D box such that the currents flow on the chip and on the walls.

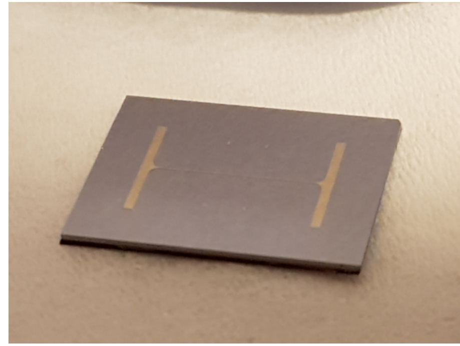

(b) Optical image of the 'H-resonator' on a silicon chip.

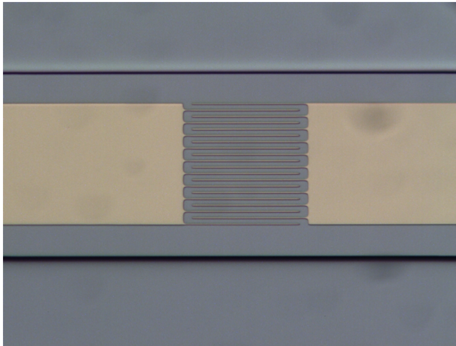

(c) Close-up of the IDC at the centre of the H-antenna: here with 10 pairs of 80 µm long fingers, with 8 µm finger period.

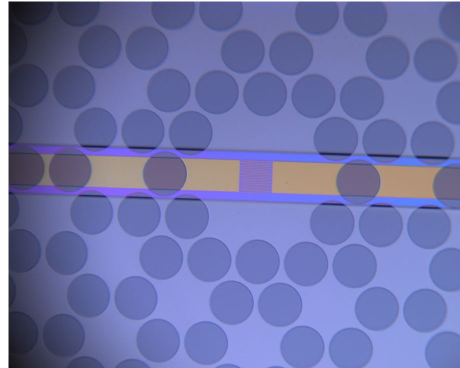

(d) We place and glue a SiN membrane over the antenna chip such that the membrane defect hovers over the IDC.

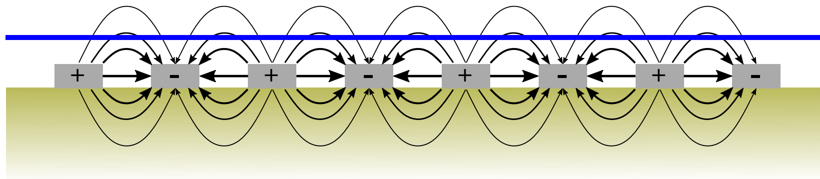

(e) Sketch of the electro-mechanical coupling scheme where the out-of-plane field of the IDC permeates the dielectric membrane (shown in blue).

Figure 3.1: Optical images of chip with the superconducting IDC chip, placed inside a 3D cavity with a membrane in flip-chip assembly.

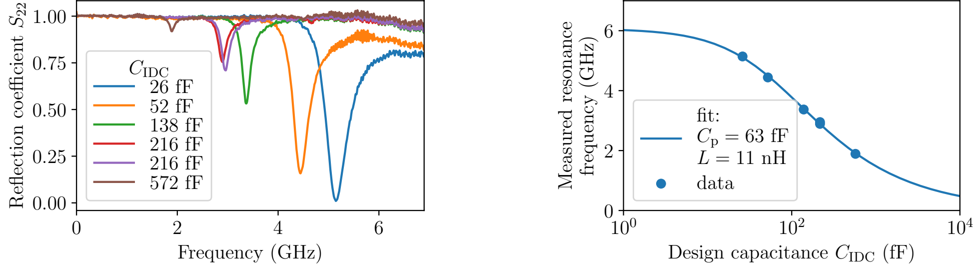

(a) Measured spectra when placing chips with varying IDC capacitance inside the 3D cavity.

(b) By fitting the MW frequency to the IDC capacitance we extract a parasitic capacitance.

Figure 3.2: We measure the resonance frequency of a MW resonator at room temperature, where we place chips with different IDC capacitance (made from a gold thin film) inside a 3D cavity. We can then extract the capacitance in parallel with the IDC.

we had indeed one single time measured $Q_I > 10,000$ but our assembly did not allow us to reproduce it. Eventually we moved on to using a loop-gap resonator, which was expected to yield more reproducible MW resonator quality.

Electro-mechanical device with IDC dielectric coupling

Having fabricated loop-gap resonators with IDCs, we proceed to attempting a flip-chip assembly using a membrane in order to make use of the dielectric coupling between the (non-metallised) membrane and the electric fields coming out of the plane of the IDC. The electric field amplitude decays exponentially away from the plane of the IDC[Cap+20], thus out-of-plane displacement of the membrane modifies the capacitance of the IDC giving rise to an electro-mechanical coupling. An image of a membrane hovering over an IDC is shown in Fig. 3.1.

Characterisation measurements were performed on this device at 4 K following procedures detailed in Chap. 4. In particular, we extracted a single-photon coupling rate $g_0/2\pi = {\sim}6\,\mathrm{mHz}$, which corresponds to a membrane distance of 1.3 µm above the IDC, based on simulation. The use of an IDC capacitance severely limits the achievable coupling because most of the electric field between the IDC fingers lives in vacuum or in the high-dielectric constant substrate and only a very small amount permeates the membrane. In particular, since the mechanical quality factor of our mem-

branes is inversely proportional to the thickness of the membrane[Tsa+17], we have a difficult trade-off between larger coupling (thicker membranes) and higher mechanical Q (thinner membranes). The experiments we wish to perform require a much larger single-photon coupling, therefore we moved to a vacuum gap capacitor coupling using a metallised membrane. We now describe the fabrication of such a device.

3.3 Fabrication of the Loop-Gap Resonator

The superconducting microwave resonator used for a large part of this thesis is a square loop which is interrupted on one side by a gap in the conductor: this geometry is known as a loop-gap resonator (LGR). We show images of its different parts in Fig. 3.3. The gap is set to 10 µm, which should be much smaller than the dimensions of the membrane metallisation in order to not sacrifice overlap area. The LGR has rounded corners to reduce current crowding, which can lead to energy dissipation in regions of large current[Hen+12; Hor+12].

The Si region on the outside of the loop and on its inside is etched away to create a recess of depth 28 µm. We keep a distance of about 10 µm from the conductor to the edge of the recess. In parts of the LGR which are not in the overlap region with the membrane metallisation, we reduce the width of the conductor and correspondingly the edge of the recess such that we minimise any area which could be close to the membrane (once the two chips are assembled): this reduces the risk of any particles laying on the superconductor and touching the membrane. This narrowing of the conductor can in principle also be used to tune the kinetic inductance of the film; however for a $\sim$100 nm thick NbTiN film, significant kinetic inductance is only seen for a conductor width on the order of 1 µm or less[Xu+19; Sam+16].

Spacing pillars are placed a few millimetres away from the LGR gap, such that they are far enough away from the membrane edge, and give a nominal membrane-to-LGR distance of 300 nm. Our membrane chips are squares with side length 10 mm, the pillars thus contact the membrane chip close to its edge: this can in principle be used to push the membrane further in and reduce the vacuum capacitor gap. While being an interesting idea, applying pressure to the flip-chip during glue curing has not given the desired outcomes: this chips' intrinsic curvatures relax the flip-chip and the vacuum gap is not preserved once the pressure is released.

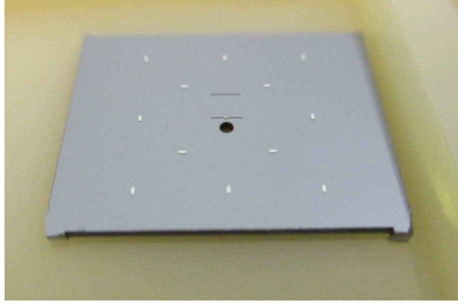

(a) Optical image of one resonator chip with the LGR in the middle and spacing pillars at the periphery.

(b) SEM image of the NbTiN loop-gap resonator with etched recess and optics through-hole. The side dimension of the square loop is 1500 µm and the diameter of the optics hole is ∼500 µm.

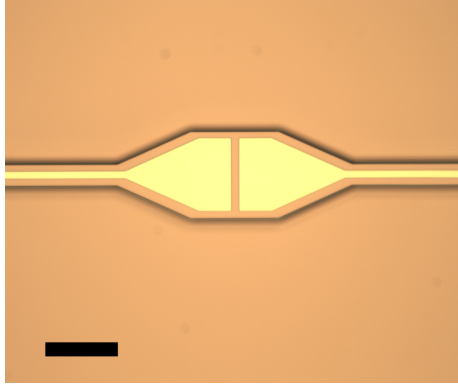

(c) Close-up of the 10 µm gap in the resonator loop which is bridged by the metallised membrane. The black scale bar is 100 µm long.

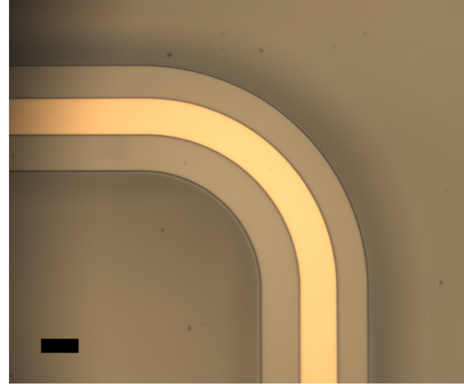

(d) Close-up of the edge of the recess at a corner of the resonator, we have left a ∼10 µm distance between the superconductor and the recess. The black scale bar is 10 µm long.

(e) Optical image of the 100 µm × 300 µm, 300 nm thick Al spacing pillars used to define the flip-chip distance.

(f) Image of a superconducting NbTi wire loop, shaped by hand, used as incoupling inductor to the LGR cavity.

Figure 3.3: Optical and SEM images of a chip with the superconducting resonator, spacing pillars and recess to protect the membrane during flip-chip assembly.

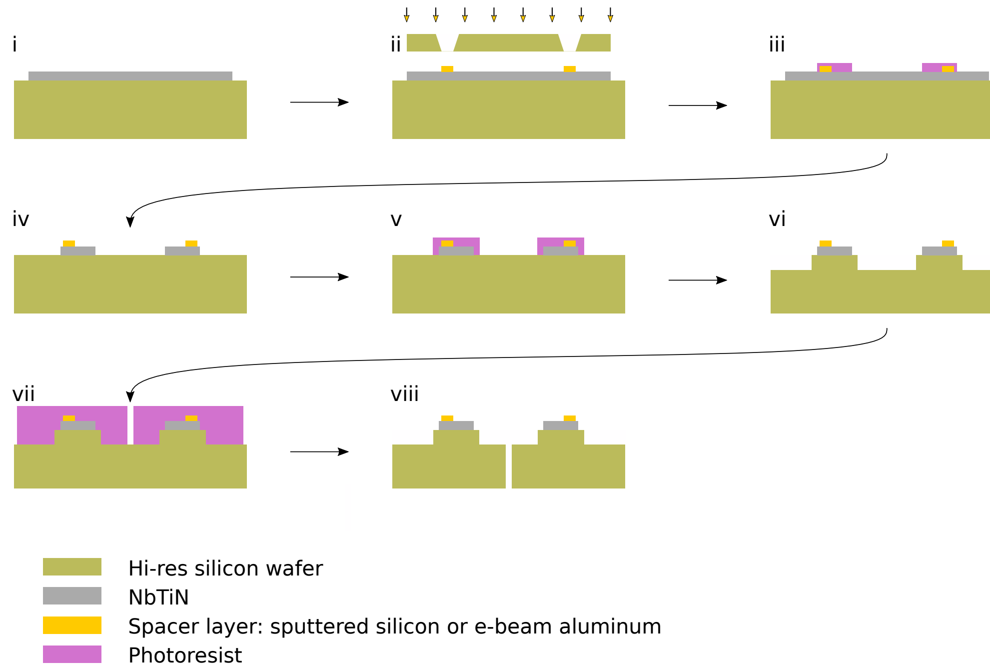

Figure 3.4: Fabrication flow for the superconducting NbTiN resonator chip for the flip-chip device.

Fabrication flow

The latest process flow for fabricating superconducting resonators made of NbTiN is presented in diagram form in Fig. 3.4.

i) We start with a high-resistivity (>10 000 Ω cm) Silicon wafer from Topsil (Denmark). After cleaning the wafers in a Piranha solution or using the RCA cleaning sequence, we send the wafers to be coated with 100 nm NbTiN at the Star Cryoelectronics foundary (Santa Fe, New Mexico, USA). Films have a room temperature sheet resistance in the range 10–15 Ω/□.

ii) Back in the DTU cleanroom, we use a shadow mask made from a Si wafer etched in potassium hydroxide (KOH) to define spacing pillars. We manually align the flats of the shadow mask wafer with our device wafer, hold them in place with a rigid Aluminium tape. Then we evaporate a material such as Aluminium from an e-beam tool to define

300 nm thick, rectangular spacing pillars. This defines the nominal distance of the membrane above the superconducting resonator.

The use of a shadow mask is important here to protect the superconducting film. An alternative patterning of the Al spacing layer could have been done by coating the entire wafer with Al and etching it away to define the pillars. However, using a TMAH-based developer (Microchemicals AZ 726 MIF Developer) to etch Al seems to damage the NbTiN film surface: we indeed measured that a 10 min exposure of the superconductor to TMAH increases its sheet resistivity by 10% and worsened the uniformity of the subsequent dry etch as well as required a slightly longer etch time.

iii) Next we use ultra-violet (UV) photo-lithography to define the MW resonator pattern in a 1.5 µm thick negative photo-resist (Microchemicals AZ nLOF 2020). Adhesion promotion with HMDS is used prior to resist spinning and baking. Then the resist is exposed using a maskless aligner (Heidelberg Instruments MLA100), post-exposure baked and developed with the TMAH-based solution mentioned above. Here we over-expose the negative resist to avoid negative sidewalls in the resist after development, which could lead to an unfaithful transfer of the resist pattern due to excessive under-etching of the resist.

iv) Etching of the superconductor is done in an ICP etch tool. Once the wafer is loaded, we first run a descum O_2 plasma clean to remove resist residues, which are more likely when using a negative tone resist. We use an SF_6 and O_2 based chemistry at low power (250 W) to etch NbTiN. This step has turned out to be *the* most important one when it comes to cleanliness of the superconductor surface: resist burning at this step has proven very difficult to remove using any solvent-based sonication stripper. To further reduce this risk, we etch the film by splitting up the etch from one long 90 s etch into three shorter 30 s etches with ∼3 min cooling time in between. The resist is then stripped in a solvent (Microposit Remover 1165) bath with sonication for ∼30 min. Again to avoid damaging the superconductor, we choose to not use O_2 plasma stripping as exposure to the plasma was seen to visibly change the film colour. The effect of O_2 plasma on the superconducting quality was not investigated.

v) Since we will eventually assemble two chips using the flip-chip technique, we wish to protect the membrane by defining a recess into the resonator chip, such that we reduce the chance of there being large

particles that could contact the membrane. Similar to step iii), the pattern of the recess is defined by exposing a 4 µm thick layer of nLOF with the mask-less aligner.

vi) The recess into the Si wafer is etched with the Bosch process in another ICP tool. We run an O_2 plasma clean, then run 60 cycles of the anisotropic process and clean again with an O_2 plasma after the etch. The etch depth after 60 cycles is approximately 28 µm. The second plasma clean is absolutely necessary to prepare the exposed Si surface to the next resist spinning step: indeed the deposition of the passivation layer during the Bosch process worsens the photoresist's adhesion to the Si substrate. This post-etch plasma clean is requires despite the fact that the Bosch process finishes with an etch step. The resist is similarly stripped in solvent with sonication.

vii) We then spin a thick layer of positive photoresist (Microchemicals AZ 4562) to cover the structures now that we have a deep recess: first a 20 µm thick layer, then another 10 µm. The rehydration of the resist after baking is done by leaving the wafer to rest overnight. Then we expose the resist by using a combination of a masked aligner for the grooves delimiting the chips (the pattern of which is not likely to change over time) and mask-less aligner for the optics through hole (the design of which we can change every time). Development of this thick layer requires about 10 puddle developments of 1 min each in the TMAH solution.

viii) The final etch step is again done using a Bosch process, where we first etch almost the entire way through the wafer, only stopping approx. 50 µm before reaching the bottom face of the wafer. Then we bond the wafer to a carrier using crystal bond, to avoid damaging the chuck in the tool, and finish etching through our device wafer. We strip the resist again and dice the wafer into chips by breaking them off along the etch-defined grooves with the help of hand-held cleaving pliers and a diamond pen.

3.4 Phononic Membrane Device Fabrication and its Metallisation

The patterned membranes are made from stoichiometric Silicon Nitride (Si_3N_4) deposited to yield high stress (approx. 1.2 GPa) and are patterned with standard UV lithography and dry-etching techniques to create a phononic

shield with one or several defects which host localised modes. The membrane is finally released in a solution of hot potassium hydroxide (KOH), which removes the Si substrate underneath the Si_3N_4 thin film and leaves only the suspended patterned membrane. The process flow was first developed by Yeghishe Tsaturyan[Tsa+17], and more recently augmented by Eric Langman. Since we have also used this process in the cleanroom, we briefly sketch it out here and then elaborate on the process which we have developed for metallising selected regions of the membrane.

Once the membranes have been released and broken off into chips of dimension 10 mm by 10 mm, each hosting one membrane, each chip is equipped with a shadow mask covering up the entire membrane except for a small opening in the centre which allows for the depositing of metals in that region. The shadow mask assembly is made more convenient by the use of self-alignment holes on the membrane front side and corresponding pillars on the shadow mask, proposed by Yeghishe Tsaturyan. Assembly is done by sliding the mask on to the membrane chip until the two fall into place, aligned by the self-alignment structures.

The mask and membrane can be held in place by rigid Aluminium tape. However, we found it generally sufficient to hold them in place with soft clamps used to mount samples in the e-beam tool, as depicted in Fig. 3.6. If Aluminium tape is used, the adhesive should be removed with ethanol. After Al metallisation, the membranes are annealed in N_2 at 400 °C to increase the tensile stress of the metallisation to 300 MPa[YPR12].

Fabrication flow for the membrane and its metallisation

A fabrication flow in diagram form is given in Fig. 3.7.

i) We start with a clean crystalline Si, double-side polished, 500 µm thick wafer which is coated in stoichiometric Silicon Nitride using a low-pressure chemical vapour deposition technique, which deposits the high-stress material at 790 °C. We deposit films in the range 20 nm to 70 nm for metallised membranes.

ii) We then pattern both sides of the wafer with standard UV-lithography and CF_4/H_2-based dry-etching. We first process (pattern, etch and resist-strip) the bottom side while protecting the top side with photoresist, then process the front to transfer the phononic pattern. During the front side patterning we also open holes on the four corners of the membrane chips, which server as the self-alignment structures

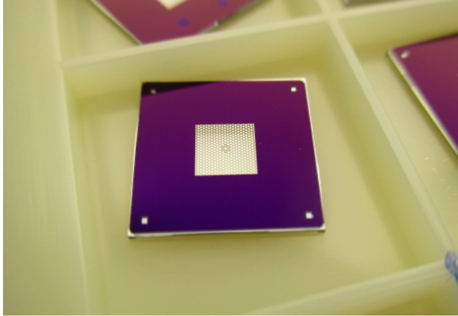

(a) Optical image of a released and broken-off membrane chip.

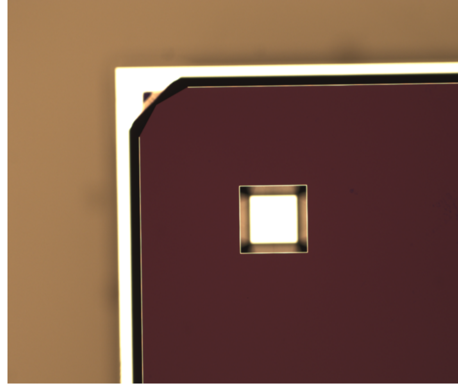

(b) Zoom in on one corner of the membrane chip where we placed a self-alignment hole.

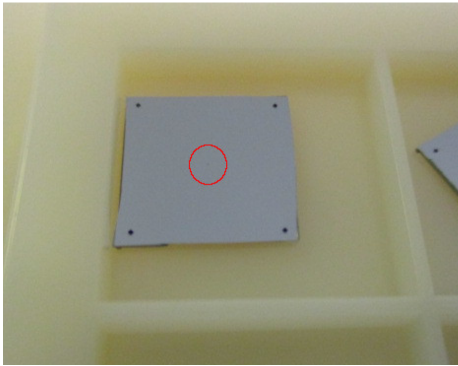

(c) Optical image of a shadow mask, where we circled in red the location of the opening.

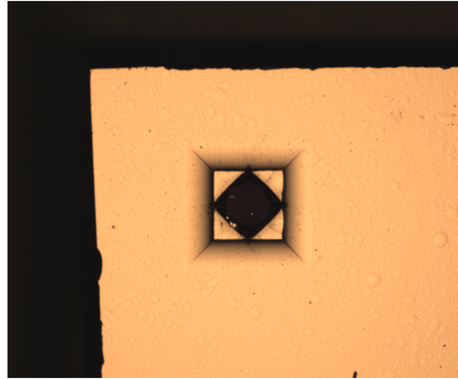

(d) Close-up of the corner of the shadow mask chip with the alignment pillar.

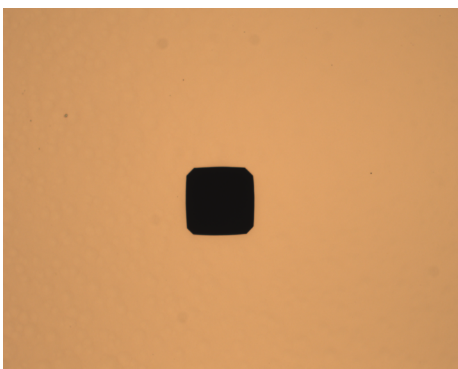

(e) Close-up of the opening, centred on the shadow mask

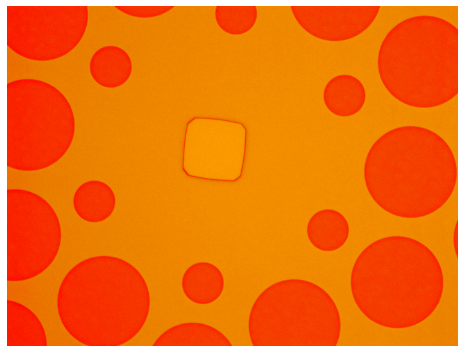

(f) Optical image of a metallised defect.

Figure 3.5: Optical images of patterned membranes and a shadow mask used to metallise a defect of the membrane.

(a) Clamping of one shadow mask and membrane assembly at the upper side of the holder of the e-beam tool.

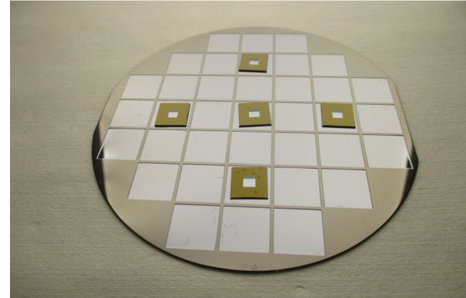

(b) Carrier for the annealing of Al-metallised membranes in a furnace at 400 °C.

Figure 3.6: Optical images of membrane and shadow mask used to metallise a defect of the membrane.

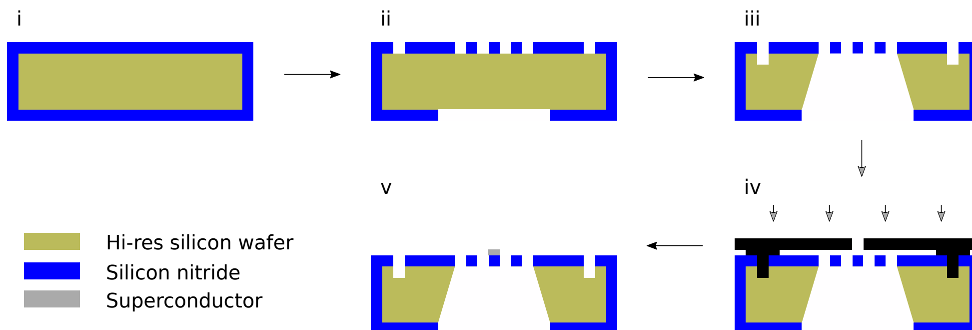

Figure 3.7: Fabrication flow for the Si_3N_4 patterned membrane and its metallisation.

for the shadow mask. Both sides also have patterns for chip-defining grooves, which will help breaking of the wafer into 10 mm × 10 mm chips.

iii) The Si substrate is anisotropically etched in a KOH solution at 80 °C from the bottom side: the top patterned side is protected by a back-side protecting holder. Precise timing of the etch is necessary at this point to take the wafer out from the holder right before all the substrate is etch through, then the etch is finished by placing the wafer back in the bath without back-side protection. Once the membranes are released we continue the etch for 60 min to etch the alignment holes by at least 60 µm. Then the wafer is cleaned in a Piranha solution and rinsed in water.

The clean wafer is carefully broken into chips along the grooves. Splinters of Si can fall on the membranes at this stage, they can sometimes be removed by a dip into a beaker with isopropanol, followed by a rinse in de-ionised water.

iv) Next, each membrane is assembled with a shadow mask by self-alignment. And the metal is deposited: either we deposit Al by e-beam deposition or NbTiN by reactive sputtering. We target 20 nm thick metal layers and use a low deposition rate of 2 Å s^{-1} for the e-beam process.

v) After removing the shadow mask, the Al is annealed in an N_2 furnace at 400 °C.

After some practise, the metallisation and annealing steps can be done with > 90% yield and the largest loss of samples happens at the release step in KOH where the additional 60 min over-etch seems to break membranes and broken pieces of Si_3N_4 then fall on other otherwise undamaged membranes, making them unusable.

Fabrication flow for the shadow mask

Shadow masks are fabricated following the process flow depicted in Fig. 3.8.

i) We start with a clean crystalline Si, double-side polished, 500 µm thick wafer which is coated in stoichiometric SiN on both sides. Thickness of the LPCVD nitride is not important here, 30 nm or more is enough to withstand the BHF dips done throughout the processing.

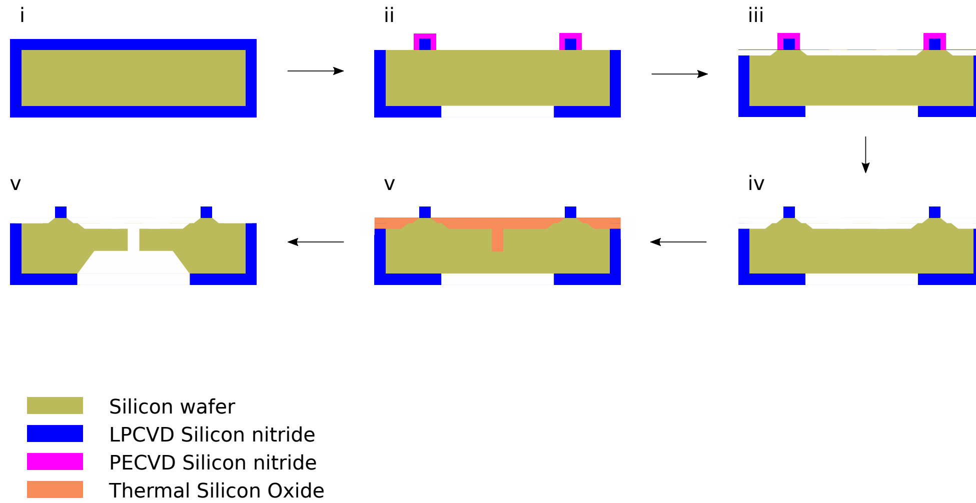

Figure 3.8: Fabrication flow for the shadow masks used for membrane metallisation.

ii) We pattern the back-side LPCVD nitride with square openings, and the front side with squares which will give the pillars. We then coat the front side with PECVD SiN, choosing a recipe which gives good resistance to KOH etch, but has a sufficiently high etch rate in BHF.

The following two etch steps in KOH separated by a BHF dip will allow us to form the pillars while also creating a recess in the membrane area. The pillars then only contact the membrane frame and the released membrane never touches the shadow mask at any point.

iii) We use a back-side protecting holder to only etch the top side of the wafer in 60 °C KOH. We first etch the substrate for 10 min: this effectively defines the recess which is 3 µm deep.

iv) We strip the PECVD SiN from the front side in a BHF dip and etch the Si substrate for another ∼180 min to define the ∼60 µm high pillars. During this time the recess continues to be etched such that it still is ∼3 µm below the base of the pillars. The wafer is taken out of the holder and cleaned in Piranha. Since we are etching crystalline Si in KOH the sides of the pillars have a characteristic angle of 54.7°, this angle matches the angle of the walls in the corners openings on the membrane chips.

v) We now define the mask opening used for metallisation by UV lithography of a 10 µm thick, positive tone AZ 4562 resist and etch the Si in a DRIE Bosch process for 80 cycles, giving ∼50 µm deep holes. We then protect the front side with a thick ∼500 nm thermal SiO_2 layer using an oxidation furnace (with a preceding RCA clean step to be allowed in the furnace). The wafer is again placed in a holder which this time protects the top side, and we strip the oxide from the back with a BHF dip. The oxide layer on the front protects that side from etching in the next KOH step.

vi) We open up the back side window by etching the substrate in 80 °C KOH for 240 min until we reach the front side opening hole, thus creating a hole through the shadow mask chip allowing for deposition of metals. The oxide on the front side is stripped, the wafer cleaned again in Piranha and the shadow mask chips (squares of side length 10 mm) are broken off from the wafer.

Metallisation with NbTiN

In addition to Al metallisations which ended up being the more successful technique, we have also attempted metallising the membrane with NbTiN from the sputtering tool. It is for the sputtering technique that the depth of the recess on the shadow masks may be of importance: grains of the material ripped out of the target by the ionised Ar gas, do not move in straight lines through the plasma in the chamber. Therefore, too deep a recess could allow for the material to undercut the mask opening: that is to deposit on the membrane in a region larger than the opening would allow, in particular we feared this could lead to a gradient of material thickness on the edge of the metallisation. For recess depths of a few microns, this did not seem to be a problem, as can be seen in Fig. 3.9(b). A gradient in thin film thickness is, however, visible if the substrate holder is not rotating during sputtering: this is due to the target-substrate geometry inside the sputtering tool where the material is deposited on the membrane at an angle. Rotating the substrate during deposition ensure a more uniform metallisation.

What can also be seen from Fig. 3.9(a) is that the deposited film using the usual parameters has a compressive stress: which can be seen in the fact that the film is buckling (that is crumbling onto itself giving a 'wavy' pattern). Investigations into obtaining higher stress in sputtered films by tuning of process temperature and pressure where then done by Eric Langman, where he found that increasing the membrane temperature

(a) The NbTiN film on a thin 30 nm membrane exhibits buckling, which suggests compressive stress.

(b) We sputtered NbTiN without rotating the substrate, which resulted in a gradient in deposition thickness.

Figure 3.9: Optical images of a metallisation made of sputtered NbTiN.

to 400 °C allows us to also have tensile stress in the NbTiN film of around 300 MPa. The superconducting properties of these films deposited at higher temperatures were, however, not investigated.

At cryogenic temperatures, membrane metallisations with Al resulted in superconducting and mechanical quality factors that are large enough for our applications. Therefore, we decided to choose the easier fabrication involving Al rather than NbTiN.

3.5 Flip-Chip Bonding

The final step in the fabrication of electro-mechanical devices is the assembly of the superconducting resonator chip with the metallised membrane. Proper assembly requires horizontal alignment to place the metallisation over the gap in the resonator and vertical pressure to reach the small distance as set by the spacing pillars deposited on the resonator chip. Finally the two chips must be glued together in a way which keeps the distance between the two. To make the task easier we use a flip-chip bonder (Dr Tresky 3000 FC/DA) at the packaging lab of the DTU cleanroom. A picture of the flip-chip bonder and a close-up of the vacuum suction used for placement of the membrane are shown in Fig. 3.10. Horizontal alignment and vertical pressure is best done by turning and pulling a knob by hand, which has a limited precision (approx. 5 µm horizontally), but are enough for our current purposes.

The resonator chip can be placed on a bottom stage equipped with horizontal translation, while the membrane chip is turned membrane facing

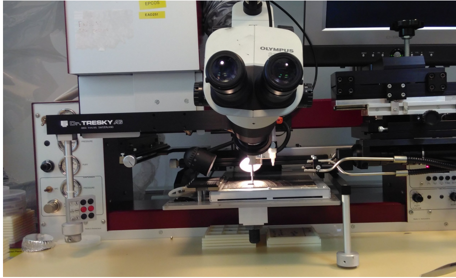

(a) Overview of the flip-chip bonding tool with its microscope, illumination and bottom translation stage.

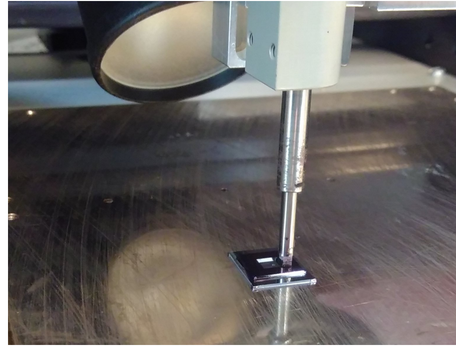

(b) Close-up of the vacuum suction holding a membrane ready to be aligned to a resonator chip.

Figure 3.10: Photographs of the flip-chip bonding tool.

down and held by a “finger” with vacuum suction at a corner of its frame. The membrane can be lowered close to the resonator and aligned horizontally, by using the microscope and looking through the thin transparent membrane, until the metallisation is above the gap in the LGR.

Then the vacuum finger is used to apply pressure to reduce the membrane distance and is held in place while the glue is applied and cured. We have used two different epoxies to bond the chips: Stycast 2850FT with catalyst 24LV, and Araldite 5 min. Both are two part epoxies with different working and curing times: 30 min and 24 h for the first epoxy, and 5 min and 30 min for the second. Tuning of the epoxy viscosity is particularly important at this step: since the distance between membrane and resonator chips will be ∼30 µm (the recess depth on the resonator chip, apart from at the spacing pillars which make direct contact), the epoxy applied on the edge of the membrane frame will be pulled in between the chips by capillary forces, towards the membrane and may reach the membrane (see Fig. 3.11).

We can tune the epoxy viscosity by waiting a certain amount of time after mixing the two components before applying the epoxy to the chips, in such a way that the chips are pulled together but without collapsing the membrane onto the bottom chip.

When approaching the membrane close to the resonator, we see an optical interference pattern made by the reflections of the membrane and the superconducting film. At first, the colours of the patter are faint and they become more intense as the distance is reduced. As we go closer, the colours cycle from long wavelength colour to shorter wavelengths; in that way we can infer whether parts of the membrane are moving closer or away from the resonator chip: both during our manipulation and during application

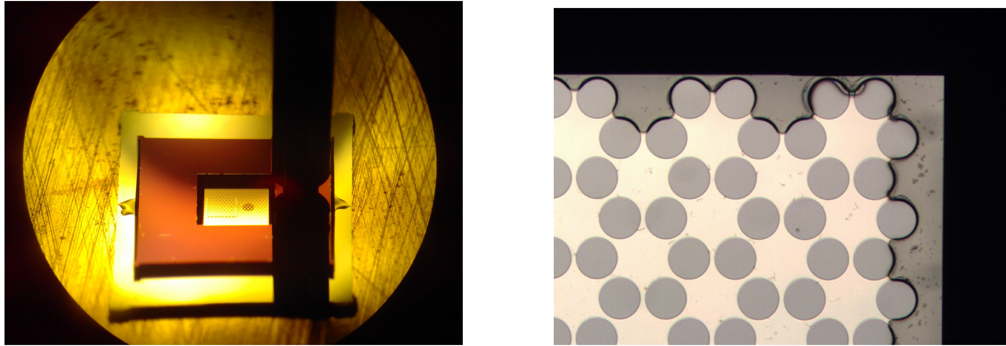

(a) The epoxy is applied at the edge of the membrane frame to bond to the chip underneath (Taken through the microscope objective of the bonder).

(b) Capillary forces may pull the epoxy in, reach the membrane and compromise the mechanical properties, damage or collapse it.

Figure 3.11: Optical images of the application of epoxy to bond the flip-chip assembly.

of the epoxy, we can deduce whether the membrane is pulled in or pushed it away.

When the membrane distance is below the half-wavelength of any visible light, the interference disappears. Furthermore, when the membrane contacts the resonator, a distinct colour appears: a deep blue for 67 nm SiN membrane. These interference colours give further information as to the placement of the membrane. We show microscope images of these patterns in Fig. 3.12. A collapsed membrane can be confidently identified by this dark blue colour of the contact region, complemented by a strong colour gradient (indicating a distance gradient) where the membrane is not contacted but close to the surface (see Fig. 3.12(b)). If a resonator surface is dirty (typically with photoresist residues that were not removed in a solvent bath), this grain of dirt can contact the membrane and be identified by a colour gradient around the contact point (see Fig. 3.12(c)).

One must be especially careful of membrane collapsing, when it contacts the resonator. This may damage the membrane by breaking individual tethers or even rip the entire structure: membrane rupture also contaminates the resonator chip with SiN shreds which means it cannot be reused for another flip-chip attempt. Often it is however possible to pull the membrane off undamaged, provided we pull exclusively vertically in a very controlled manner. Unfortunately the membrane does, in this case, have a tendency to collapse again at the same location, the cause of this is still unclear. While the same resonator chip can be reused, it does mean we must use a different membrane.

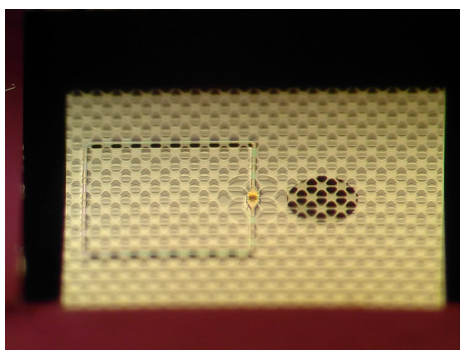

(a) A gradient of interference colour indicated the two chips are at an angle with respect to each other. Absence of colour on the left side means the chips are very close (Taken through the microscope objective of the bonder).

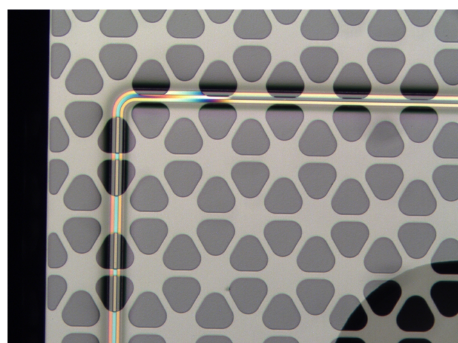

(b) The dark blue colour indicates the membrane is contacting the superconductor on the top right side, with a strong colour gradient on the top left.

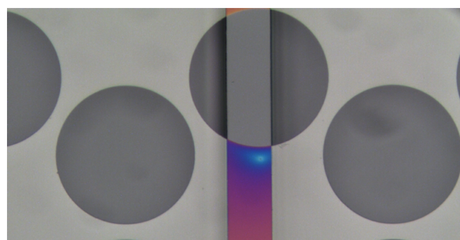

(c) Optical image of the interference patter when a resist residue contacts the membrane, giving a strong circular colour gradient around the contact point.

Figure 3.12: Optical images showing the interference pattern between a 67 nm thick SiN membrane and the NbTiN resonator after the flip-chip assembly. The colours give an indication of the distance between the two chips or whether there has been contact.

While we had some success with applying pressure on the flip-chip during application of glue and curing, we saw that the flip-chip ultimately relaxes to a distance different from which it was held in place. We attribute this to the intrinsic curvature of the Si chips, and we were told that other groups had seen similar relaxations. Therefore, our most recent and most successful gluing attempts were done by dropping a membrane onto a resonator chip without applied pressure to see which colour interference pattern would arise. Using our previous experience, we then gauged the flip-chip gap: if it was sufficiently small, we applied the glue and cured it at room temperature; if the gap was too large we lifted the membrane and either rotated it to see if a better configuration was possible at a different angle or we chose another resonator or membrane chip and attempted the assembly again. During curing, we inspected the interference pattern of this dropping and inspection technique of the membrane, and saw it changed much less than when applying pressure. Since we also knew which interference patterns corresponded to small gaps, we were able to repeatedly achieved large electro-mechanical couplings with $g_0/2\pi > 1\,\mathrm{Hz}$.

3.6 Fabrication Failures and Modifications in the Process Flow

In this final fabrication section we report on fabrication attempts which have not yielded any success or modifications made over time to the above processes which resolved problems which we encountered.

Deposition of superconducting MgB_2

At the beginning of the project, we attempted to deposit Magnesium Diboride (MgB_2) as a superconductor, since its high transition temperature around 38 K would allow for superconducting chips at liquid helium temperature near 4 K. A number of papers had reported thin film deposition of this material[Xi09] and superconducting resonators[Že+14].

We thus attempted to deposit the material by co-sputtering with two separate targets of Mg and B, which is typically followed by an annealing step. Unfortunately the tool frequently went out of use without us being able to measure superconductivity in the thin film. We eventually abandoned this route after a few months: no-one in the DTU cleanroom had ever used MgB_2. Also Mg is generally considered a dirty material in vacuum systems: given its low vapour pressure, it easily cross-contaminates other

users' wafers and this would have severely limited the tools which we would be able to use in the cleanroom.

Deposition of superconducting Nb

Pure Niobium (Nb) is also already superconducting at liquid He temperature, thus we attempted its deposition in the cleanroom's Lesker sputter tool. High-quality superconducting Nb deposition may require elevated substrate temperature and certainly needs an ultra-high vacuum tool ($<10^{-9}$ mTorr base pressure before processing) since Nb very easily forms an oxide. We attempted to reduce the base pressure by gettering with e.g. titanium: that is, we sputter Ti into the process chamber which captures any residual gases. If the cryopump of the Lesker has recently been regenerated, we coat the process chamber with Ti (which can be done be having a shutter in front of the processed wafer) and can reduce the base pressure from its usual 1×10^{-7} mTorr to 1×10^{-8} mTorr. This pressure reduction can be sustained over hours and even allows for processing and loading of multiple wafers via the tool's load-lock.

This reduction in base pressure by gettering was however not enough for pure Nb. We also attempted baking of the process chamber by loading the wafer, keeping the chamber at elevated temperature (up to 600 °C) for several hours or overnight, and depositing the material once the chamber had cooled down to room temperature. This also allows to reduce the base pressure to low 10^{-8} mTorr, but not sufficient once again to reach ultra-high vacuum (UHV). Ultimately, the vacuum flanges of the Lesker tool are not adapted for UHV operation and deposition of superconducting Nb.

Etching NbTiN from Cl_2 to SF_6

For a long time we used an ICP etch recipe using a pure Cl_2 gas at high-power (1900 W on the coil). Despite the short 40–60 s etch, this lead to burning of the 1.5 µm thick UV photoresist which ultimately makes a flip-chip assembly with small distance impossible, since the membrane contacts the grains of photoresist remaining after processing (see Fig. 3.12(c)).

A first step was to split up the etch from one long one into several 20 s long ones, but keeping the same coil power and chemistry. This improved cleanliness, by only leaving small resist residues as opposed to larges ones as before, but still making flip-chip assembly impossible. Any amount of sonication in a solvent resist strip bath was not able to remove these last residues.

We finally changed to a low power 250 W SF_6/O_2 etch, where we also ran several short 30 s etches resulting in very clean surfaces.

Chapter 4

Device Characterisations

In this chapter, we discuss the hardware of the microwave experiment. We use cryogenic vacuum chambers to isolate the samples for the environment and bring the materials into their superconducting state. Then we extract the experimental parameters by measuring the devices with low-noise microwave signals and detection.

4.1 Microwave Hardware and Cryogenic Setup

The cryogenic equipment used in this thesis is a Janis vacuum cryostat (a customised version of the ST-200 model giving us a larger sample volume) used for initial characterisation of the devices at approx. 4 K and a dry dilution refrigerator (DR) from Bluefors (model LD-250) for measurements at millikelvin temperatures. The microwave hardware are high-end Rohde& Schwarz tools.

Microwave Equipment

The main equipment used for microwave characterisation and measurement are a Rohde & Schwarz Vector Network Analyser (VNA, model ZNB20, with a calibration kit up to 15GHz), a R&S spectrum analyser (SA, model FSW, up to 26GHz) and a R&S signal generator (SG, model SMA100B, up to 12.75 GHz, with ultra low noise option SMAB-B711).

Most other equipment such as (cryogenic) circulators/isolators, or cryogenic amplifiers have a working range ∼3.5 GHz to ∼8.5 GHz, thus this is the frequency range which we target in our device fabrication.

Measurement sequences can be scripted in Python where we use Python modules and classes which we either wrote ourselves based on the VISA interface of the equipment or have taken from a R&S Github repository[Lal20].

A diagram of the cable connections for the microwave setup is shown in Fig. 4.1. The main MW pump tone comes from the SG and is sent to the Janis or DR input. After interaction in the device, the output is sent to the SA. For cavity reflection measurements and electro-mechanically induced reflection (EMIR) traces, a small probe tone from VNA port 1 is in-coupled at $-20\,\mathrm{dB}$ to the input line, and out-coupled at $-20\,\mathrm{dB}$ from the output line to VNA port 2. The most sensitive measurements of mechanical motion (both thermal and cooled close to its quantum ground state) are done with the SA, making use of its large dynamical range. Therefore we send the largest fraction of the signal to the SA and only in- and out-couple approx. 1% at the VNA. Amplitude and phase modulations of the pump tone are controlled by an arbitrary waveform generator (AWG) to port ext1 of the SG.

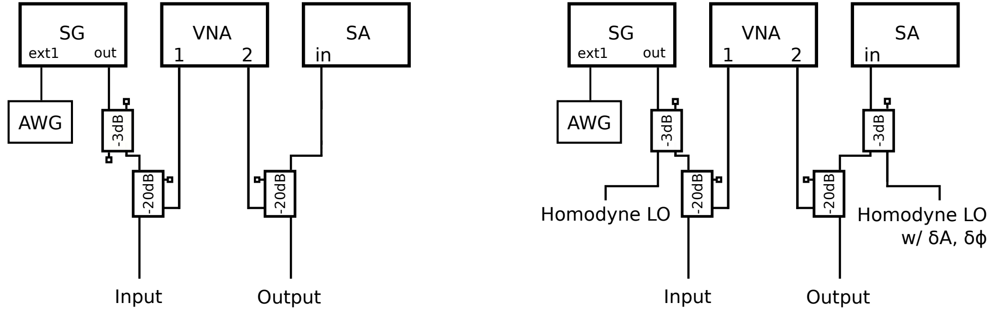

(a) Wiring of the MW equipment for cavity scan and direct detection readout of the electro-mechanical system.

(b) Wiring for cavity scan and homodyne detection.

Figure 4.1: Schematic of the microwave setup in the dilution refrigerator used for millikelvin and quantum operation of our devices. For homodyne detection used for the Gorodetsky calibration (Subsec. 4.4), we can adjust amplitude δA and phase $\delta\phi$ of the local oscillator.

Flow Cryostat

The Janis cryostat is operated with a Pfeiffer HiCube roughing and turbo pump which allows to pump the vacuum can to approx. $1 \times 10^{-6}\,\mathrm{mbar}$ and is then cooled to $4\,\mathrm{K}$ by transferring liquid helium from a dewar to

the cryostat cold finger (where the device is mounted) with a transfer line. A radiation shield is fitted around the cold finger to shield it from room temperature thermal radiation heating. A schematic of the Janis setup is shown in Fig. 4.2.

The cold finger currently has enough space for one device assembly (superconducting flipchip mounted inside of a 3D box) to be mounted. Typically the mounting of the sample takes 30-60 minutes, the pump-down 1-2 hours, the cooldown 90-120 minutes and the characterisation lasts a few hours, such that we can let the cryostat heat up over night: allowing us to characterise 1 device per day. A sample mount which can host four assemblies on the cold finger of the Janis or in the DR has been designed and machined by the workshop, but, we have not tested it yet.

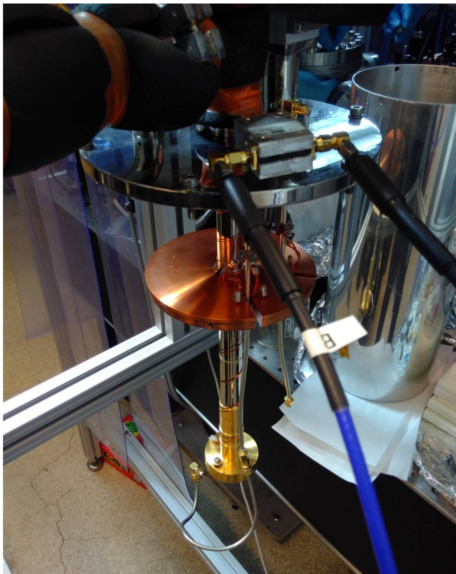

(a) Picture of the open Janis 4 K flow cryostat with MW coaxial lines, and radiation shield in the back.

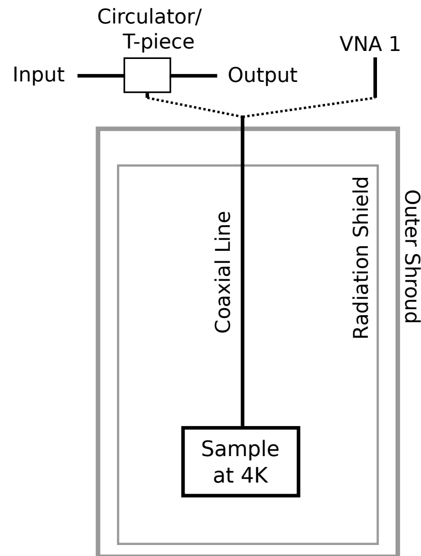

(b) Sketch of the MW lines setup in the Janis cryostat.

Figure 4.2: The Janis flow cryostat is used to perform initial characterisations of the devices at 4 K.

Two microwave semi-rigid lines run from the outer vacuum can, thermalised at the radiation shield, down to the cold finger and connect to the 3D box for microwave readout of the cavity. We measure the single-port microwave cavity in reflection, where we place a circulator at the outside of the cryostat to avoid standing waves in any S-parameter measurement.

This setup also lends itself to pump-probe measurements such as EMIR or to measure the mechanical thermal sideband of a pump field.

Since the MW cavity resonance frequency depends on fabrication, we sometimes must measure resonances beyond the working range of the circulator (for resonances beyond ~9 GHz). We can then either simply measure the direct reflection (without circulator), but cannot perform pump-probe characterisation; or we replace the circulator with an SMA T-piece which effectively results in a side-coupled cavity (notch-type resonator).

Typical characterisation in the Janis cryostat comprises of:

- a scan of the microwave resonance to extract the resonance frequency ω_c, the external coupling rate κ_e and the internal loss rate κ_i,
- a scan of the mechanical sideband frequency (in an EMIR trace or in a power spectrum) to determine the mechanical mode frequency Ω_m where we also identify the location of the phononic bandgap (approximate locations in frequency are known from simulation); and ringdowns of the mechanical mode to obtain the mechanical energy decay rate Γ_m,
- the measurement of dynamical backaction effects (microwave induced spring effect and damping) to determine the electromechanical (multi-photon) coupling strength g, and from calibration of the intra-cavity photon number n_{cav} (by explicitly measuring the cable losses in a transmission S-parameter measurement) we extract the single-photon coupling g_0.

Promising devices are then placed into the dilution refrigerator for measurement at millikelvin temperatures.

Dilution Refrigerator

In the dilution refrigerator (DR) samples can be cooled down to a temperature of about 10 mK: the exact temperature can depend on how much we load up the mixing chamber plate.

A schematic of the microwave setup in the DR is given in Fig. 4.3. More details about the setup inside of a DR and the MW components used can be found for example in Ref. [Ber19].

These extremely low temperatures allow us to explore new regimes of ultra-low material loss for our mechanical oscillators, to make use of more conventional superconducting materials (such as Al) for low electrical energy loss in our circuits, and to reduce the thermal occupations of the mechanical and microwave baths for quantum operation of our experiments.

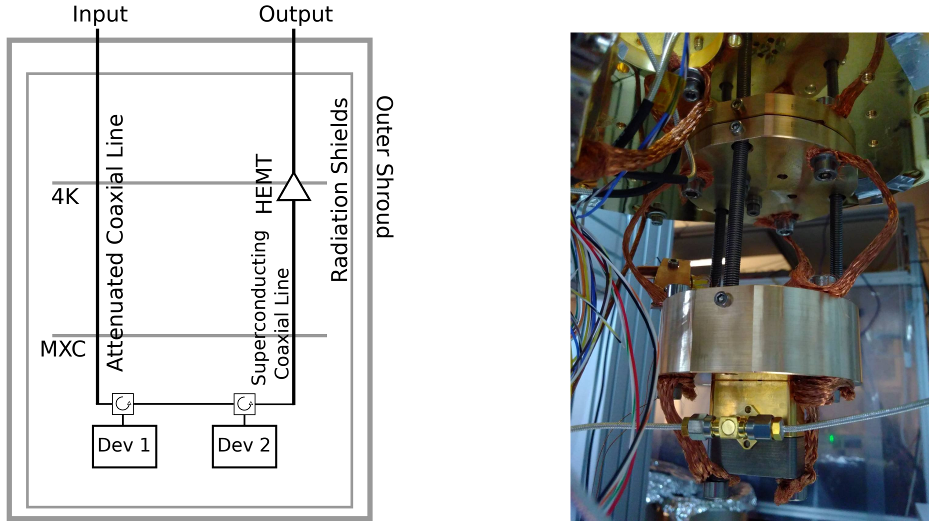

(a) Sketch of the MW lines setup in the DR, with circulators at the device entrances.

(b) A mass-on-a-spring sample holder isolates the electro-mechanical system from environmental vibrations.

Figure 4.3: Schematic of the microwave setup in the dilution refrigerator used for millikelvin and quantum operation of our devices.

Our DR is a so-called "dry" model where the cooling of the system down to 4 K is done with a pulse tube (PT), instead of "wet" models which are cooled with liquid He. The final cooling to millikelvin is done by a ^{3}He-^{4}He mixture at the mixing chamber (MXC): when pumping from one side on the mixture, the ^{3}He is preferentially evaporated, leading to depletion in the mixture and new ^{3}He can be diluted into the mixture from the other side. This dilution being an endothermic process leads to the cooling of the environment.

Our DR has a large MXC plate where we can mount numerous assemblies and connect them in series such that they can all be measured in a single cooldown. Each cavity and device assembly is equipped with its own circulator or SMA T-piece such that we mount them in series one after the other on the same coaxial line. In this way we only require one amplified line after the samples and only one attenuated line for MW input. The individual devices are then addressed in a frequency-multiplexed fashion where we know each device's MW resonance frequency from the initial characterisation in the Janis cryostat. For this to work properly, we must

in particular be careful that one device's resonance does not fall on top of a spurious resonance of another assembly.

When working with mechanical objects near their quantum ground state, environmental sources of vibration become an important heating mechanism and need to be avoided. One such heating source is the PT which can heat mechanical modes up to several Kelvin despite the thermodynamic temperature of the environment and materials being at a few millikelvin. Newer versions of Bluefors DRs such as the one used in this thesis are thus equipped with a ^{4}He battery on the 4K plate: we can fill it up with gaseous He which condenses into liquid while the pulse tube is on. Then this liquid He can be pumped upon to keep the system cold, while the pulse tube is turned off. The filling of the battery takes approximately 8 hours and gives us about 2.5 hours of DR operation without PT vibration.

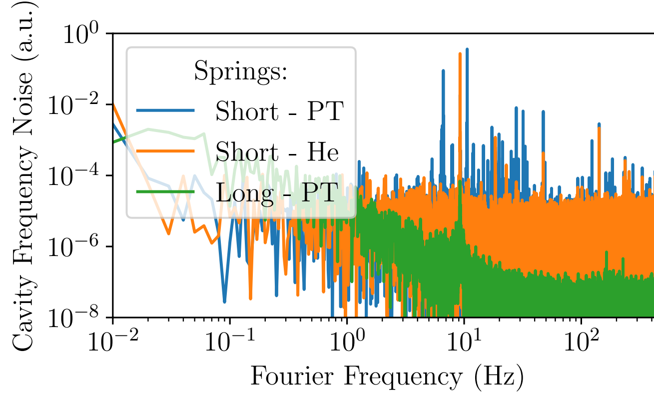

Figure 4.4: We measure the noise in the cavity resonance frequency $S_{\omega_r\omega_r}$ of flipchipv27. With short springs, operation on He battery is significantly quieter that on PT. With the longer springs, almost all noise peaks are suppressed.

To prevent excess vibrational noise, we place our devices on a mass-on-a-spring mechanical damper (Fig. 4.3(b)). The development of the damper by Thibault Capelle being recent means that only flipchipv24 and flipchipv27 data presented here was taken on the damper, all other devices were fixed directly onto the MXC plate. As an example of vibrational noise, we plot the cavity frequency noise $S_{\omega_r\omega_r}$ computed from the phase of the tone reflected by the cavity[Bar+08]. We compare the cases when the damper is assembled with short and long springs (keeping the same mass), operated on PT and on He battery. When the damper is set up with short springs, we are able to see noise peaks at multiples of 1.2 Hz, which is the PT frequency. Many of

these peaks disappear on He battery operation, however longer springs are necessary to suppress the remaining peaks. The longer springs set-up allows for a cleaner cavity spectrum and reduces the mechanical bath occupation even on PT (see also Sec. 4.5 comments for the 20 nm device).

4.2 Microwave Reflection Measurements

The first step of the device characterisation is finding and measuring the MW resonance. The transmission spectrum through the Janis cryostat or DR can look complicated especially if there are spurious resonances (such as the resonance of the NbTi in-coupling antenna or of the 3D volume hosting the chip) or if several devices are placed in series along a single transmission line. At this stage we must identify which dips in the spectrum are those of our MW cavities. The most outstanding difference is their behaviour with temperature when we reach close to the superconducting transition temperatures of the materials involved.

For our choice of material, NbTiN has a superconducting transition temperature T_c around 13-17K for high-quality films. As the cryostat reaches these temperatures, a reflection dip starts appearing and shifting up in frequency as the device cools and thermalises to the cold finger. We may differentiate the device resonance from other spurious resonances as the device is the only one to experience a significant frequency shift when its temperature reaches the base temperature of the cryostat. This is because the device is the only element with a material exhibiting significant *kinetic inductance* (KI) in its superconducting state[NBB19; Xu+19]. In a circuit made out of a KI material, electrons react with a delay to alternating fields because of the inertia due to their kinetic energy. This delay is equivalent to an increased circuit inductance (in addition to the geometric inductance): thus an increase in kinetic inductance will lead to a reduction of the circuit's resonance frequency. In its superconducting state, the kinetic part of the inductance of a thin film increases as we approach (from below) the critical current or critical temperature of the superconducting material: therefore we expect a reduction of the KI as the film thermalises below its T_c, leading to an upwards shift of the device's resonance frequency. NbTiN and other superconducting nitrides like TiN or NbN, being in the 'dirty superconductor' limit, are well known for having large KI fractions as opposed to clean superconductors like Al.

In the Janis cryostat, the presence of significant kinetic inductance makes temperature stability and in particular fast thermalisation particularly important for frequency stability of the cavity. Materials with high

heat conductivities are crucial at these low temperature: as an example, using standard copper pieces without gold plating as sample mounts in the cryogenic setup gives a thermalisation time upwards of several hours, whereas gold-plated oxygen-free high-conductivity copper (OFHC copper) reduces thermalisation time (and thus frequency drift) to around 30 min (time after the cold finger, where the thermometer resides, reached its base temperature).

Proper design of the sample holder is also crucial to not have any spurious MW resonances. For our loop-gap resonators, we require a small 3D volume to hold our chip assembly such that any 3D vacuum mode is pushed to frequencies beyond 15 GHz.

LGR characterisation at 4K and millikelvin

We fit the reflection data to the model given in Eq. 2.6 and extract the cavity parameters.

We plot the real and imaginary parts of the reflection coefficient S_{11} against frequency and in the complex plane in Fig. 4.5. In the complex plane a resonance is a circle, where the size of the circle gives the coupling or interaction efficiency, and the location in the complex plane (its position and rotation) gives environment factors (such as cable loss, delay or cable reflections). Device flipchipv27 is measured in the Janis flow cryostat at 4 K and plotted in Fig. 4.5(a), we extract

- Resonance frequency $f_c = 8.363\text{GHz}$,
- Internal loss $\kappa_i/2\pi = 1.99\text{MHz}$, $Q_i = 4.2 \times 10^3$,
- External coupling $\kappa_e/2\pi = 160\text{kHz}$, $Q_e = 5.2 \times 10^4$,
- Loaded total loss $\kappa/2\pi = 2.15\text{MHz}$, $Q_l = 3.9 \times 10^3$.

This same assembly measured in the DR at 35 mK, plotted in Fig. 4.5(b), gives a much higher internal quality factor, now that the entire MW resonator is deeply in its superconducting state. We extract

- Resonance frequency $f_c = 8.350\text{GHz}$,
- Internal loss $\kappa_i/2\pi = 43\text{kHz}$, $Q_i = 1.92 \times 10^5$,
- External coupling $\kappa_e/2\pi = 183\text{kHz}$, $Q_e = 4.6 \times 10^4$,
- Loaded total loss $\kappa/2\pi = 226\text{kHz}$, $Q_l = 3.7 \times 10^4$.

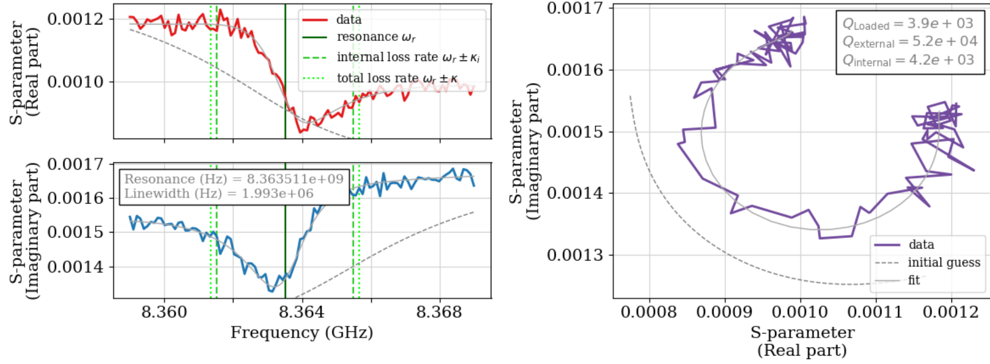

(a) Cavity parameter characterisation for flipchipv27 at 4 K, where the large internal loss ∼2 MHz is attributed to the Al metallisation on the membrane which is not superconducting and the NbTiN which is still lossy at this temperature. We fit the data with Eq. 2.6.

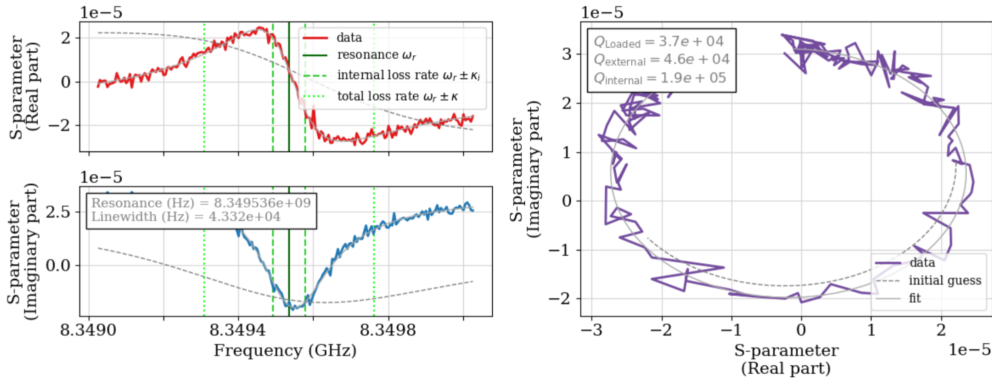

(b) Cavity parameter characterisation for flipchipv27 in the DR at base temperature of 35 mK shows an internal linewidth of 43 kHz.

Figure 4.5: The fit of the cavity reflection data to our model allows us to extract parameters intrinsic to the cavity as well as the effect of the environment.

For these microwave cavity characterisations, we must acknowledge the slight caveat that there can be systematic errors in the extraction of the ratio κ_i/κ_e in the current setup which we cannot correct for[1]. In the microwave setup, reflections at component interfaces can lead to partial reflections of waves in the coaxial cables. This reflections result in the measurement of asymmetric cavity resonances from which an overestimated coupling efficiency η_c is extracted. While we did not have time to implement a calibration correcting for this asymmetry before submission of this thesis, we do now have the 6-way cryogenic switch necessary for this calibration as proposed in Ref. [Wan+21]. Fortunately an over-estimate of η_c does not qualitatively change the results in the rest of this thesis: in particular for the claim of ground state cooling in Chap. 5, it would only overestimate the real final occupation.

We may here use the simulations performed in Sec. 2.2 to estimate the membrane gap to the LGR electrodes and the participation ratio. We can deduce the ratio of capacitances and the participation ratio from the ratio of resonance frequencies of the measured device f_c and simulated membrane-free LGR $f_{\text{no-mem}}$ from Fig. 2.5(d):

$$\left(\frac{f_c}{f_{\text{no-mem}}}\right)^2 = \frac{C_p}{C_p + C_m} = 1 - \eta_{C-C}, \qquad \eta_{C-C} = 25\%, \tag{4.1}$$

giving a gap $d \approx 450\,\text{nm}$.

Another assembly (flipchipv26) has given an even higher participation ratio: with resonance frequency of 6.719 GHz, we calculate $\eta_{C-C} = 53\%$. However this device collapsed during early cryogenic operation and we did not gather much data on it. It nonetheless confirms that our fabrication technique allows us to fabricate devices with low resonant frequency, implying the flip-chip distances are very small.

4.3 Mechanical Characterisation

The metallised phononic membranes are measured in cryogenic conditions to assess their mechanical qualities. The mechanical mode we mainly report on is the mode in the first bandgap of flipchipv27 at 1.485 MHz, this is the mode for which the "lotus" design was developed: Fig. 4.6 show a clean bandgap from 1.36 MHz to approx. 1.70 MHz, with the mode of interest in its middle.

[1] We are grateful to Prof. Gary Steele for pointing this out in private communications.

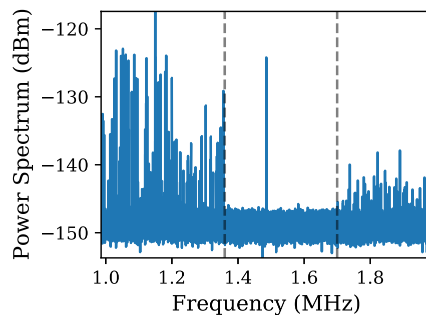

Figure 4.6: The bandgap around the 1.485 MHz mode is clearly visible in the power spectrum of the upper sideband of a MW pump placed on cavity resonance.

Mechanical Ringdown Measurements

Given the generally ultra-high quality factors of our membranes, the easiest measurement of mechanical decay rate is by ringdowns of the mechanical energy. Spectral measurements of the mechanical linewidth are also set-up as a means of measuring additional mechanical frequency noise.

To perform ringdown measurements, we must first supply the mechanics with energy in a reproducible manner, which will then leak out to give an exponentially decaying mechanical energy in time. We fit the energy ringdown with the formula:

$$E_0 \exp\left(-\Gamma_m t\right) \tag{4.2}$$

with the initial energy E_0 and the energy decay rate Γ_m.

The excitation sequence taken from Ref. [Cap20] is composed of three steps:

- the pump is red detuned from the cavity to $\omega_c - \Omega_m$ and phase-modulated at the mechanical frequency Ω_m to prepare the mechanics into a well defined coherent state,
- the pump is blue-detuned to $\omega_c + \Omega_m$ to amplify the mechanical state to a coherent state with occupation many orders of magnitude larger than thermal,
- the pump is again placed on the red cavity side to $\omega_c - \Omega_m$ at varying powers to measure the decaying mechanical sideband.

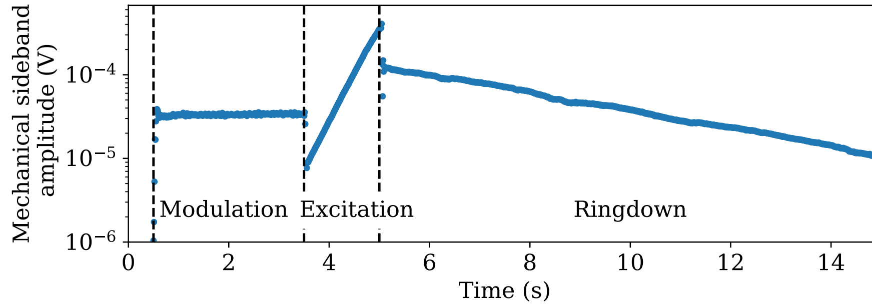

Figure 4.7: Ringdown sequence measured with coherent displacement, amplification and ringdown (here with DBA broadening). Without DBA the change in mechanical amplitude would be imperceptible over 10s: generally we measure ringdowns over period of at least 300s to see a significant decrease!

During the entire sequence, the SA measures an IQ trace on cavity resonance: since the pump is always detuned from the cavity by $\pm\Omega_m$, one of the two mechanical sidebands will always be on resonance to be recorded. The exponentially decaying mechanical sideband energy is then fit to extract the decay time constant and thus the mechanical broadening at the given pump power and environment temperature.

A measured trace is plotted in Fig. 4.7 where the three steps of the sequence are clearly visible: with 3 s of phase modulation to displace the mechanics, the pump is on the blue side for 1.5 s, and the mechanics is left to ringdown for 300 s.

Mechanical quality at millikelvin temperatures

In the DR, we measure ringdowns series where we vary the power of the red pump during the ringdown. Traces of these ringdowns are plotted in Fig. 4.8(a). From the fit of ringdowns, we can extract the intrinsic mechanical decay rate Γ_m as the decay rate in the low power limit (see Fig. 4.8(b)), and the high power limit gives us information about the electro-mechanical interaction: where the induced broadening goes linearly with intra-cavity power (see Eq. 2.21).

We then perform such ringdown series at several temperatures between the sample base temperature at 30 mK and 1500 mK to investigate the mechanical damping of the material. In Fig. 4.9 we plot the intrinsic mechanical damping rate and quality factor as we increase the temperature

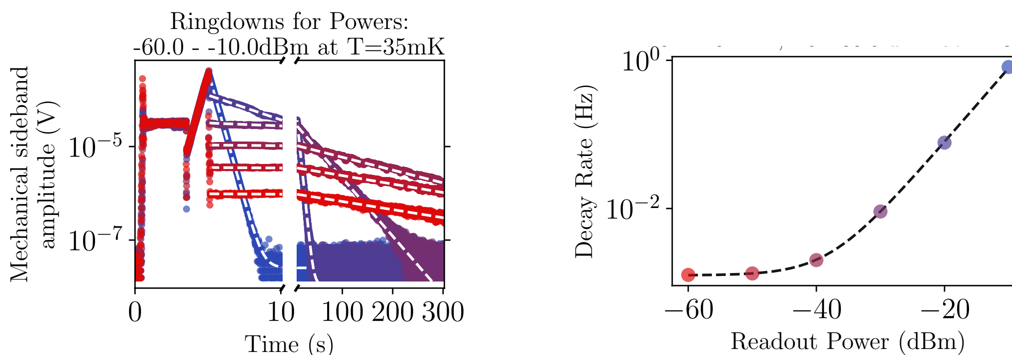

(a) Overlapped time traces of the ringdowns for varying powers. Identical initialisation of the mechanics through coherent displacement and amplification is clearly observed. Red to black traces indicate increasing power during ringdown.

(b) Plot of the inverse ringdown time constants as a function of power. We fit the ringdown decays to extract the mechanics' intrinsic $\Gamma_m/2\pi = 1.25\,\mathrm{mHz}$ and the corner power $P_0 = -38.0\mathrm{dBm}$, where the electro-mechanically induced linewidth broadening is also Γ_m.

Figure 4.8: At a fixed temperature of 35 mK, we perform multiple ringdowns with the same coherent displacement and amplification steps, as an initialisation, and ramp up the power in the red pump during ringdown to induce a broadening of the mechanical linewidth. Data point colours agree between the two plots.

of the MXC plate. Firstly we do not see any convergence of the damping rate at low temperatures, suggesting that the sample remains thermalised with the MXC plate all the way down to the base temperature. For early cryogenic measurements, we indeed observed a plateau in Q-factors starting around ∼100 mK, suggesting thermal decoupling of the sample from the MXC plate. Thermal coupling was improved by tightening the screws on the assembly and by changing the sample holder box material from Nb to OFHC copper.

Furthermore ringdown series were performed while the PT was on and while using the He battery: these two temperature series show no difference. We can thus perform an initial part of our characterisation with the PT on, while measurements involving the mechanical thermal occupation must be done on the He battery or at least with the mechanical damper.

The power law dependence of the intrinsic mechanical damping with temperature suggests our devices are limited by coupling to a mechanical two-level systems (TLS) bath[Zho+19]. We also note a qualitatively different behaviour from the square, unpatterned Si_3N_4 membranes presented in Ref. [YCS15], where the Q-factor levels off above 200 mK. This qualita-

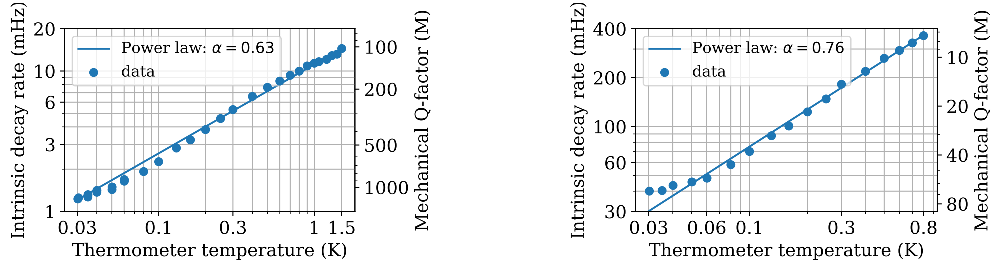

(a) Intrinsic loss for the first bandgap mode at 1.485 MHz.

(b) Intrinsic loss for the second bandgap mode at 2.671 MHz.

Figure 4.9: We change the temperature of sample holder of flipchipv27 and extract the intrinsic linewidth of the main mechanical mode (first bandgap at 1.485 MHz) and a high-Q mode in the second bandgap (2.671 MHz). The mechanical damping follows a power law with temperature, suggesting being limited by TLS damping.

tive difference could hint at the impact of clamping and phonon tunnelling losses at very low temperatures[Wil+09; WR08; Col+11].

We finally point out that the mechanical quality factor for flipchipv27 which we report in Chap. 5 and in the publication in App D is higher than the one in Fig. 4.8: namely $1.5 \cdot 10^9$ against $1.2 \cdot 10^9$. The data sets were taken during the same cooldown cycle but at different times: after 1 month at millikelvin temperatures for Fig. 4.8 and after 3 months for the publication. As the device remained in the cryogenic environment, the mechanical quality increased even though measurements were performed at the same temperature: thus it is not simply due to improved thermalisation to the cold environment.

Mechanical Spectrum and Frequency Stability at millikelvin temperatures

At the DR's base temperature, the electro-mechanical system is remarkably stable in time and allows us to measure long time traces (many hours) of the cavity reflected microwave signal. To show that we can measure the mechanical frequency stability of a sample, we recorded 40 traces each 1000 s long for the earlier sample flipchipv20 demodulated around the mechanical sideband frequency from which we extract the I and Q quadratures, take the Fourier transform and plot the spectrum (Fig. 4.10(a)). A Lorentzian fit to the mechanical peak (fit on the log-scale making use of the large signal-to-noise ratio) gives a linewidth which we compare to the ringdown-extracted

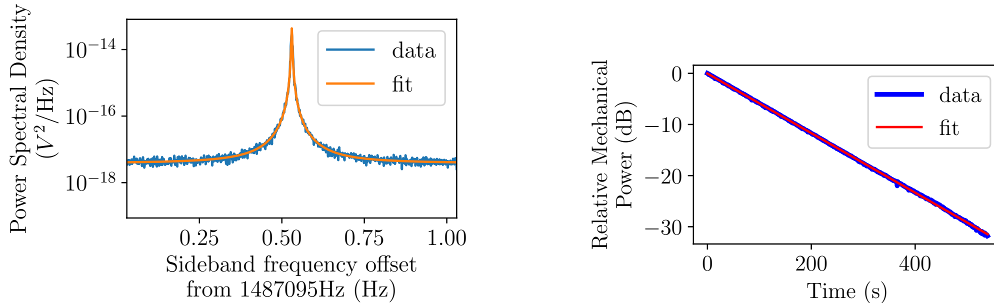

(a) Spectrum at the mechanical sideband, with 1 mHz measurement bandwidth. A Lorentzian fit gives a linewidth of (2.60 ± 0.15) mHz or a Q of (570 ± 33) M.

(b) We measure the mechanical ringdown under the same conditions to compare with the spectrum: we extract a decay rate of (2.13 ± 0.02) mHz, a Q of (696 ± 5)M.

Figure 4.10: Mechanical frequency spectrum on flipchipv20 measured at the DR base temperature (30 mK) while cooled by PT. We compare the mechanical linewidths extracted from the frequency spectrum and from the energy ringdown.

decay rate: (2.60 ± 0.15) mHz and (2.13 ± 0.02) mHz respectively, suggesting that any additional dephasing is small (at most 22% of the total spectral linewidth). Such a measurement could also be performed on other samples, as part of a more complete device characterisation.

4.4 Electro-Mechanical Interaction Calibration

The calibration of the single-photon coupling is quite easily performed in the Janis cryostat by knowing the intra-cavity photon number. We can directly measure cable losses at room temperature, without these losses changing too much at cryogenic operation. The much higher complexity of the MW wiring in the DF makes the measurement of cable losses at millikelvin temperatures more difficult. Thus we must use the so-called Gorodetsky method instead.

Calibration of the Single-Photon Coupling Using the Gorodetsky Method

To establish the interaction strength of individual quanta of light and motion, we implement the g_0 calibration technique presented in Ref. [Gor+10]. This method assumes the mechanical state to be a thermal one (condition which we need to verify) and measures the phase modulation imparted by the mechanically-modulated cavity onto a fixed frequency pump tone, this modulation is then referenced to a known phase modulation to extract the interaction strength.

We perform this calibration in an unbalanced homodyne setup, where for microwave signals we do not need to worry about additional amplitude modulation caused by elements in the circuit (as opposed to the optical case). The tone from the SMP is internally phase-modulated with a frequency given by an AWG and a modulation depth ϕ_0, and split on a 50/50 splitter (see Fig. 4.1(b)) where one side is sent to the cavity and the other becomes the local oscillator (LO). The total attenuation and amplification on the sample arm (going through the DR) of this microwave interferometer is much less than unity such that the LO is large compared to the signal to be measured. We make use of a phase shifter on the LO to optimise the homodyne signal, and an LO variable attenuator to not saturate the IQ measurement. The phase modulation depth is calibrated by a fit to the

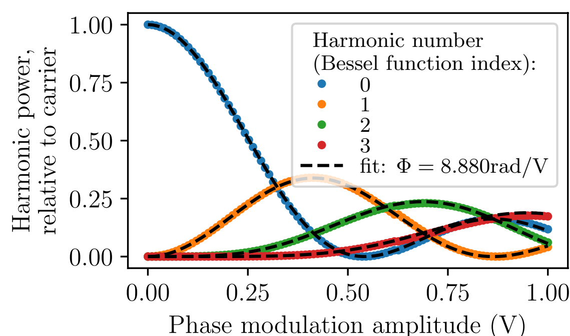

Figure 4.11: The MW carrier from the SG is phase modulated with a voltage from the AWG. We calibrate the phase modulation by applying a 1 MHz modulation with voltage amplitude from 0 V to 1 V and measuring the power in the sideband harmonics at multiples of the modulation frequency (the zeroth harmonic is the carrier). This calibrates the phase modulation sensitivity Φ in radians/V.

measured Bessel functions expansion, as shown in Fig. 4.11. We then use a small ϕ_0 for the calibration measurement.

We demodulate the homodyne signal around the carrier frequency with a bandwidth of 4 MHz into its I and Q components. Then we take the modulus squared of the temporal IQ trace to numerically simulate an intensity measurement (as a photodiode would), perform the Fourier transform, and take the modulus squared of the FFT to obtain the power spectral density. The areas A_{mod} and A_{mech} under the calibration peak at Ω_{mod} and mechanical peak at Ω_{mech} in the power spectrum respectively are compared to yield a g_0 calibration following:

$$g_0^2 = \frac{1}{2\langle n_m \rangle} \frac{\phi_0^2 \Omega_{mod}^2}{2} \frac{A_{\mathrm{mech}}}{A_{\mathrm{mod}}}. \tag{4.3}$$

The carrier tone is placed on cavity resonance ($\Delta \approx 0$, slightly red detuned) with the calibration sideband 2 kHz below the mechanical peak ($\Omega_{mod} - \Omega_{mech} = -2\pi \cdot 2\,\mathrm{kHz}$). For a good signal to noise ratio, we must increase the carrier power into a regime where DBA is non-zero. We take this mechanical cooling into account by measuring two ringdown sequences, one at the calibration power and one at a low, DBA-free power: the ratio of energy decay rates between these two gives the mechanical cooling factor, which we multiply to the measured mechanical area A'_{mech} in the PSD to obtain the DBA-free area A_{mech}.

We plot the ratio of mechanical (DBA-free) to calibration peaks areas against temperature in Fig. 4.12, measured on PT. To use Eq. 4.3, we require the mechanical state to be thermalised: this condition is verified at

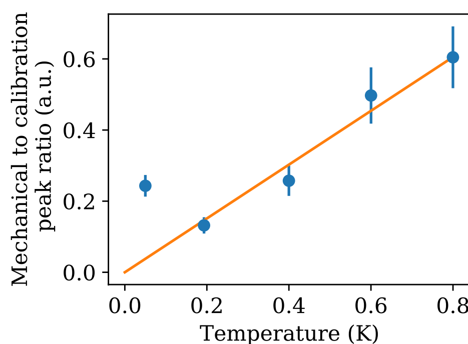

Figure 4.12: At high temperatures, the ratio of mechanical to calibration peak area is proportional to temperature: from this thermalisation condition, we extract $g_0 = 2\pi \cdot (0.87 \pm 0.11)\,\mathrm{Hz}$.

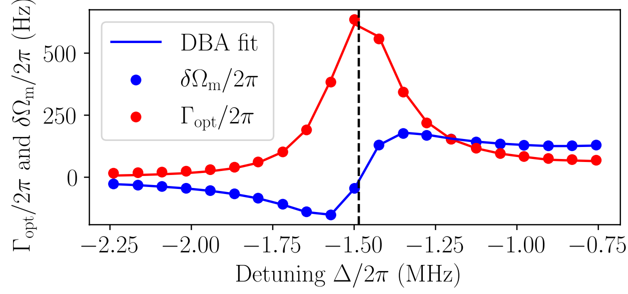

Figure 4.13: A detuning series of EMIR measurements gives the multi-photon coupling g and corresponding intra-cavity photon number n_c via fits of the light-induced mechanical frequency shift $\delta\Omega_m$ and damping Γ_{opt}. The vertical dashed line indicates a negative detuning by the mechanical frequency. Note that the fit curves are not smooth when varying Δ because cavity parameters change at each data point.

high temperatures (above 400 mK) where the area ratio is proportional to the thermometer temperature. We extract $g_0 = 2\pi \cdot (0.87 \pm 0.11)$ Hz. At low temperatures, the mechanical mode is not in equilibrium with its thermal environment but is additionally excited by the PT vibrations. At the time when the data for flipchipv27 was being taken, we were still in the early stages of testing the damper. While testing a damper with shorter springs, we measured such good MW and mechanical performance on flipchipv27 that we decided to stay cold to take the data presented here. This spontaneous decision however meant that we did not have the best damper setup for these measurements. With the longer springs the noise of the MW cavity was as small on PT as on He battery (see Fig. 4.4). A damper with longer springs had also been tested for flipchipv24, which lead to lower vibrational noise (see Sec. 4.5).

Calibration of the multi-photon coupling, wiring loss and amplification

To calibrate the multi-photon coupling g, we make use of the DBA equations Eqs. 2.21 and the cavity-detuning dependent intra-cavity photon number via Eq. 2.3. Taking both these effects into account, we fit the mechanical frequency and damping rate via an EMIR measurement (see Fig.4.13). During these measurements we also monitor the cavity reflection (to account for any pump-induced modifications of the cavity shape). Given the above

g_0 calibration, the only free parameter is the cable attenuation from SMP to cavity which we extract from this measurement. Data in Fig.4.13 give an MW power attenuation of -66.5 ± 1dB. In this thesis we always refer to the power as exiting the SG, the power at the cavity entrance can be computed by adding the above attenuation to any plotted MW power.

4.5 Supplementary Devices

We have so far mainly presented our main device flipchipv27. For completeness, we briefly report (in addition to flipchipv20 above) on other devices fabricated and measured during this project to showcase the possibilities of our electro-mechanics know-how. We present here a dielectrically-coupled device (flipchipv2), a double-defect membrane device (flipchipv6) and a 20 nm thin membrane device (flipchipv24).

Dielectrical Coupling

Pictures of a dielectrically coupled membrane are shown in Fig. 3.1. From a DBA detuning series measured in the Janis cryostat, we extract a single-photon coupling $g_0/2\pi \sim 6$ mHz. The dielectric coupling falling off exponentially with distance of the membrane from the IDC[Cap+20] meant that, if we wanted to reach higher g_0 values, we needed to switch to a vacuum-gap capacitor coupling scheme with a metallised membrane. Taking the IDC geometry in our design file, we estimate the flipchip distance to be $\sim$1.3 µm, showing we needed to improve our assembly technique to reach the nominal 300 nm flip-chip distance.

We also measure mechanical ringdowns, fitting a Q-factor of $\sim$ 40M in the Janis cryostat. Given that this coupling scheme does not involve the adding of any material of the membrane, it could be beneficial for investigating the mechanical properties of Si_3N_4 at millikelvin temperature without potential losses from a metallisation or heating from optical absorption[Fis+16].

Double Defect Membrane

An image of a double defect sample can be seen in Fig. 2.8(a). First characterisation was done in the optical interferometer[Bar+16] with the probe beam placed on the non-metallised defect. The two mechanical modes are clearly visible in Fig. 4.14(a), where the signal heights (differing by slightly less than 10dB) are in agreements with the simulated mode shapes

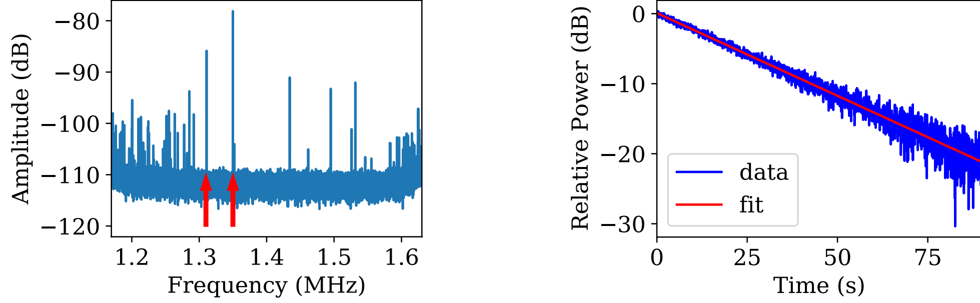

(a) Spectrum of the double defect membrane as measured in the optical interferometer at room temperature. Arrows point to E and O modes.

(b) Rindown measurement of mode E at 22 mK has a Q-factor of 150M for a frequency of 1.290 MHz.

Figure 4.14: The mechanical properties of a metallised double defect “dahlia” membrane.

in Fig. 2.8(b): at the optical defect, the lower frequency mode (mode E) has a lower displacement amplitude than the higher frequency mode (mode O). This membrane has 15 nm of Al deposited on a 70 nm thick SiN membrane where we see that the metallised “dahlia” design gives modes much closer to the lower bandgap edge than the “lotus” design (to be compared to the mode placing in Fig. 4.6).

At room temperature, the mechanical quality is low possibly limited by loss in the Al metallisation or by squeeze-film damping[Tsa+17] in the flipchip vacuum gap. After pumping for one week reaching a pressure of 3.7×10^{-8} mbar, Mode E has a Q_m of 510k at 1.311 MHz and mode O a Q_m of 3.67M at 1.350 MHz.

In the Janis at 4 K, the mechanical quality increased: $Q_m = 6.3$M for mode E and $Q_m = 9.1$M for mode O, while their frequencies fell to 1.290 MHz and 1.324 MHz respectively. In the DR with the MXC plate at 22 mK, the quality factor of mode E increased to 150M, with just a small change in frequency compared to the Janis measurement (less than 1 kHz). For an unknown reason the Q-factor for mode O dropped to 1.4M.

The relatively low mechanical Q-factors of early samples (lower than the expected several 100s of million at cryogenic temperatures) is attributed to unclean membranes: the initially low fabrication yield forced us to use membranes that for example had not come out perfectly clean of the Piranha bath. As an example flipchipv6 had visible residues on the membrane that were not removed in any cleaning step.

Thinnest Membrane of 20 nm

The thinnest metallised membrane assembled into flipchipv24 had a Si_3N_4 thickness of 20 nm with an Al pad of 20 nm. This electro-mechanics device was the first to exceed a Q-factor of 1B, reaching 1.14B at 30 mK at 1.408 MHz. The device coupling was unfortunately too small to continue experimentation. We were however able to confirm the operation of the mechanical damper: the measured mechanical peak area increased by only 35% on PT operation as compared to He battery operation at 24 mK. This was encouraging for devices such as flipchipv27 which could then be operated continuously on PT with very little excess mechanical heating.

Chapter 5

Ground State Cooling

In this chapter, we summarise the main result of this thesis which is the sideband cooling of an ultra-coherent mechanical mode to its quantum mechanical ground state. The experimental setup is the same as for the characterisation performed in Chap. 4: we use the wiring depicted in Fig. 4.1(b). The device 'flipchipv27' is mounted on the mechanical damper with short springs and passively cooled by the DR to 30 mK for this series. As mentioned in Sec. 4.3, after prolonged exposure to the cryogenic environment the mechanical quality factor has increased to $1.5 \cdot 10^9$, thus $\Gamma_\mathrm{m}/2\pi = 1.0\,\mathrm{mHz}$.

First we calibrate the mechanical occupation in number of quanta by ensuring thermal equilibrium of the mechanics to its environment. For this thermalisation verification, we monitor the area of the mechanical sideband (placed on cavity resonance, i.e. $\Delta = -\Omega_\mathrm{m}$) at cooperativity $\mathcal{C} \ll 1$ and compare it to the thermometer reading. We plot this relation in Fig. 5.1(a), and fit it with a linear relationship for temperature points above 200 mK (red points). We limit the fit to high temperatures in case the sample thermally decouples from the thermometer and cooling plate at low temperatures, however the data shows that the sample remains thermalised below 200 mK. While the sample is cooled below the transition temperatures of the superconductors in the device, we expect the cavity parameters to change with temperature. We fit the cavity parameters for each temperature point, plotted in Fig. 5.1(b), and use them to correct the data in Fig. 5.1(a).

The linear relationship between mechanical energy and thermometer reading confirms the thermalisation of the sample and allows us to use the Bose-Einstein relation to extract an initial occupation of $\bar{n}_\mathrm{th} \sim 1400$ at DR base temperature. This initial occupation corresponds to an effective mode temperature of about 80 mK, which is significantly above the sample temperature of 30 mK.

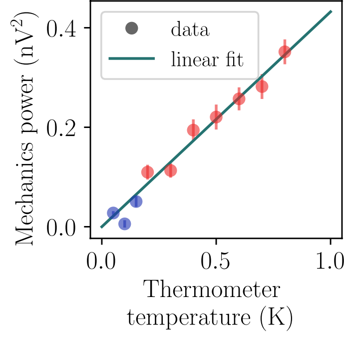

(a) Mechanical mode thermalisation at millikelvin.

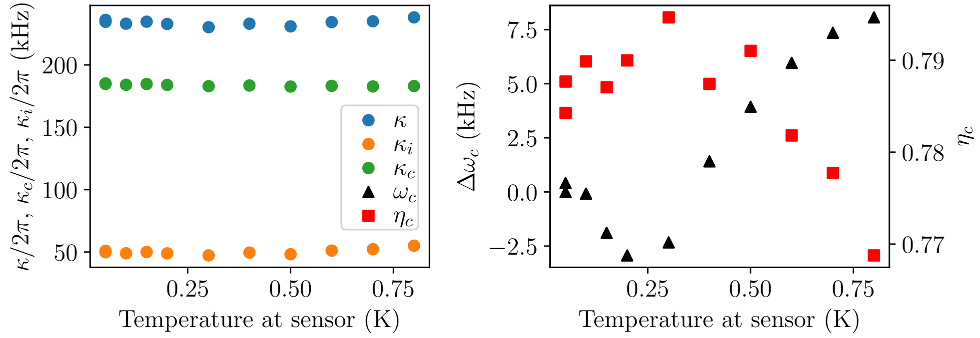

(b) Cavity parameters at millikelvin.

Figure 5.1: (a) The mechanical sideband area is measured as temperatures from 30 mK to 800 mK in the same configuration as for the cooling series in Fig. 5.2. The linear relationship confirms device thermalisation to the DR environment. (b) Cavity parameters fitted for each temperature point vary little, but are nonetheless used to correct data points in (a). Subfigure (a) reproduced from [Sei+21].

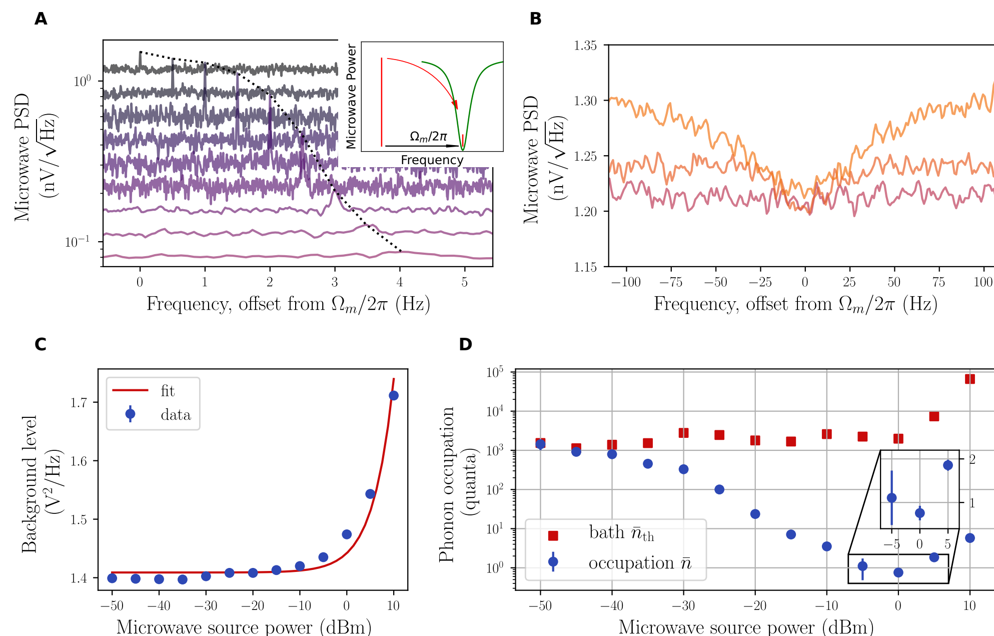

Figure 5.2: Sideband cooling power series. A) and B) Spectra of the upper mechanical sideband as the pump power is increased from −50 dBm to 10 dBm (darker to lighter curves). Figure reproduced from [Sei+21].

To demonstrate ground state cooling in this sideband resolved system, we place a pump tone red-detuned from cavity resonance by the mechanical frequency to enable the electro-mechanical beam-spitter interaction (see Sec. 2.5) which extracts quanta from the mechanical oscillator.

As the pump power is increased, we monitor the upper mechanical sideband on resonance and we see three phases in Fig. 5.2. First the measured mechanical peak height increases in the power spectral density (PSD) as the measurement gain goes up (until we reach cooperativity $\mathcal{C} \sim 1$), then the mechanical peak broadens due to light-induced damping. Both these phases are visible in Fig. 5.2A. Lastly, at very high pump powers the phase noise of the pump becomes appreciable and is seen as an increased background level of the spectrum and an ‘inverted’ (also called ‘squashed’) mechanical peak, as seen in Fig. 5.2B.

We fit the measured PSD background level, in Fig. 5.2C, proportionally to pump power (on top of a background level due to the HEMT amplifier). This proportionality allows us to extract the cavity photon occupation due to pump phase noise. This noise cavity occupation increases proportional

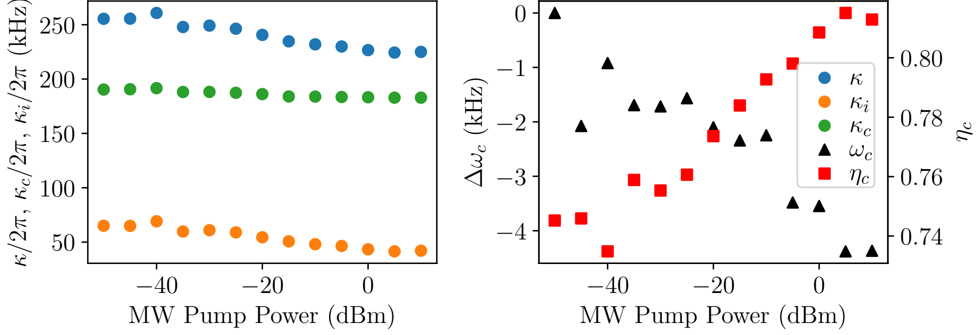

Figure 5.3: The intracavity MW power sweep slightly modifies the cavity parameters, which we adjust for in the ground state cooling analysis.

to pump power. Thus we have two competing effects at play: as the pump power is increased, mechanical quanta are extracted, but at high pump powers, the cavity will be populated limiting the mechanical energy extraction via the beam-splitter interaction.

During the sideband cooling series we again monitor cavity parameters for each power point and plot them in Fig. 5.3. We use this monitor to correct the raw data and extract the correct occupancy in Fig. 5.2D. We reach a lowest occupancy of $\bar{n}_{\mathrm{min}} = 0.76 \pm 0.16$ confirming ground state cooling, before pump phase noise heats up the mechanics. Given our experimental configuration (a sideband resolved cavity with the pump placed at $\omega_{\mathrm{r}} - \Omega_{\mathrm{m}}$) achieving ground state cooling corresponds to $\mathcal{C}_{\mathrm{q}} > 1$.

For further details about the experimental setup, calibration of the ground state occupation and theoretical model, we refer to the manuscript published on the arXiv repository at https://arxiv.org/abs/2107.05552v2. We reproduce the publication in its pre-print form in App. D.

Future improvements to the experiment include improved vibration isolation to reduce the initial mechanical occupation $\bar{n}_{\mathrm{th}}$. We also suspect that the pump phase noise limiting the cooling capability may be due to cavity frequency noise and not noise of the signal generator: indeed we attempted to filter out the instrument phase noise with a narrow-band microwave notch filter set around cavity resonance, and saw no improvement in minimal occupancy $\bar{n}_{\mathrm{min}}$. Better vibration isolation may reduce this cavity frequency noise.

The next step in the electro-mechanics experiment is to characterise the system as a microwave quantum memory. The electro-mechanical quantum cooperativity $\mathcal{C}_{\mathrm{q}} > 1$ would allow us to manipulate genuine quantum states

in the memory. Parameters extracted for the ground state cooling experiment estimate a quantum coherence time $t_{\mathrm{coh}} = (\bar{n}_{\mathrm{th}}\Gamma_{\mathrm{m}})^{-1} \sim 140\,\mathrm{ms}$. A more complete characterisation will be done by preparing and reading out mechanical states, and measuring thermalisation rates as phonons leak into the mechanical mode from the thermal environment.

Chapter 6

Outlook

In this final chapter, we discuss future axes of research prompted by the results of this thesis. The design of a filter to reduce microwave pump phase noise would allow for improved manipulation of the electro-mechanical system. While the next great challenge in our lab is to combine electro-mechanics and opto-mechanics into a single experiment.

6.1 Superconducting Microwave Filter Design

As we have seen in the ground state cooling experiment in Chap.5, operation our devices in the quantum regime becomes limited by phase noise heating. If cavity frequency noise is sufficiently reduced, phase noise of the control pump is the next source of heating. For our low mechanical frequency membrane, we require to filter the pump phase-noise close (at 1.5 MHz) to the carrier. These requirements mean we want a filter with approx. 100 kHz linewidth and tunable over a range of a few GHz. Previously such filtering has been done for electro-mechanical systems where the mechanical frequency was in the tens of MHz, with room-temperature 3D cavities where tuning was done by adjusting the inner volume of the resonator. However the best achievable linewidths for room-temperature resonators is around 1MHz[Lec+15; Tó+17], which in our case would also remove part of the carrier tone.

For more narrow-band filters, we propose a cryogenic superconducting design. In this section, we describe its working principle, the tuning mechanism, and a noise analysis.

Tuning mechanism: Superconducting Kinetic Inductance

Due to their low energy loss, superconducting thin films exhibit an inductance L_K (in addition to any geometric inductance L_G) due to the kinetic energy of their charge carrier: the kinetic inductance (KI)[Xu+19]. Superconductors in the so-called 'clean limit' (where the Cooper pair coherence length is shorter than the electron mean free path in the material) such as for example Al typically exhibit little KI, whereas superconductors in the 'dirty limit' such NbTiN, TiN, NbN etc. have larger KI (and comparatively high critical temperature T_c). Such knowledge is well established in the MW Kinetic Inductance Detector community.

The kinetic part of the inductance is non-linear in the current I flowing through the thin film following

$$L_K(I) = L_{K0}\left(1 + \left(\frac{I}{I^*}\right)^2\right), \tag{6.1}$$

where I^* is a scale comparable to the critical current in the film, and L_{K0} is the kinetic inductance in the low current limit. The full inductance is then

$$L_{tot} = L_G + L_K(I). \tag{6.2}$$

Note that since applying a bias current increases the inductance, the filters can only be dynamically tuned down in frequency[Xu+19].

In addition to the dynamical tuning done by the bias current I, we can also set L_{K0} by geometry. The KI per square is given by[Val+19]

$$L_{K,\square} = \frac{0.18\hbar}{k_B}\frac{R_n}{T_c}, \tag{6.3}$$

where R_n is the normal-state sheet resistance (often measured at room temperature). We may then define a conductor with width w and length l, such that

$$L_{K0} = L_{K,\square}\frac{l}{w}. \tag{6.4}$$

Filter design

Operating Principle

The filter is proposed as follows. On a micro-fabricated chip, we define two coplanar waveguide (CPW) resonators (CPWRs) coupled in a notch-filter (or side coupled) configuration to a main CPW transmission line. The

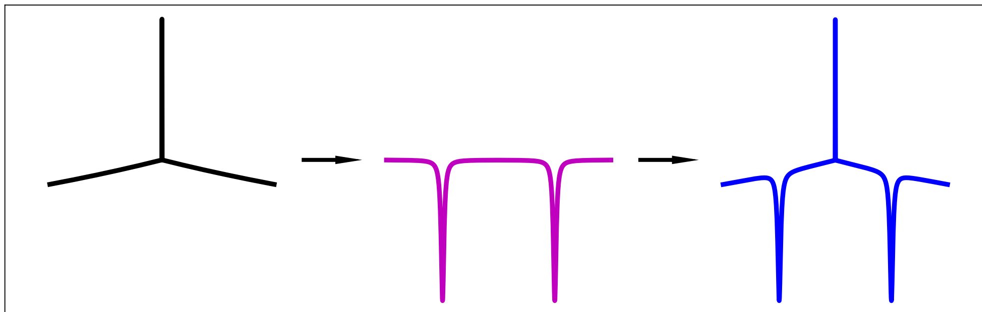

Figure 6.1: Operation of the filter. The MW carrier with its noise sidebands (blue), passes through the notch filters (magenta) which remove the noise at the chosen sideband frequencies and transmit the carrier (blue).

transmission function of each resonator is[Pro+15]:

$$S_{21}(\omega) = 1 - \frac{1}{1 + \kappa_i/\kappa_e - 2i(\omega - \omega_C)/\kappa_e} \tag{6.5}$$

The CPWRs should be in the strongly overcoupled limit such that any signal falling on the resonance of the CPWRs is reflected and thus filtered out from the transmitted signal. The resonances of the CPWRs are tuned to the upper and lower mechanical sideband frequencies $\pm\Omega_\mathrm{m}$ of the MW carrier and remove noise in these frequencies while transmitting the unaffected main carrier (see Fig. 6.1).

A first condition for the carrier to be unaffected by the filter is that the CPWRs, while being strongly overcoupled, still have a total linewidth much less than the mechanical frequency Ω_m. We thus have a hierarchy for the internal κ_i and total κ CPWR loss rates:

$$\kappa_i \ll \kappa \ll \Omega_m, \tag{6.6}$$

then

$$S_{21}(\omega) \approx 1 - \frac{i\kappa}{2(\omega - \omega_C)}. \tag{6.7}$$

Respecting this hierarchy is made possible with commercially deposited NbTiN thin films and standard cleanroom fabrication (as measured in Sec. 4.2), and we can use the fact that in the notch filter configuration the on-resonance transmission tends to zero in the strongly overcoupled limit.

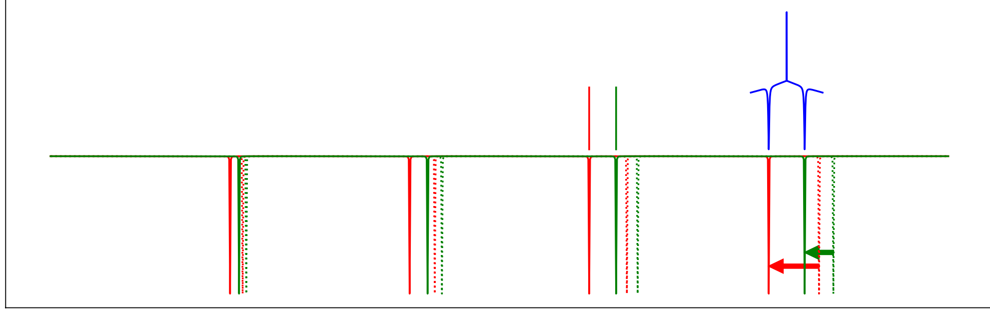

Figure 6.2: Filter tuning. Small pump tones on each resonator (green and red transmission spectra) at a certain FSR (here the third) tune all the FSRs downwards such that the fourth FSRs match the mechanical sidebands of the main carrier.

Gigahertz spanning

For the filter to span the full operating range 4-9GHz, we propose that the CPWRs be designed as long resonators hosting many standing-wave resonances, equally spaced by full-spectral ranges (FSR) on the order of 10s MHz: no matter where our electro-mechanical resonance frequency ends up due to fabrication, we can find a resonance to tune down to the mechanical sideband.

Furthermore, the multiple standing-wave resonances allow us to apply the AC bias current on each CPWR at a different resonance frequency or FSR than the filtering is done at, such that these tuning tones do not interfere with the electro-mechanical device (see Fig. 6.2).

Design Parameters

Using the TXLine software, we find $l = 60\,\mathrm{mm}$, and $w = 5\,\mu\mathrm{m}$ gives a $\lambda/2$ resonator at $\omega_c = 2\pi \cdot 1\,\mathrm{GHz}$ on Si (so FSR of 1 GHz), with $Z_0 = 50\,\Omega$ a the CPW design, if there are no KI effects: we take this geometry as a starting point for the filter resonators. We also obtain $C = (Z_0\omega_c)^{-1} = 3.2\,\mathrm{pF}$ and $L = Z_0/\omega_c = 8.0\,\mathrm{nH}$.

For a realistic tuning resonator, we consider a 20nm thick NbTiN thin film ($R_n \sim 60\,\Omega/\Box$ and $T_c \sim 12.5\,\mathrm{K}$ provided by StarCryo Electronics). Then $L_{K,\Box} = 6.6\,\mathrm{pH}/\Box$ and $L_{K,0} = 76\,\mathrm{nH}$. Firstly we see that the resonance frequency is pulled down to $\omega_c = 2\pi \cdot \mathrm{FSR} = 2\pi \cdot 310\,\mathrm{MHz}$.

For a 100nm thick NbTiN thin film ($R_n \sim 16.4\,\Omega/\Box$ and $T_c \sim 13.5\,\mathrm{K}$), we have $L_{K,\Box} = 1.6\,\mathrm{pH}/\Box$ and $L_{K,0} = 20\,\mathrm{nH}$, and the resonance frequency

is pulled down to $\omega_c = 2\pi \cdot \mathrm{FSR} = 2\pi \cdot\ 530\,\mathrm{MHz}$.

We would like the main waveguide to not have any KI, such that it stays at $Z_0 = 50\,\Omega$ no matter what large power flows through it. Measurements on resonators with superconducting loops of thickness 100 nm, width 10 µm and length 1.5 mm (in Chaps. 4 and 5), have not shown any appreciable non-linearity at millikelvin temperatures, so we probably will not have a non-linear Z_0 for the main waveguide.

Noise Estimations

Since we wish to remove excess phase noise from the carrier sidebands, we must ensure that the filtering process does not also add its own phase noise, coming for example from the filter cavities' frequency noise.

The first choice in this direction is to place the carrier far off-resonant from the filter cavities where the transmission is unity and with a flat phase response: any frequency fluctuations of the cavities induce only very weak phase modulations when far off-resonance. A very detrimental alternative operation would be to place the carrier on transmission of a narrow resonance and rejecting the sidebands: this way would make the carrier very susceptible to cavity jitter at the strong phase slope of the resonance.

Let us non the less compute this far off-resonant phase jitter, which may be of importance if we wish to reduce the phase noise further than its specified $-155\,\mathrm{dBc/Hz}$ level intrinsic to the SMP source. This will give an upper bound on the acceptable frequency noise of the filtering cavities.

Using Eq. 6.7, the transmission phase is

$$\phi_{21} = \frac{\kappa}{2(\omega - \omega_c)} \text{ and,} \tag{6.8a}$$

$$\frac{d\phi_{21}}{d\omega_c} = \frac{\kappa}{2(\omega - \omega_c)^2}. \tag{6.8b}$$

The filter's phase noise $S_{\phi\phi}$ is connected to the filter's resonance frequency ω_c noise $S_{\omega_c\omega_c}$ by

$$S_{\phi\phi} = \left(\frac{d\phi_{21}}{d\omega_c}\right)^2 S_{\omega_c\omega_c}, \tag{6.9}$$

which we would like to be below $-155\mathrm{dBc/Hz}$ in order to not add phase noise in the filter.

Intrinsic material noise

Firstly the material itself creates an intrinsic frequency noise. For NbTiN films (on a high-resistivity Si substrate), Ref. [Bar+08] gives an expression

$$S_{\omega_c\omega_c} = (2.5 \cdot 10^{-19}) \cdot \omega_c^2 \cdot (\Omega/2\pi)^{-0.4}. \tag{6.10}$$

for a sideband Fourier frequency Ω. Taking these numbers, with $\Omega = |\omega - \omega_c| = 2\pi \cdot 1.5\,\text{MHz}$, $\kappa = 2\pi \cdot 200\,\text{kHz}$, we have $S_{\phi\phi} = -161\,\text{dBc/Hz}$; for $\kappa = 2\pi \cdot 100\,\text{kHz}$, we have $S_{\phi\phi} = -167\,\text{dBc/Hz}$.

Once a sample filter is fabricated the measurement of $S_{\omega_c\omega_c}$ would be the first test to assess the viability of this design.

Tuning pump amplitude noise

Secondly, any amplitude noise of the tuning pump's current I will lead to additional frequency noise of the tuned resonator:

$$S_{\omega_c\omega_c} = \left(\frac{d\omega_c}{dI}\right)^2 S_{II}. \tag{6.11}$$

We have $d\omega_c/dL_k = -\omega_c/2(L + L_k)$ and $dL_k/dI = 2L_{K,0}I/I^{*2}$. Measurements on an actual sample will be needed to determine I^{*2}.

Note that these noise estimates are calculated for the filtering of a single sideband. If we have to filter both sidebands (because of a sideband unresolved electromechanical device), this filter phase noise number has to be multiplied by 2.

Further, κ_e will be the only parameter that we can easily change in the filter design. Thus, if hierarchy 6.6 if too stringent, $\kappa \ll \Omega_m$ is sufficient to keep the filter added noise low, but a larger κ_i will mean less filtering of the noise sideband.

6.2 Towards Electro-Opto-Mechanics

Future research in the group will endeavour to combine the quantum electromechanics (see Sec. 5) and opto-mechanics[Che+20; Ros+19; Ros+18] research in our lab. The operation of a membrane-based electro-opto-mechanical system[Bag+14; And+14] operating in the quantum regime would allow for the frequency conversion of quanta of between the microwave and optical regions of the electromagnetic spectrum[Tia12]. Previous experimental realisations of microwave-optics transduction in various other systems have

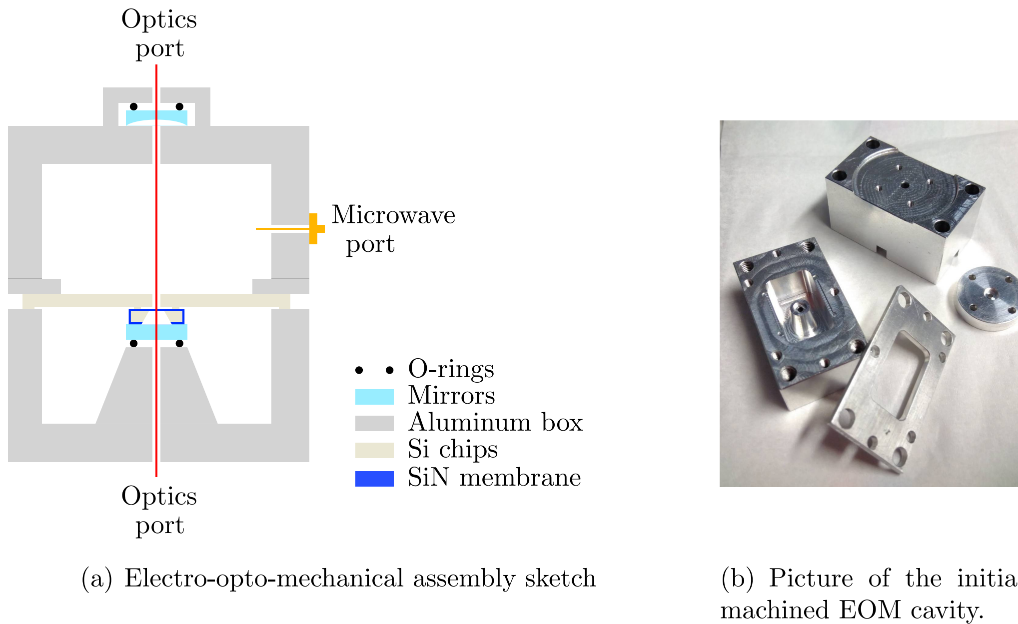

(a) Electro-opto-mechanical assembly sketch

(b) Picture of the initial machined EOM cavity.

Figure 6.3: The electro-opto-mechanical assembly is composed at its centre of the electro-mechanics flip-chip. The optical Fabry-Pérot cavity axis goes through an opening in the MW resonator chip to couple to the membrane.

suffered from low conversion efficiency or too high added noise to preserve the quantum state[Hig+18; Mir+20; Hea+20].

The successful integration of ultra-coherent mechanical oscillators into microwave and optical cavities separately, both operated in the quantum regime, gives reason to continue our efforts towards full integration to bridge such heterogenous components that are 8 GHz microwave photons, 1.5 MHz phonons and 350 THz optical photons.

We present a sketch of the assembly in Fig.6.3. At the centre of the assembly is the electro-mechanical flip-chip, which is read out as above via the magnetic coupling to a coaxial connector. Around the membrane we place two high-reflective mirrors (one flat and one concave curved mirror) to create an overcoupled Fabry-Pérot cavity modulated by the displacement of the dielectric membrane. Shining the laser through the flip-chip is allowed by a hole through the Si substrate of the superconducting resonator as depicted in Fig. 3.3, such that only the membrane occupies the optical cavity axis.

A first machined design of the assembly as designed together with Junxin Chen is shown in Fig. 6.3(b). The assembly starts with a bottom half with a central pillar to hold the flat mirror, and a thin clamping ring pushing

the electro-mechanical flip-chip against the flat mirror. A top half closes the assembly and holds the microwave incoupler, finally a curved mirror is placed atop the top half and held by a circular clamp.

Important considerations which need to be taken care of by Eric Planz and Thibault Capelle in their testing of this monolithic assembly are the mechanical stability of the flip-chip and of the optical axis. To insure parallelity of the bottom flat mirror with the membrane, we contact the flip-chip with the mirror. The contact force however will bend the Si and may lead to collapse of the membrane onto the MW resonator or chip fracture during assembly, or when cooling down or heating up the sample. Further testing will establish the mechanical stability of the optical cavity in presence of the flip-chip and whether this new assembly (mounted on a mechanical damper) is sufficiently stable to lock the laser wavelength to the optical cavity length.

A more fundamental difficulty is the heating of the Si_3N_4 membrane by absorption of laser light in the millikelvin environment. The scattering of laser light in our dilution refrigerator can heat up samples from base temperature to above 1 K within seconds. This heating can compromise the electromechanics side by reducing mechanical and microwave quality factors, and increasing the bath population, making quantum operation on the microwave side more difficult. Preliminary measurements of the heating due to optical absorption in the membrane material have been performed by Massimiliano Rossi and David Mason in Fig. S11 of Ref. [Pag+20] (see also Ref. [Fis+16]) and heat diffusion simulations in the membrane at millikelvin temperatures were performed by Eric Langman.

The group's continued simulation, fabrication, and optics efforts and expertise make us optimistic as to the success of the electro-opto-mechanics endeavour. The ground state cooling result of this thesis with $\mathcal{C}_\mathrm{q} > 1$ is an important achievement as it is a necessary condition for the electro-mechanical interface of a transducer to maintain the quantum nature of the transduced state.

Appendix A

Circuit Analysis

In this appendix, we derive impedance transformations for the circuit model.

A.1 Impedance transformation of the mutually coupled inductors

Here we briefly justify the transformation of the impedance of two inductors coupled by their mutual inductance to a T-piece geometry as depicted in Fig. A.1.

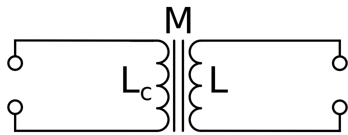

(a) Two inductances coupled by their mutual inductance.

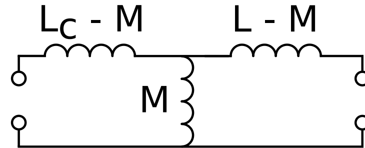

(b) Equivalent impedance in a T-piece topology.

Figure A.1: The two-port mutually coupled inductances can be transformed into three inductances placed in a T-piece topology.

This transformation can be proven by using the two-port impendance matrix:

$$\mathbf{Z} = \begin{pmatrix} Z_{11} & Z_{12} \\ Z_{21} & Z_{22} \end{pmatrix} \tag{A.1}$$

where $Z_{l_1 l_2} = \left.\frac{V_{l_1}}{I_{l_2}}\right|_{I_{\overline{l_2}}=0}$, with $\overline{l_2}$ the port that is not l_2; such that

$$\begin{pmatrix} V_1 \\ V_2 \end{pmatrix} = \begin{pmatrix} Z_{11} & Z_{12} \\ Z_{21} & Z_{22} \end{pmatrix} \begin{pmatrix} I_1 \\ I_2 \end{pmatrix}. \tag{A.2}$$

Then, from the definition of mutual inductance and series inductance addition respectively, we can show that both circuits satisfy

$$\mathbf{Z} = i\omega \begin{pmatrix} L_c & M \\ M & L \end{pmatrix}. \tag{A.3}$$

Appendix B

Hamiltonian and equations of motion

Here we derive the Hamiltonian and equations of motions for the opto-mechanical system from basics. These results can be found in the literature[AKM14] and are reproduced here mainly for the benefit of the author of this thesis.

B.1 Hamiltonian in the rotating frame

The Hamiltonian of the opto-mechanical system with an interaction to first order in the mechanical operator is:

$$\hat{H} = \hbar\omega_r \hat{a}^\dagger \hat{a} + \hbar\Omega_m \hat{b}^\dagger \hat{b} - \hbar G x_{\text{zpf}} \hat{a}^\dagger \hat{a}(\hat{b} + \hat{b}^\dagger) + i\hbar\sqrt{\kappa_e}(\hat{a}\hat{a}_{\text{in}}^\dagger e^{i\omega_L t} - \hat{a}^\dagger \hat{a}_{\text{in}} e^{-i\omega_L t}) \tag{B.1}$$

where the first two terms are the energies of the cavity and of the mechanics, the third is the interaction term linear in $\hat{x} = x_{\text{zpf}}(\hat{b}+\hat{b}^\dagger)$, the last two terms are the driving terms due to the external field entering the cavity. Then we move to a frame rotating with the drive frequency ω_L, by changing to the Hamiltonian

$$\hat{H}_{\text{rot}} = \hat{U}\hat{H}\hat{U}^\dagger - i\hbar\hat{U}\frac{\partial \hat{U}^\dagger}{\partial t}, \tag{B.2}$$

with the unitary operator $\hat{U} = \exp(i\hat{H}_0 t/\hbar) = \exp(i\omega_L \hat{a}^\dagger \hat{a} t) = \sum_{k=0}^{\infty}(i\omega_L \hat{a}^\dagger \hat{a} t)^k/k!$ and $\hat{U}^\dagger = \exp(-i\omega_L \hat{a}^\dagger \hat{a} t)$.

We have $\left[\hat{a}^\dagger \hat{a}, U\right] = 0$ since $\left[\hat{a}^\dagger \hat{a}, (\hat{a}^\dagger \hat{a})^k\right] = 0$ for any integer k, therefore the transformation $\hat{U}\hat{H}\hat{U}^\dagger$ leaves the first three terms of $\hat{H}$ unaffected. The

driving terms however become time-independent:

$$\hat{U}\hat{a}e^{i\omega_L t}\hat{U}^\dagger = \hat{a}, \tag{B.3a}$$

$$\hat{U}\hat{a}^\dagger e^{-i\omega_L t}\hat{U}^\dagger = \hat{a}^\dagger. \tag{B.3b}$$

In addition, we have

$$\hat{U}\frac{\partial \hat{U}^\dagger}{\partial t} = -i\hat{U}\omega_L \hat{a}^\dagger \hat{a}\hat{U}^\dagger = -i\omega_L \hat{a}^\dagger \hat{a}. \tag{B.4}$$

Finally the Hamiltonian in the rotating frame is

$$\hat{H}_{rot} = -\hbar\Delta\hat{a}^\dagger\hat{a} + \hbar\Omega_m \hat{b}^\dagger\hat{b} - \hbar G x_{\text{zpf}}\hat{a}^\dagger\hat{a}(\hat{b}+\hat{b}^\dagger) + i\hbar\sqrt{\kappa_e}(\hat{a}\hat{a}_{\text{in}}^\dagger - \hat{a}^\dagger\hat{a}_{\text{in}}). \tag{B.5}$$

with the pump detuning from cavity resonance $\Delta = \omega_L - \omega_r$.

Note 1: we obtain Eq. B.2 by using

$$|\tilde{\Psi}(t)\rangle = \hat{U}|\Psi(t)\rangle, \tag{B.6}$$

and requiring

$$\hat{H}|\Psi(t)\rangle = i\hbar\partial_t|\Psi(t)\rangle, \text{ and} \tag{B.7}$$

$$\hat{H}_{\text{rot}}|\tilde{\Psi}(t)\rangle = i\hbar\partial_t|\tilde{\Psi}(t)\rangle. \tag{B.8}$$

Then we have:

$$\begin{aligned} \hat{H}U^\dagger|\tilde{\Psi}(t)\rangle &= i\hbar\partial_t(U^\dagger|\tilde{\Psi}(t)\rangle) = i\hbar(\partial_t U^\dagger)|\tilde{\Psi}(t)\rangle + i\hbar U^\dagger\partial_t|\tilde{\Psi}(t)\rangle \\ &= i\hbar(\partial_t U^\dagger)|\tilde{\Psi}(t)\rangle + U^\dagger\hat{H}_{\text{rot}}|\tilde{\Psi}(t)\rangle. \end{aligned} \tag{B.9}$$

and we can retrieve the above expression for $\hat{H}_{\text{rot}}$.

Note 2: we obtain Eqs. B.3 by transforming the (time-independent) operator $\hat{a}_S$ from the Schrödinger picture to the interaction picture. The operation $\hat{a}_I(t) = \hat{U}\hat{a}_S\hat{U}^\dagger$ is equivalent to solving

$$\begin{aligned} i\hbar\frac{d}{dt}\hat{a}_I(t) &= \left[\hat{a}_I(t), \hat{H}_0\right] = \hbar\omega_L\left[\hat{a}_I(t), \hat{a}_I(t)^\dagger\hat{a}_I(t)t\right] \\ &= \hbar\omega_L t\,\hat{a}_I(t) \end{aligned} \tag{B.10}$$

where we have made use of the fact that $\hat{a}_I(t)^\dagger\hat{a}_I(t) = \hat{a}_S^\dagger\hat{a}_S$, as derived above. Then we solve:

$$\hat{a}_I(t) = \hat{a}_I(0)\exp(-i\omega_L t). \tag{B.11}$$

and a similar expression for $\hat{a}_I^\dagger(t) = \hat{a}_I^\dagger(0)\exp(i\omega_L t)$.

B.2 Equations of motion

We now derive the equations of motion for $\hat{a}$ and $\hat{b}$, and then of $\hat{x}$ from the Hamiltonian in the rotating frame given by Eq. B.5.

Given an interaction picture operator O, its unitary Heisenberg equation of motion is

$$i\hbar\frac{d}{dt}\hat{O} = \left[\hat{O}, \hat{H}_{\text{rot}}\right]. \tag{B.12}$$

We derive

$$\begin{cases} \dot{\hat{a}} = \frac{-i}{\hbar}\left[\hat{a}, \hat{H}_{\text{rot}}\right] & = i\left(\Delta + Gx_{\text{zpf}}(\hat{b}+\hat{b}^\dagger)\right)\hat{a} - \sqrt{\kappa_e}\hat{a}_{\text{in}}, \\ \dot{\hat{b}} = \frac{-i}{\hbar}\left[\hat{b}, \hat{H}_{\text{rot}}\right] & = -i\Omega_m\hat{b} + iGx_{\text{zpf}}\hat{a}^\dagger\hat{a}, \\ \dot{\hat{b}}^\dagger = \frac{-i}{\hbar}\left[\hat{b}^\dagger, \hat{H}_{\text{rot}}\right] & = i\Omega_m\hat{b}^\dagger - iGx_{\text{zpf}}\hat{a}^\dagger\hat{a}. \end{cases} \tag{B.13}$$

Then we add loss mechanisms by hand:

$$\begin{cases} \dot{\hat{a}} & = -\frac{\kappa}{2}\hat{a} + i\left(\Delta + Gx_{\text{zpf}}(\hat{b}+\hat{b}^\dagger)\right)\hat{a} - \sqrt{\kappa_e}\hat{a}_{\text{in}} + \sqrt{\kappa_i}\hat{f}_{\text{in}}, \\ \dot{\hat{b}} & = \left(-i\Omega_m - \frac{\Gamma_m}{2}\right)\hat{b} + iGx_{\text{zpf}}\hat{a}^\dagger\hat{a} + \sqrt{\Gamma_m}\hat{b}_{\text{in}}, \\ \dot{\hat{b}}^\dagger & = \left(i\Omega_m - \frac{\Gamma_m}{2}\right)\hat{b}^\dagger - iGx_{\text{zpf}}\hat{a}^\dagger\hat{a} + \sqrt{\Gamma_m}\hat{b}_{\text{in}}^\dagger, \end{cases} \tag{B.14}$$

and we use a strong coherent pump ($\hat{a} \to \alpha + \delta\hat{a}$) and keep only the linear terms in $\delta\hat{a}, \delta\hat{a}^\dagger$:

$$\begin{cases} \delta\dot{\hat{a}} & = \left(i\Delta - \frac{\kappa}{2}\right)\delta\hat{a} + iGx_{\text{zpf}}\alpha(\hat{b}+\hat{b}^\dagger) - \sqrt{\kappa_e}\delta\hat{a}_{\text{in}} + \sqrt{\kappa_i}\hat{f}_{\text{in}}, \\ \dot{\hat{b}} & = \left(-i\Omega_m - \frac{\Gamma_m}{2}\right)\hat{b} + iGx_{\text{zpf}}(\alpha\delta\hat{a}^\dagger + \alpha^*\delta\hat{a}) + \sqrt{\Gamma_m}\hat{b}_{\text{in}}, \\ \dot{\hat{b}}^\dagger & = \left(i\Omega_m - \frac{\Gamma_m}{2}\right)\hat{b}^\dagger - iGx_{\text{zpf}}(\alpha\delta\hat{a}^\dagger + \alpha^*\delta\hat{a}) + \sqrt{\Gamma_m}\hat{b}_{\text{in}}^\dagger. \end{cases} \tag{B.15}$$

Eqs. B.15 describe the quantum fluctuations of the mechanics and of the cavity field around its classical average value.

We may also derive classical equations of motion for the average values of the mechanics and the cavity in the large quanta limit. From Eqs. B.14, we write:

$$\begin{cases} \ddot{\hat{b}} & = \frac{-i}{\hbar}\left[\dot{\hat{b}}, \hat{H}_{\text{rot}}\right] = \frac{-i}{\hbar}\left(-i\Omega_m - \frac{\Gamma_m}{2}\right)\left[\hat{b}, \hat{H}_{\text{rot}}\right] = \left(-i\Omega_m - \frac{\Gamma_m}{2}\right)\dot{\hat{b}}, \\ \ddot{\hat{b}}^\dagger & = \frac{-i}{\hbar}\left[\dot{\hat{b}}^\dagger, \hat{H}_{\text{rot}}\right] = \frac{-i}{\hbar}\left(i\Omega_m - \frac{\Gamma_m}{2}\right)\left[\hat{b}^\dagger, \hat{H}_{\text{rot}}\right] = \left(i\Omega_m - \frac{\Gamma_m}{2}\right)\dot{\hat{b}}^\dagger; \end{cases} \tag{B.16}$$

then we substitute $\dot{\hat{b}}^\dagger$ and $\dot{\hat{b}}$ from Eqs. B.14 (while ignoring terms in $\hat{b}_{\text{in}}^\dagger$ and $\hat{b}_{\text{in}}^\dagger$ anticipating taking the average value, where these will go to zero):

$$\begin{cases} \ddot{\hat{b}} & = -i\Omega_m \left[\left(-i\Omega_m - \frac{\Gamma_m}{2}\right)\hat{b} + iGx_{\text{zpf}}\hat{a}^\dagger\hat{a}\right] - \frac{\Gamma_m}{2}\dot{\hat{b}} \\ & = -\Omega_m^2\hat{b} + Gx_{\text{zpf}}\Omega_m\hat{a}^\dagger\hat{a} - \Gamma_m\dot{\hat{b}}, \\ \ddot{\hat{b}}^\dagger & = i\Omega_m \left[\left(i\Omega_m - \frac{\Gamma_m}{2}\right)\hat{b}^\dagger - iGx_{\text{zpf}}\hat{a}^\dagger\hat{a}\right] - \frac{\Gamma_m}{2}\dot{\hat{b}}^\dagger \\ & = -\Omega_m^2\hat{b}^\dagger + Gx_{\text{zpf}}\Omega_m\hat{a}^\dagger\hat{a} - \Gamma_m\dot{\hat{b}}^\dagger. \end{cases} \tag{B.17}$$

where in the last step we make use, from Eqs. B.13, of the free mechanical evolution $i\Omega_m\hat{b} = \dot{\hat{b}}$.

Finally we obtain:

$$\begin{cases} \dot{\alpha} & = -\frac{\kappa}{2}\alpha + i\left(\Delta + Gx\right)\alpha - \sqrt{\kappa_e}\alpha_{\text{in}} \\ m_{\text{eff}}\ddot{x} & = -m_{\text{eff}}\Omega_m^2 x - m_{\text{eff}}\Gamma_m\dot{x} + \hbar G|\alpha|^2 \end{cases} \tag{B.18}$$

where $2m_{\text{eff}}x_{\text{zpf}}^2\Omega_m = \hbar$,

$$\begin{cases} \alpha & = \langle\hat{a}\rangle, \\ \alpha_{\text{in}} & = \langle\hat{a}_{\text{in}}\rangle, \\ \ddot{x} & = x_{\text{zpf}}\left\langle\left(\ddot{\hat{b}} + \ddot{\hat{b}}^\dagger\right)\right\rangle, \\ \dot{x} & = x_{\text{zpf}}\left\langle\left(\dot{\hat{b}} + \dot{\hat{b}}^\dagger\right)\right\rangle, \text{and} \\ x & = x_{\text{zpf}}\left\langle\left(\hat{b} + \hat{b}^\dagger\right)\right\rangle; \end{cases} \tag{B.19}$$

and the linearised form:

$$\begin{cases} \delta\dot{\alpha} & = \left(-\frac{\kappa}{2} + i\Delta\right)\delta\alpha + iG\bar{\alpha}x - \sqrt{\kappa_e}\delta\alpha_{\text{in}} \\ m_{\text{eff}}\ddot{x} & = -m_{\text{eff}}\Omega_m^2 x - m_{\text{eff}}\Gamma_m\dot{x} + \hbar G(\bar{\alpha}^*\delta\alpha + \bar{\alpha}\delta\alpha^*) \end{cases} \tag{B.20}$$

where we have redefined $\alpha \to \bar{\alpha} + \delta\alpha$ and $x \to \bar{x} + x$ and we have disregarded the static displacement of the mechanics to a new equilibrium point, which is due to static radiation pressure force. The average values can be found by solving Eqs. B.18 and setting all derivatives to zero:

$$\begin{cases} \bar{\alpha} & = \frac{-\sqrt{\kappa_e}}{-i(\Delta+G\bar{x})+\kappa/2}\bar{\alpha}_{\text{in}} \\ \bar{x} & = \frac{\hbar G|\alpha|^2}{m_{\text{eff}}\Omega_m^2}, \end{cases} \tag{B.21}$$

which also redefines the detuning $\Delta + G\bar{x} \to \Delta$.

In the frequency domain, we use the Fourier transform of all the variables following $\hat{a}[\omega] = \mathcal{F}(\hat{a}) = \int_{-\infty}^{+\infty} e^{i\omega t}\hat{a}dt$, such that $\mathcal{F}\left(\dot{\hat{a}}\right) = -i\omega\hat{a}[\omega]$. Then Eqs. B.15 and B.20 become:

$$\begin{cases} -i\omega\delta\hat{a}[\omega] = & \left(i\Delta - \frac{\kappa}{2}\right)\delta\hat{a}[\omega] + iGx_{\text{zpf}}\bar{\alpha}(\hat{b}[\omega] + \hat{b}^\dagger[\omega]) \\ & -\sqrt{\kappa_e}\delta\hat{a}_{\text{in}}[\omega] + \sqrt{\kappa_i}\hat{f}_{\text{in}}[\omega], \\ -i\omega\hat{b}[\omega] = & \left(-i\Omega_m - \frac{\Gamma_m}{2}\right)\hat{b}[\omega] + iGx_{\text{zpf}}(\bar{\alpha}\delta\hat{a}^\dagger[\omega] + \bar{\alpha}^*\delta\hat{a}[\omega]) \\ & +\sqrt{\Gamma_m}\hat{b}_{\text{in}}[\omega], \\ -i\omega\hat{b}^\dagger[\omega] = & \left(i\Omega_m - \frac{\Gamma_m}{2}\right)\hat{b}^\dagger[\omega] - iGx_{\text{zpf}}(\bar{\alpha}\delta\hat{a}^\dagger[\omega] + \bar{\alpha}^*\delta\hat{a}[\omega]) \\ & +\sqrt{\Gamma_m}\hat{b}^\dagger_{\text{in}}[\omega]. \end{cases} \tag{B.22}$$

and

$$\begin{cases} -i\omega\delta\alpha[\omega] & = \left(-\frac{\kappa}{2} + i\Delta\right)\delta\alpha[\omega] + iG\bar{\alpha}x - \sqrt{\kappa_e}\delta\alpha_{\text{in}}[\omega] \\ -\omega^2 m_{\text{eff}}x[\omega] & = -m_{\text{eff}}\Omega_m^2 x[\omega] + i\omega m_{\text{eff}}\Gamma_m x[\omega] + \hbar G(\bar{\alpha}^*\delta\alpha[\omega] + \bar{\alpha}(\delta\alpha^*)[\omega]). \end{cases} \tag{B.23}$$

where $\hat{a}^\dagger[\omega] = (\hat{a}[-\omega])^\dagger$ must hold, thus also $\delta\alpha^*[\omega] = (\delta\alpha[-\omega])^*$.

B.3 Dynamical Backaction

We now look at how the opto-mechanical interaction modifies the properties of the mechanics. We solve Eq. B.23 for $\delta\alpha$ in terms of x

$$\begin{cases} \delta\alpha[\omega] & = \frac{G\bar{\alpha}}{-(\Delta+\omega)-i\kappa/2}x[\omega] \\ \delta\alpha^*[\omega] & = \frac{G\bar{\alpha}^*}{-(\Delta-\omega)+i\kappa/2}x[\omega] \end{cases} \tag{B.24}$$

Then we may write the equation, for the mechanical susceptibility χ_{eff}, of the small force mechanical response $F[\omega]\chi_{\text{eff}}(\omega) = x[\omega]$. Solving for x:

$$\begin{aligned} F = & -\omega^2 m_{\text{eff}}x[\omega] + m_{\text{eff}}\Omega_m^2 x[\omega] - i\omega m_{\text{eff}}\Gamma_m x[\omega] \\ & + \hbar G(\bar{\alpha}^*\delta\alpha[\omega] + \bar{\alpha}(\delta\alpha^*)[\omega]) \\ = & \Big[m_{\text{eff}}\left(-\omega^2 + \Omega_m^2 - i\omega\Gamma_m\right) \\ & +\hbar G^2|\bar{\alpha}|^2\left(\frac{1}{(\Delta+\omega)+i\kappa/2} + \frac{1}{(\Delta-\omega)-i\kappa/2}\right)\Big]x[\omega] \end{aligned} \tag{B.25}$$

from which we have

$$\chi_{\text{eff}}[\omega]^{-1} = \left[\chi(\omega)^{-1} + \hbar G^2|\bar{\alpha}|^2\left(\frac{1}{(\Delta+\omega)+i\kappa/2} + \frac{1}{(\Delta-\omega)-i\kappa/2}\right)\right] \tag{B.26}$$

with the bare mechanical susceptibility $\chi(\omega)^{-1} = m_{\text{eff}}\left(-\omega^2 + \Omega_m^2 - i\omega\Gamma_m\right)$ and where we call the light induced modification $\Sigma(\omega)$.

The light field modifies the mechanical frequency and linewidth which are associated with the real and imaginary parts of $\Sigma(\omega)$. If we rewrite

$$\begin{aligned}\chi_{\text{eff}}(\omega)^{-1} &= m_{\text{eff}}\left[-\omega^2 + (\Omega_m + \delta\Omega_m(\omega))^2 - i\omega\left(\Gamma_m + \Gamma_{opt}(\omega)\right)\right] \\ &\approx m_{\text{eff}}\left[-\omega^2 + \Omega_m^2 + 2\Omega_m\delta\Omega_m(\omega) - i\omega\left(\Gamma_m + \Gamma_{opt}(\omega)\right)\right] \\ &= m_{\text{eff}}\left[-\omega^2 + \Omega_m^2 + \frac{1}{m_{\text{eff}}}Re\{\Sigma(\omega)\} - i\omega\Gamma_m + \frac{i}{m_{\text{eff}}}Im\{\Sigma(\omega)\}\right],\end{aligned} \tag{B.27}$$

we can identify, setting $\omega = \Omega_m$ (valid in the high-Q limit, $\Gamma_m + \Gamma_{opt} << \kappa$),

$$\begin{aligned}\delta\Omega_m &= \frac{1}{2m_{\text{eff}}\Omega_m}Re\left\{\Sigma(\Omega_m)\right\} \\ &= \frac{\hbar G^2|\bar{\alpha}|^2}{2m_{\text{eff}}\Omega_m}\left(\frac{\Delta + \Omega_m}{(\Delta + \Omega_m)^2 + (\kappa/2)^2} + \frac{\Delta - \Omega_m}{(\Delta - \Omega_m)^2 + (\kappa/2)^2}\right)\end{aligned} \tag{B.28}$$

$$\begin{aligned}\Gamma_{opt} &= \frac{-1}{m_{\text{eff}}\Omega_m}Im\left\{\Sigma(\Omega_m)\right\} \\ &= \frac{\hbar G^2|\bar{\alpha}|^2}{2m_{\text{eff}}\Omega_m}\left(\frac{+\kappa}{(\Delta + \Omega_m)^2 + (\kappa/2)^2} + \frac{-\kappa}{(\Delta - \Omega_m)^2 + (\kappa/2)^2}\right),\end{aligned} \tag{B.29}$$

where we have $\frac{\hbar G^2|\bar{\alpha}|^2}{2m_{\text{eff}}\Omega_m} = g_0^2|\bar{\alpha}|^2$; note that, in the unresolve sideband regime, $|\bar{\alpha}|^2$ depends significantly on Δ following Eq. B.21.

If we set the drive on the blue ($\Delta = +\Omega_m$) or red ($\Delta = -\Omega_m$) sideband, we have

$$\delta\Omega_m|_{\Delta=\pm\Omega_m} = \pm g_0^2|\bar{\alpha}|^2\frac{2\Omega_m}{4\Omega_m^2 + \kappa^2/4} \tag{B.30}$$

$$\Gamma_{opt}|_{\Delta=\pm\Omega_m} = \pm g_0^2|\bar{\alpha}|^2\left(\frac{\kappa}{4\Omega_m^2 + \kappa^2/4} - \frac{4}{\kappa}\right) = \frac{\pm 4g_0^2|\bar{\alpha}|^2}{\kappa}\left(\frac{1}{1 + 16(\Omega_m/\kappa)^2} - 1\right). \tag{B.31}$$

B.4 Electro-Mechanically Induced Reflection

Let us now look at a simple two tone setup, with one strong pump and a weak probe tone. We use the linearised approximation in Eqs. B.20 where the pump is the large classical field $\bar{\alpha}_{\text{in}}$ at frequency ω_L, $\bar{\alpha}_{\text{in}} = \bar{\alpha}_L e^{-i\omega_L t}$: this tone provides the multi-photon enhancement of the opto-mechanical

interaction via a large intra-cavity photon number $n_{\text{cav}} = |\bar{\alpha}|^2 = \kappa_e/(\Delta^2 + (\kappa/2)^2)|\bar{\alpha}_L|^2$ and sets the rotating frame which we consider. The weak probe tone is the $\delta\alpha_{\text{in}}$ field in the equation of motion at frequency ω_p, detuned by $\Omega = \omega_p - \omega_L$ from the pump.

This derivation is taken from the Supplementary of Ref. [Wei+10].

We take the ansatz solution at the same frequency as the perturbative probe drive $\delta\alpha_{\text{in}} = \alpha_p e^{-i\Omega t}$:

$$\begin{cases} \delta\alpha(t) = A^- e^{-i\Omega t} + A^+ e^{i\Omega t} \\ \delta\alpha^*(t) = (A^+)^* e^{-i\Omega t} + (A^-)^* e^{i\Omega t} \\ x(t) = X e^{-i\Omega t} + X^* e^{i\Omega t}. \end{cases} \tag{B.32}$$

We plug these expressions into Eqs. B.20 and only keep the terms with $e^{-i\Omega t}$ since that is the frequency of the probe.

$$\begin{cases} (-i(\Delta + \Omega) + \kappa/2)A^- & = iG\bar{\alpha}X + \sqrt{\kappa_e}\alpha_p \\ (i(\Delta - \Omega) + \kappa/2)(A^+)^* & = -iG\bar{\alpha}X \\ m_{\text{eff}}(\Omega_m^2 - \Omega^2 - i\Gamma_m\Omega)X & = \hbar G\alpha\left(A^- + (A^+)^*\right). \end{cases} \tag{B.33}$$

Solving Eqs. B.33 for A^- yields

$$A^- = \frac{1 + if(\Omega)}{-i(\Delta + \Omega) + \kappa/2 + 2\Delta f(\Omega)}\sqrt{\kappa_e}\alpha_p \tag{B.34}$$

with

$$f(\Omega) = \hbar G^2 \alpha^2 \frac{\chi(\Omega)}{i(\Delta - \Omega) + \kappa/2} \tag{B.35}$$

and the mechanical susceptibility

$$\chi(\Omega) = \left[m_{\text{eff}}(\Omega_m^2 - \Omega^2 - i\Gamma_m\Omega)\right]^{-1}. \tag{B.36}$$

Then the outgoing light can be computed using the input-output relation:

$$\begin{aligned} \alpha(t) &= \alpha_{\text{in}}(t) - \sqrt{\kappa_e}\alpha(t) \\ &= (\alpha_L - \sqrt{\kappa_e}\bar{\alpha})e^{-i\omega_L t} + (\alpha_p - \sqrt{\kappa_e}A^-)e^{-i(\omega_L+\Omega)t} - \sqrt{\kappa_e}A^+ e^{-i(\omega_L-\Omega)t} \end{aligned} \tag{B.37}$$

where for completeness we have the pump tone, along with the positive and negative frequency sidebands at $\omega_L \pm \Omega$. We now compute the transmission

amplitude of the probe tone (which is the positive frequency sideband)

$$\begin{aligned} r_p &= \frac{\alpha_p - \sqrt{\kappa_e} A^-}{\alpha_p} \\ &= 1 - \kappa_e \frac{1 + i f(\Omega)}{-i(\Delta + \Omega) + \kappa/2 + 2\Delta f(\Omega)}. \end{aligned} \tag{B.38}$$

We point out that most reflection or transmission experiments (homodyne detection or vector network analysis) measure the field at the same frequency as the probe is sent out, which is why we do not need to compute the A^+ component in Eq. B.37 above.

Special Cases

If we set the pump on resonance with the cavity resonance $(\Delta = 0)$, then near the mechanical sidebands ($\delta = \Omega \pm \Omega_m$, $|\delta| \ll \Omega_m$), we can approximate the mechanical susceptibility by a Lorentzian:

$$\chi(\delta) \approx \mp (m_{\text{eff}} \Omega_m)^{-1} / (2\delta - i\Gamma_m); \tag{B.39}$$

we write:

$$f(\delta) = \mp \frac{\hbar G^2 |\bar{\alpha}|^2}{m_{\text{eff}} \Omega_m} (2\delta - i\Gamma_m)^{-1} (\pm i\Omega_m + \kappa/2)^{-1} \tag{B.40}$$

$$= \mp \mathcal{C} \left(\frac{2\delta}{\Gamma_m} - i \right)^{-1} \left(\pm i \frac{2\Omega_m}{\kappa} + 1 \right)^{-1}, \tag{B.41}$$

with the optomechanical cooperativity $\mathcal{C} = 4 g_0^2 n_{\text{cav}} / \kappa \Gamma_m$. The reflected signal from the 1-port cavity is:

$$r_p(\delta) = 1 - \kappa_e \frac{1 + i f(\delta)}{(\pm i\Omega_m + \kappa/2)} \tag{B.42}$$

And in the limit $\kappa \gg \Omega_m$,

$$r_p(\delta) = 1 - 2\eta_c \pm 2\eta_c \frac{\mathcal{C}}{-2i\delta/\Gamma_m - 1} \tag{B.43}$$

with the cavity outcoupling efficiency $\eta_c = \kappa_e/\kappa$. In this regime, we see that the mechanical transparency feature of the two sidebands are anti-symmetric around the point $1 - 2\eta_c$ in the complex plane of reflection coefficients.

If we set the pump on a mechanical sideband of the cavity ($\Delta = \pm\Omega_m$), then the transmission on resonance ($\delta = \Omega \pm \Omega_m$, $|\delta| \ll \Omega_m, \kappa$), we have:

$$\begin{aligned} f(\delta) &= \mp \frac{4\hbar G^2 \alpha^2}{2m_{\text{eff}}\Omega_m \kappa \Gamma_m} \frac{\kappa}{4\Omega_m} \left(\frac{2\delta}{\Gamma_m} - i\right)^{-1} \left(\frac{\kappa}{4\Omega_m} \pm i\right)^{-1} \\ &= \mp \mathcal{C} \frac{\kappa}{4\Omega_m} \left(\frac{2\delta}{\Gamma_m} - i\right)^{-1} \left(\frac{\kappa}{4\Omega_m} \pm i\right)^{-1}. \end{aligned} \tag{B.44}$$

$$\begin{aligned} r_p(\delta) &= 1 - \kappa_e \frac{1 + i f(\delta)}{\kappa/2 \pm 2\Omega_m f(\delta)} \\ &= 1 - 2\eta_c \frac{1 \mp i\mathcal{C} \frac{\kappa}{4\Omega_m} \left(\frac{2\delta}{\Gamma_m} - i\right)^{-1} \left(\frac{\kappa}{4\Omega_m} \pm i\right)^{-1}}{1 - \mathcal{C} \left(\frac{2\delta}{\Gamma_m} - i\right)^{-1} \left(\frac{\kappa}{4\Omega_m} \pm i\right)^{-1}}. \end{aligned} \tag{B.45}$$

Mechanical Characterisation

In the vicinity of the mechanical resonance, Eq. B.45 describes a Lorentzian peak, which we can analyse to extract mechanical parameters. We place the pump on the red side of the resonance ($\Delta = -\Omega_m$) and offset the reflection measurement $t_d(\delta)$ by the value of the cavity reflection without interaction ($\mathcal{C} = 0$, $t_d(\delta)|_{\mathcal{C}=0} = 1 - 2\eta_c$):

$$r_p(\delta) - r_d(\delta)|_{\mathcal{C}=0} = -2\eta_c \mathcal{C} \frac{i \left(\frac{2\delta}{\Gamma_m} - i\right)^{-1}}{1 - \mathcal{C} \left(\frac{2\delta}{\Gamma_m} - i\right)^{-1} \left(\frac{\kappa}{4\Omega_m} - i\right)^{-1}} \tag{B.46}$$

$$= 2\eta_c \mathcal{C} \frac{1}{\left(1 + i\frac{2\delta}{\Gamma_m}\right) - i\mathcal{C} \left(\frac{\kappa}{4\Omega_m} - i\right)^{-1}}. \tag{B.47}$$

Let us now rewrite the denominator of Eq. B.47 as

$$\left(1 + i\frac{2\delta}{\Gamma_m}\right) - i\mathcal{C} \frac{\frac{\kappa}{4\Omega_m} + i}{\left(\frac{\kappa}{4\Omega_m}\right)^2 + 1} \tag{B.48}$$

$$= \left(1 + \frac{\mathcal{C}}{1 + \left(\frac{\kappa}{4\Omega_m}\right)^2}\right) + i \left(\frac{2\delta}{\Gamma_m} - \frac{\mathcal{C}\frac{\kappa}{4\Omega_m}}{1 + \left(\frac{\kappa}{4\Omega_m}\right)^2}\right) \tag{B.49}$$

From Eqs.B.30 and B.31, with a red pump, we have

$$\frac{\delta\Omega_m}{\Gamma_m} = -\frac{1}{2}\frac{\mathcal{C}\left(\frac{\kappa}{4\Omega_m}\right)}{1+\left(\frac{\kappa}{4\Omega_m}\right)^2} \tag{B.50}$$

$$\frac{\Gamma_{opt}}{\Gamma_m} = \mathcal{C}\left(1-\frac{\left(\frac{\kappa}{4\Omega_m}\right)^2}{1+\left(\frac{\kappa}{4\Omega_m}\right)^2}\right) = \frac{\mathcal{C}}{1+\left(\frac{\kappa}{4\Omega_m}\right)^2}, \tag{B.51}$$

and we can rewrite Eq. B.49 as

$$\frac{\Gamma_m+\Gamma_{opt}}{\Gamma_m} + i\frac{2(\delta+\delta\Omega_m)}{\Gamma_m}. \tag{B.52}$$

Finally, we get

$$r_p(\delta) - r_d(\delta)|_{\mathcal{C}=0} = 2\eta_c\mathcal{C}\frac{\Gamma_m}{\Gamma_m+\Gamma_{opt}}\left(1+2i\frac{\delta+\delta\Omega_m}{\Gamma_m+\Gamma_{opt}}\right)^{-1}, \tag{B.53}$$

such that the mechanical EMIR feature appearing is a complex-valued Lorentzian where the mechanical frequency and linewidth have been modified by the light-induced spring and damping effects. Therefore EMIR can be used to measure DBA effects and characterise the light-mechanics interaction.

Appendix C

Samples Summary

In this Appendix, we summarise the flip-chip devices presented in this thesis. We report mechanical, microwave and electro-mechanical parameters.

C.1 Flipchip v2 - Dielectric Coupling

Dielectrically coupled un-metallised "dahlia" membrane, IDC on an H-antenna.

$$\begin{aligned} \omega_c/2\pi &= 4.495\,\mathrm{GHz} \\ Q_l = 410,\ Q_e &= 970,\ Q_i = 710 \\ \Omega_m/2\pi = 1.105\,\mathrm{MHz},\ Q_m &= 41\mathrm{M}\,(\text{at } 4\,\mathrm{K}) \\ g_0/2\pi &= 6\,\mathrm{mHz} \end{aligned} \tag{C.1}$$

C.2 Flipchip v6 - Double Defect Membrane

Double defect "dahlia" membrane with one metallised defect, over an LGR MW resonator: 15 nm of Al on 63 nm Si_3N_4.

$$\begin{aligned} \omega_c/2\pi &= 9.032\,\mathrm{GHz} \\ Q_l \sim Q_e &= 830 \\ \Omega_{m,E}/2\pi = 1.290\,\mathrm{MHz},\ Q_{m,E} &= 150\mathrm{M}(22\,\mathrm{mK}) \\ \Omega_{m,O}/2\pi = 1.324\,\mathrm{MHz},\ Q_{m,E} &= 9.1\mathrm{M}(\text{at } 4\,\mathrm{K}) \\ g_0/2\pi &= 26\,\mathrm{mHz} \end{aligned} \tag{C.2}$$

C.3 Flipchip v20 - Single Defect Membrane

Single defect "lotus" membrane with metallisation, over an LGR MW resonator: 20 nm of Al on ∼63 nm Si_3N_4.

$$\begin{aligned} \omega_c/2\pi &= 7.871\,\text{GHz} \\ Q_L = 1000,\ Q_e = 1300,\ Q_i &= 4700 \\ \Omega_m/2\pi = 1.487\,\text{MHz},\ Q_m &= (696 \pm 5)\text{M}\,(\text{at } 30\,\text{mK}) \\ g_0/2\pi &= 1.5\,\text{Hz} \end{aligned} \tag{C.3}$$

C.4 Flipchip v24 - Single Defect 20 nm Membrane

Single defect "lotus" membrane with metallisation, over an LGR MW resonator: 20 nm of Al on ∼20 nm Si_3N_4.

$$\begin{aligned} \omega_c/2\pi &= 8.976\,\text{GHz} \\ Q_l = 860,\ Q_e = 2200,\ Q_i &= 1400 \\ \Omega_m/2\pi = 1.408\,\text{MHz},\ Q_m &= 1.14\text{B}\,(\text{at } 30\,\text{mK}) \end{aligned} \tag{C.4}$$

C.5 Flipchip v26 - Highest Participation Ratio Flip-chip

Single defect "lotus" membrane with metallisation, over an LGR MW resonator: 20 nm of Al on ∼44 nm Si_3N_4.

$$\begin{aligned} \omega_c/2\pi &= 6.719\,\text{GHz} \\ Q_l = 880,\ Q_e = 1100,\ Q_i &= 4000 \\ \Omega_m/2\pi &= 1.492\,\text{MHz} \end{aligned} \tag{C.5}$$

Notice that all the above samples had very low microwave quality factors. For a long time, given our early attempts to fabricate an electromechanical system where the sample holding 3D box would be part of the MW circuit, the volume containing our LGR resonator flip-chips were large enough to host its own resonant mode at ∼8 GHz. The proximity of this spurious MW modes meant that our electromechanics cavity mode would couple to the very lossy 3D box mode giving low MW Q-factors. For

flipchipv27, we use a smaller volume sample holder without MW mode coupling leading to internal Q-factors in the 100k as is typical for superconducting microwave circuits.

C.6 Flipchip v27 - Ground State Cooling

Single defect "lotus" membrane with metallisation, over an LGR MW resonator: 50 nm of Al on ∼63 nm Si_3N_4.

$$\begin{aligned} \omega_c/2\pi &= 8.350\,\mathrm{GHz} \\ Q_l = 37000,\ Q_e = 46000,\ Q_i &= 192000 \\ \Omega_m/2\pi = 1.487\,\mathrm{MHz},\ Q_m &= 1.5\mathrm{B}\,(\mathrm{at}\ 30\,\mathrm{mK}) \\ g_0/2\pi &= (0.87 \pm 0.11)\,\mathrm{Hz} \end{aligned} \tag{C.6}$$

The high MW quality factors of flipchipv27 reveal power dependent internal loss attributable to MW TLS[Cap+20], thus we must keep track of the cavity lineshape at every data point.

Appendix D

Published Paper

In this appendix, we reproduce the main result from this research as published on the arXiv paper repository at https://arxiv.org/abs/2107.05552v2.

Notice that equation numbering, citations and page numbering are independent from the main text of this thesis.

arXiv:2107.05552v2 [quant-ph] 22 Jul 2021

Ground State Cooling of an Ultracoherent Electromechanical System

Yannick Seis [1,2], Thibault Capelle[1,2], Eric Langman[1,2], Sampo Saarinen[1,2], Eric Planz[1,2], and Albert Schliesser[1,2,*]

[1] *Niels Bohr Institute, University of Copenhagen, Blegdamsvej 17, 2100 Copenhagen, Denmark*
[2] *Center for Hybrid Quantum Networks (Hy-Q), Niels Bohr Institute, University of Copenhagen, Copenhagen, Denmark*
[*] *email: albert.schliesser@nbi.dk*

Abstract

Cavity electromechanics relies on parametric coupling between microwave and mechanical modes to manipulate the mechanical quantum state, and provide a coherent interface between different parts of hybrid quantum systems. High coherence of the mechanical mode is of key importance in such applications, in order to protect the quantum states it hosts from thermal decoherence. Here, we introduce an electromechanical system based around a soft-clamped mechanical resonator with an extremely high Q-factor ($> 10^9$) held at very low (30 mK) temperatures. This ultracoherent mechanical resonator is capacitively coupled to a microwave mode, strong enough to enable ground-state-cooling of the mechanics ($\bar{n}_{\mathrm{min}} = 0.76 \pm 0.16$). This paves the way towards exploiting the extremely long coherence times ($t_{\mathrm{coh}} > 100\,\mathrm{ms}$) offered by such systems for quantum information processing and state conversion.

1 Introduction

The field of cavity electromechanics [1, 2] investigates mechanical resonators which are parametrically coupled to radio-frequency or microwave circuits. Analogous to cavity optomechanics [3], this coupling is at the heart of a broad set of phenomena and techniques of interest in quantum science and technology. They range from ground-state cooling of the mechanics [4, 5, 6], via entanglement and squeezing [7, 8, 9, 10], to coherent microwave-optical [11, 12] (see also [13] and references therein) and superconducting qubit-mechanical interfaces [14, 15, 16, 17].

For most of these applications, a long *coherence time*

$$t_{\mathrm{coh}} = \frac{\hbar Q}{k_{\mathrm{B}} T} = \frac{1}{\bar{n}_{\mathrm{th}} \Gamma_{\mathrm{m}}}, \tag{1}$$

of the mechanical system is favourable. Here, $Q = \Omega_\mathrm{m}/\Gamma_\mathrm{m}$ is the mechanical quality factor defined as the ratio of the mechanical (angular) frequency Ω_m and its energy decay rate Γ_m; T the resonator temperature; $\hbar$ and k_B the reduced Planck and the Boltzmann constant, respectively; and $\bar{n}_\mathrm{th} \approx k_\mathrm{B}T/\hbar\Omega_\mathrm{m}$ is the equivalent occupation of the thermal bath. For state-of-the-art electromechanical systems with $Q \sim 10^5$ operated at milliKelvin temperatures, typical coherence times are in the range of 100 microseconds [14, 10].

On the other hand, recent progress in the design of mechanical systems has allowed reaching much higher quality factors in excess of 10^9 [18, 19, 20, 21, 22, 23]. At milliKelvin temperatures, such ultracoherent mechanical devices can reach $t_\mathrm{coh} > 100$ ms, some three orders of magnitude beyond the state-of-the-art (provided excess dephasing [21] is not an issue). However, so far, the mechanics' coupling to microwave modes has either been extremely weak [18], or absent because of lacking functionalization through e.g. metallization [19, 20, 22, 23]. For this reason, such mechanical systems could not yet be harnessed in electromechanics.

Here we demonstrate functionalization of an ultracoherent mechanical resonator based on a soft-clamped silicon nitride membrane [19] with a superconducting metal pad. This allows coupling it to a microwave resonator with sufficient strength to cool it to its quantum mechanical ground state. This implies that we have achieved a quantum cooperativity $C_\mathrm{q} > 1$ [3] and heralds the possibility to deploy ultracoherent mechanical resonators for applications in quantum electromechanics.

2 Results

2.1 Electromechanical system

The system studied here consists of a 63-nm thick soft-clamped membrane made of silicon nitride [19]. A square portion of its central defect (an area of approximately 60×60 $\mu\mathrm{m}^2$) is covered with a 50-nm thick layer of aluminum. This superconducting pad is placed, using a flip-chip assembly, closely above the capacitive electrodes of a planar loop gap resonator fabricated from a 100-nm thick layer of NbTiN, forming a resonant LC circuit (see Fig. 1A). The motion of the metalized membrane modulates the capacitance and in turn the resonance frequency of the microwave circuit, thereby forming a canonical electromechanical system [5, 11, 6]. The device is read out by inductive coupling to a coaxial transmission line and is placed on a mechanical damper, for vibration isolation [24], mounted on the mixing chamber plate of a dilution refrigerator (see Methods for details).

From microwave reflection measurements performed by the vector network analyser, we extract a cavity resonance frequency $\omega_\mathrm{c}/2\pi = 8.349\,\mathrm{GHz}$, a total linewidth $\kappa/2\pi = 240\,\mathrm{kHz}$ and an outcoupling efficency $\eta = \kappa_\mathrm{ex}/\kappa \sim 0.8$. With a mechanical mode at $\Omega_\mathrm{m}/2\pi = 1.486\,\mathrm{MHz}$, the system is well sideband-resolved ($\kappa \ll \Omega_\mathrm{m}$).

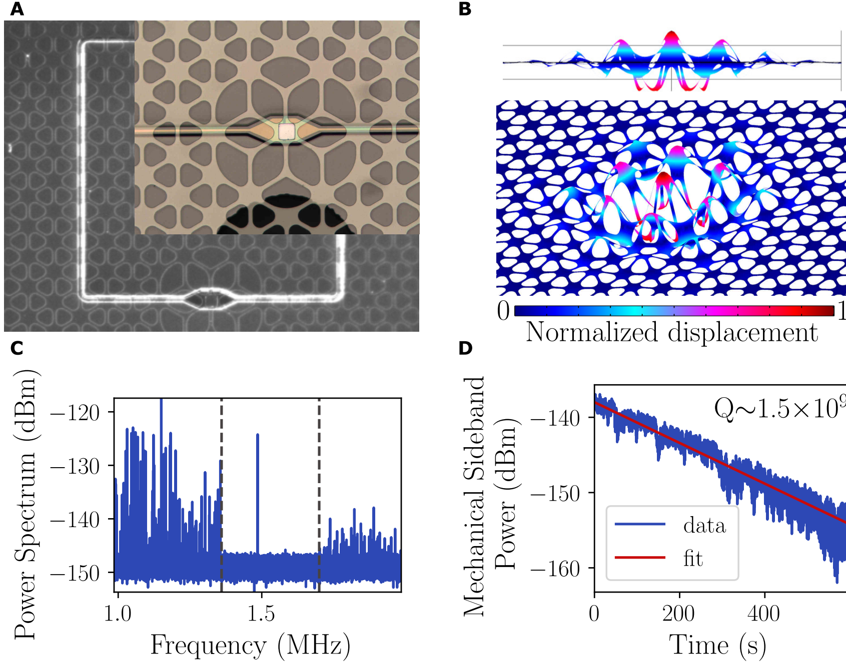

Figure 1: Electromechanical system. (A) The ultracoherent mechanical resonator is a thin Si_3N_4 patterned membrane integrated into a microwave 'loop-gap' resonator, with the mechanical motion modulating the resonator capacitance. (B) Simulated out-of-plane motion of the metalized defect mode. The displacement is localized, with largest amplitude at the metallization. (C) The measured mechanical spectrum shows a clean bandgap (whose limits appear as a dashed line) around the mode of interest (at ~ 1.5 MHz), resulting (D) in an ultra-high quality factor.

The soft-clamped membranes utilized in this work represent a new design of phononic membrane resonators, one which we find to have superior characteristics for electromechanical functionalization. Each membrane of this new design is referred to as a 'Lotus,' inspired by the resemblance of the defect-defining perforations to the large petals of various species of lotus flowers (Fig. 1A inset). Not only do we observe that Lotus-class designs possess larger bandgaps, they are capable of localizing a single out-of-plane mechanical mode centered in that enlarged bandgap, with maximum amplitude at the center of the defect (simulation in Fig. 1B). Importantly, this single mode remains well-isolated from the bandgap edges after aluminum metallization, as shown in Fig. 1C. Finally, we find such metallized lotuses are able to yield ultrahigh mechanical quality factors in excess of 10^9, as measured by energy ringdown (see Fig. 1D).

2.2 Calibrations

We establish the phonon occupation of the mechanical resonator via its equilibration to the controlled thermal bath provided in the cryostat. We drive the electromechanical system with a tone at frequency ω_p, red-detuned from the cavity resonance $\Delta \equiv \omega_\mathrm{p} - \omega_\mathrm{c} \approx -\Omega_\mathrm{m} < 0$ at a fixed, low power ($-45\,\mathrm{dBm}$ at the source) such that dynamical backaction [3] is negligible. Then, after further amplification and carrier cancellation (see Methods), we measure the spectral area occupied by the mechanical sideband (i.e. the total microwave power) around the frequency $\omega_\mathrm{p} + \Omega_\mathrm{m}$ for a range of sample temperatures as measured by the cryostat thermometer. At temperatures above $\sim$200 mK (see Fig. 2A), we observe a linear relationship between temperature and mechanical sideband area. This proportionality is interpreted as the sample being in a thermal equilibrium with the mixing chamber plate. Using Bose-Einstein statistics for thermal states $\bar{n}_\mathrm{th} = \frac{1}{e^{\hbar\Omega_\mathrm{m}/k_\mathrm{B}T} - 1}$, we extract a calibration constant between mechanical sideband area and mechanical occupation in quanta. At temperatures below $\sim$200 mK, dynamical backaction is small but nonnegligible ($\lesssim 15\%$). It has been corrected and is presented in Fig. 2A to show the thermalization of the mechanical oscillator to the base plate of the cryostat. At the lowest cryostat temperature of 30 mK, the mechanical mode thermalizes to $T_\mathrm{mode} \approx 80\,\mathrm{mK}$.

Next, we calibrate the dynamical backaction by performing mechanical ringdown measurements under red-detuned microwave drives with varying powers. Figure 2B shows superimposed ringdown sequences under increasing microwave power. For these measurements, we initialize the mechanics into a large coherent state by phase modulation of the red-detuned pump (duration 10 s), then amplify this coherent state by placing the pump on the blue side of the cavity (duration 1.75 s). Finally, we let the mechanics ring down for 600 s with the red-detuned microwave pump at power P varying from $-80\,\mathrm{dBm}$ to $-10\,\mathrm{dBm}$ (at the output of the signal generator). We fit the ringdowns to exponential decays where the time constants are the inverse angular decay rates Γ_eff^{-1}.

The resulting decay rates as function of pump power are shown in Fig. 2C, together with a fit using the model

$$\Gamma_\mathrm{eff}(P) = \Gamma_\mathrm{m} + \Gamma_\mathrm{e}(P) = \Gamma_\mathrm{m}\left(1 + \frac{P}{P_0}\right). \tag{2}$$

Here, Γ_m is the intrinsic loss rate of the mechanical resonator, while $\Gamma_\mathrm{e}(P)$ is the damping imparted by the dynamical backaction of the microwave mode [3]. We introduce P_0 as the power at which the pump-induced decay is equal to the intrinsic decay rate Γ_m. Note that P_0 depends on the cavity lineshape and the pump detuning from cavity resonance. At a cryostat temperature of 30 mK, we extract $\Gamma_\mathrm{m}/2\pi = 1.0\,\mathrm{mHz}$, a quality factor $Q_\mathrm{m} = \Omega_\mathrm{m}/\Gamma_\mathrm{m} = 1.5 \cdot 10^9$ and $P_0 = -38.7\,\mathrm{dBm}$ from the dataset shown in Fig. 2. We note that the quality factor is dependent on the sample temperature (see Methods section 4.4 for a systematic analysis). We perform our ground state cooling at the same temperature, allowing us to use the Γ_m and $\Gamma_\mathrm{e}(P)$ obtained from this fit as fixed parameters in all further analysis.

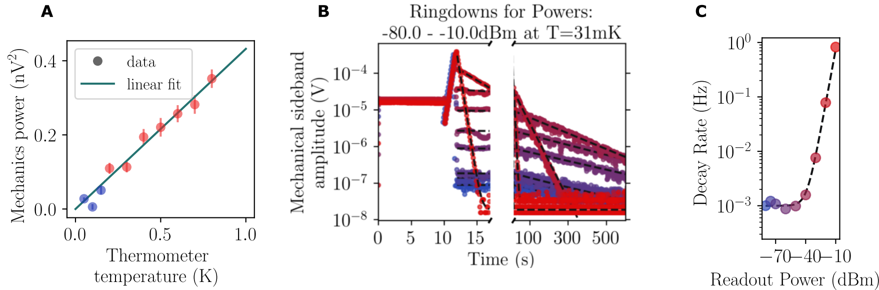

Figure 2: Electro-mechanical calibration: (A) The mechanical occupation is calibrated by thermal anchoring at temperatures above 200 mK. The linear relationship between the area of the mechanical peak in the spectrum and the sample holder temperature confirms the mechanics is thermalized. Only the red data are used for the fit (See main text) (B) A mechanical energy ringdown series measured as function of the applied cooling power, measured at 30 mK. Overlayed temporal series show repeatable initialization of the mechanical energy (up to ∼12 s) and increasing decay rates as the cooling power is turned up. (C) The fit of mechanical decay rates gives the intrinsic decay rate Γ_m, without dynamical backaction, and the corner power P_0, where the cooling rate $\Gamma_\mathrm{e}(P_0)$ is equal to Γ_m. Points' color code is the same as in panel B.

Finally, from a standard calibration technique detailed in Ref. [25], we extract a single-photon coupling rate $g_0/2\pi = (0.89 \pm 0.11)$ Hz.

2.3 Ground state cooling

To reduce the mechanical occupation of our mechanical resonator, we place a strong coherent pump on the red sideband of the microwave cavity ($\Delta = -\Omega_\mathrm{m}$), in the same experimental conditions with which we calibrated the phonon occupation (see Section 2.2).

In the resolved-sideband limit ($\kappa \ll \Omega_\mathrm{m}$), which we reach in this experiment, and close to the cavity frequency ($|\omega - \omega_\mathrm{c}| \ll \kappa$), the microwave power spectral density in units of noise quanta is then:

$$S[\omega] = n_\mathrm{add} + 4\eta\left(\tilde{n} + 1/2\right) + \eta\Gamma_\mathrm{m}\Gamma_\mathrm{e}\frac{\bar{n}_\mathrm{th} + \frac{1}{2} - \left(2 + \frac{\Gamma_\mathrm{e}}{\Gamma_\mathrm{m}}\right)\left(\tilde{n} + \frac{1}{2}\right)}{\left(\Gamma_\mathrm{m} + \Gamma_\mathrm{e}\right)^2/4 + \left(\omega - \omega_\mathrm{p} - \Omega_\mathrm{eff}\right)^2}, \quad (3)$$

where we have defined $\tilde{n} = \eta n_c + (1-\eta)\, n_0$, with $\eta = \kappa_\mathrm{c}/\kappa$, κ_c the coupling rate to the microwave cavity, n_c the microwave noise occupation coming from either the pump phase noise or the cavity frequency noise, n_0 the noise occupation of the microwave thermal environment (which is negligible in the considered experimental conditions). In the above expression, $\Omega_\mathrm{eff}/2\pi$ is the effective mechanical frequency including the frequency shift induced by the dynamical

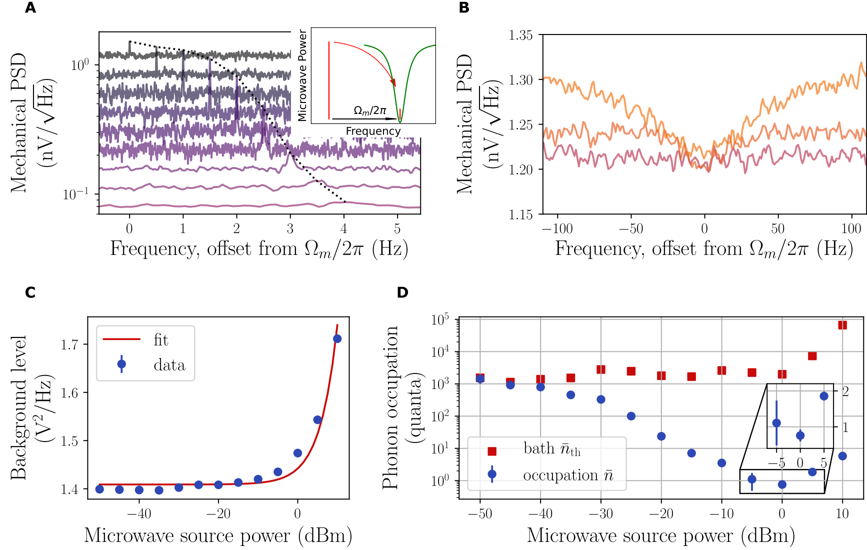

Figure 3: Sideband cooling of the mechanics to its motional ground state. (A) Mechanical power spectral density (PSD) around the defect mode as the cooling power is increased: the peak first increases in height with measurement gain, then visibly broadens as cooling takes place. Spectra are offset downwards and to the right in equal steps respectively as the power is increased. The dotted line is a guide to the eye for the location of the mechanical peaks. (B) At high pump powers, the cavity is populated due to the microwave phase noise: the noise occupancy is visible in the 'squashing' of the mechanical feature. (C) The increased background level of the mechanical spectrum allows to extract the cavity occupation $\tilde{n}$. (D) The mechanical occupation, calibrated in number of motional quanta, reaches below one phonon by dynamical backaction cooling before being heated up by cavity occupation due to source phase noise.

backaction. The measured microwave spectrum is composed of three parts: the background noise n_{add}, which is due to the HEMT amplifier, the microwave noise coming from the cavity, which is a Lorentzian whose width is the microwave loss rate κ, and the mechanical noise transduced into microwave noise *via* the electromechanical coupling. This mechanical feature is a Lorentzian of width $\Gamma_{\mathrm{eff}} = \Gamma_{\mathrm{m}} + \Gamma_{\mathrm{e}}$.

At low cooperativity $C \approx \Gamma_{\mathrm{e}}/\Gamma_{\mathrm{m}} \ll 1$, the signal, divided by the electromechanical gain $\eta\Gamma_{\mathrm{e}}/\Gamma_{\mathrm{m}}$ is simply a Lorentzian whose area is proportional to the mechanical bath occupation $\bar{n}_{\mathrm{th}} \gg \tilde{n}$. This is the regime where we performed the calibrations presented in section 2.2.

At a higher cooperativity $C \approx \Gamma_{\mathrm{e}}/\Gamma_{\mathrm{m}} \gg 1$, the rate at which phonons are extracted from the resonators initially exceeds the rate at which new phonons are entering the resonator *via* the mechanical thermal bath. A new equilibrium is

established at a reduced temperature of the mechanical resonator, corresponding to a reduced effective occupation $\bar{n} < \bar{n}_{\mathrm{th}}$. This appears as a decrease of the area under the mechanical spectrum.

At the highest cooperativities, the microwave noise starts to play a significant role. It originates either from the phase noise of the microwave source or from a cavity frequency noise. We see from equation (3) that the observed signal can then be a *negative* Lorentzian. This does not mean that the temperature of the mechanical mode is negative, but rather that the cross spectrum between the microwave noise in the cavity and the microwave noise transduced to mechanical noise changes the shape of the resulting signal [26]. In this case, inference of the mechanical mode temperature requires the knowledge of the phase noise, which is given by the background of the signal (for $\Gamma_{\mathrm{m}} + \Gamma_{\mathrm{e}} \ll |\omega - \omega_{\mathrm{c}}| \ll \kappa$)[27]:

$$S[\omega]_{\Gamma_{\mathrm{m}}+\Gamma_{\mathrm{e}} \ll |\omega-\omega_{\mathrm{c}}| \ll \kappa} = \mathcal{A} + \alpha P, \tag{4}$$

where P is the pump power, $\alpha P = 4\eta^2 n_c \approx 4\eta\tilde{n}$, and $\mathcal{A} = n_{\mathrm{add}} + 2\eta + 4\eta\,(1-\eta)\,n_0 \approx n_{\mathrm{add}}$. By fitting the model of Eq. (3) to the experimental spectra comprising both the mechanical feature and the background level, we obtain the parameters $\bar{n}_{\mathrm{th}}$ and $\tilde{n}$, respectively, at each power level (see Fig. 3). We can then compute the mechanical occupation as [5]:

$$\bar{n} = \frac{\Gamma_{\mathrm{m}}}{\Gamma_{\mathrm{m}} + \Gamma_{\mathrm{e}}}\bar{n}_{\mathrm{th}} + \frac{\Gamma_{\mathrm{e}}}{\Gamma_{\mathrm{m}} + \Gamma_{\mathrm{e}}}\tilde{n}. \tag{5}$$

The minimum inferred occupation is $\bar{n}_{\mathrm{min}} = 0.76 \pm 0.16$. This final value is limited by the efficiency of the vibration isolation, which increases the mechanical bath temperature above the thermodynamic temperature (see Methods), and the microwave phase noise at the input of the system. Although an increase of the mechanical bath temperature can be observed for pump powers ≥ 0 dBm, the contribution of the phase noise is still dominant. Placing a microwave cavity filter at the output of the signal generator, absorbing pump phase noise around the electromechanical cavity resonance, did not improve the result. This suggests that the phase noise is limited by cavity noise rather than the phase noise of the microwave source.

3 Discussion

The mechanical occupation calibrated in Fig. 2A along with the measured intrinsic mechanical decay rate furthermore allow us to estimate the mechanics' quantum coherence time. Following eq. (1), we extract $t_{\mathrm{coh}} \approx 140\,\mathrm{ms}$. This is three orders of magnitude larger than for state-of-the-art electromechanical systems [14, 10]. However, further work will be needed to fully confirm the coherence of the mechanical system, ruling out e. g. excess decoherence by dephasing [21].

At the highest input powers ($P = 10\,\mathrm{dBm}$), we achieve a cooperativity $C = \mathcal{O}(10^5)$ and an electromechanical damping on the order of $\Gamma_{\mathrm{e}}/2\pi \sim 80\,\mathrm{Hz}$.

However, we estimate that the single-photon coupling rate g_0 might be increased by an order of magnitude by adjustment of the geometry, in particular the gap between the membrane electrode and its counterelectrodes. This would immediately boost the coupling (with $\Gamma_\mathrm{e} \propto g_0^2$) and simultaneously alleviate the issues with microwave phase noise. Indeed, $g_0/2\pi = 7\,\mathrm{Hz}$ and coupling rates well above 100 kHz have been demonstrated in a similar system [6].

Potential applications of the platform introduced here include quantum memories for microwave quantum states [28], where they could replace or supplement less coherent ($t_\mathrm{coh}^\mathrm{MW} \sim 10\,\mathrm{ms}$), much more bulky microwave resonators [29]. By combining this with an *opto*-mechanical interface [20], e. g. by introducing a second defect in the phononic crystal [30], such systems could form part of an electro-opto-mechanical transducer [11, 12]. One of its key figures of merit, namely the number of added noise quanta, falls proportionally with the coherence time of the mechanics [31]. Furthermore, the high mechanical coherence immediately translates to an outstanding force sensitivity. This allows for the microwave mode to be used as a sensitive transducer for the motion induced by the physical system of interest, which could be anything from spins [32, 33, 34] to dark matter [35]. Nominally, the resonant force noise spectral density of the presented device is $S_{FF}^{1/2} = (2m\Gamma_\mathrm{m}k_\mathrm{B}T)^{1/2} \approx 650\,\mathrm{zN/Hz^{1/2}}$, assuming the mode mass of ~15 ng estimated by COMSOL simulations. Finally, the mere observation of excessively long coherence times may be used to constrain models on spontaneous collapse of the mechanical wave function [36].

4 Methods

4.1 Sample fabrication

The planar microwave resonator is a patterned thin film of NbTiN sputter-deposited by Star Cryoelectronics on a high-resistivity silicon wafer from Topsil. The superconductor is patterned with standard UV lithography and etched with an ICP recipe based on SF_6/O_2 at low power to avoid resist burning. Aluminum pillars define the flip-chip nominal separation, and we etch a recess into the resonator Si chip using the Bosch process to minimise the risk of the flip-chip contacting anywhere else than at the pillars.

The membrane is made of stoichiometric high-stress silicon nitride patterned with standard UV lithography and etched with a CF_4/H_2-based ICP recipe on wafer front and back side. The membrane is released in a hot KOH bath. The membranes are then cleaned in a bath of piranha solution, broken off to individual chips and metallized by shadow-masked e-beam evaporation of aluminum.

4.2 Sample mounting

The flip-chip assembly is placed inside a gold-coated oxygen-free high-conductivity (OFHC) copper holder and mounted on the mechanical damper. The 'mass-on-a-spring' mechanical damper is composed of a thick ~1.4 kg OFHC copper block

suspended from steel springs mounted onto the MXC plate (See Fig. 4A). The copper block and the springs are well thermalized by copper braids and allow for the device to be cooled to ∼30 mK.

4.3 Sample measurement

The sample is initially characterized by cavity reflection and electromechanically-inducted transparency measurements to establish microwave and mechanical resonance frequencies with the vector network analyser (Rohde & Schwarz ZNB20) and a pump tone supplied by a low-noise signal generator (R&S SMA100B). Mechanical ringdowns and spectra for calibration and ground-state cooling are then measured by sending a tone from the signal generator onto the device and analysing the fields exiting the cavity using the IQ module of a spectrum analyser (R&S FSW26). In order to prevent the spectrum analyser's phase noise from effecting the measured signal, we interferometrically cancel the carrier of the field before its analysis.

4.4 Investigation of mechanical damping

We plot in Fig. 4B the intrinsic mechanical damping rate Γ_m as function of temperature, as read from the thermometer placed on the MXC plate. Note that these data were taken in a different, earlier thermal cycle than those presented in the main text. The intrinsic damping follows a power law of temperature with exponent equal to 0.63, indicating two-level systems in the material being the dominant loss channel [37]. The power law fits the data from 1.5 K to 30 mK, giving us confidence that the material is well-thermalized to the MXC plate. We thus attribute any mechanical bath temperature that is higher than the measured thermometer temperature (as for the data presented in Fig. 3) to be caused by excess vibrational noise due to the dilution refrigerator's cooling system (for example the pulse tube). The later data set presented in Fig. 1D and Fig. 2B and C have slightly higher quality factors than in Fig. 4B, showing that thermal cycling and longer cryogenic operation may improve the mechanical quality of our devices.

Acknowledgements

This work was supported by the European Research Council project Q-CEOM (grant no. 638765), the Danish National Research Foundation (Center of Excellence "Hy-Q"), the EU H2020 FET proactive project HOT (grant no. 732894), as well as the Swiss National Science Foundation (grant no. 177198). The project has furthermore received funding from the European Union's Horizon 2020 research and innovation program under grant agreement No. 722923 (Marie Curie ETN - OMT) and the Marie Skłodowska-Curie grant agreement No 801199S.

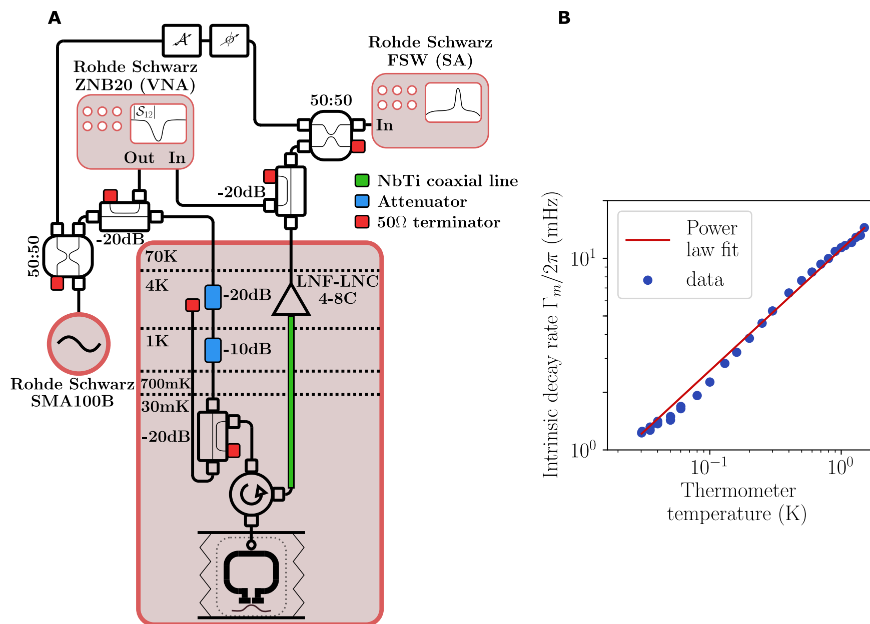

Figure 4: Experimental setup. (A) Setup of the electromechanical device (bottom) attached to the mixing chamber plate of a dilution refrigerator. It is driven by a highly pure microwave tone, attenuated to eliminate room temperature thermal noise. The returned microwave radiation is detected with a vector network analyzer (VNA) and, after interferometric cancellation of the carrier, a spectrum analyzer (SA). (B) The mechanical decay rate follows a power law as function of sample temperature, indicating the dominant loss channel to be related to mechanical two-level systems (TLS) in the material.

Author Contributions

Y. S. designed and fabricated the microwave circuit and flip-chip assembly, performed most of the experiments and analyzed the data. T. C. designed the mechanical isolator, participated in data acquisition and analysis and made the theoretical model. E. L. designed and fabricated the metallized phononic membrane resonator. S. S. and E. P. contributed to the experimental setup and characterisation at an early stage. Y. S., T. C. and A. S. wrote the manuscript, which all authors revised. A. S. supervised the entire project.

Competing interests

The authors declare no competing interests.

Data availability

The data that support the findings of this study are available from the corresponding author upon reasonable request. Source data representing all the data in the published figures are provided with this paper.

References

[1] Konrad W. Lehnert. Introduction to Microwave Cavity Optomechanics. In M. Aspelmeyer, T. J. Kippenberg, and F. Marquardt, editors, *Cavity Optomechanics: Nano- and Micromechanical Resonators Interacting with Light*, Quantum Science and Technology, pages 233–252. Springer, Berlin, Heidelberg, 2014.

[2] A. A. Clerk, K. W. Lehnert, P. Bertet, J. R. Petta, and Y. Nakamura. Hybrid quantum systems with circuit quantum electrodynamics. *Nature Physics*, 16(3):257–267, 2020.

[3] M. Aspelmeyer, T. J. Kippenberg, and F. Marquardt. Cavity optomechanics. *Rev. Mod. Phys.*, 86(4):1391–1452, 2014.

[4] J. D. Teufel, T. Donner, Dale Li, J. W. Harlow, M. S. Allman, K. Cicak, A. J. Sirois, J. D. Whittaker, K. W. Lehnert, and R. W. Simmonds. Sideband cooling of micromechanical motion to the quantum ground state. *Nature*, pages 359, 363, 2011.

[5] M. Yuan, V. Singh, Y. M. Blanter, and G. A. Steele. Large cooperativity and microkelvin cooling with a three-dimensional optomechanical cavity. *Nature Communications*, 6:8491, 2015.

[6] A. Noguchi, R. Yamazaki, M. Ataka, H. Fujita, Y. Tabuchi, T. Ishikawa, K. Usami, and Y. Nakamura. Ground state cooling of a quantum electromechanical system with a silicon nitride membrane in a 3D loop-gap cavity. *New Journal of Physics*, 18(10):103036, 2016.

[7] T. A. Palomaki, J. D. Teufel, R. W. Simmonds, and K. W. Lehnert. Entangling Mechanical Motion with Microwave Fields. *Science*, 342(6159):710–713, 2013.

[8] E. E. Wollman, C. U. Lei, A. J. Weinstein, J. Suh, A. Kronwald, F. Marquardt, A. A. Clerk, and K. C. Schwab. Quantum squeezing of motion in a mechanical resonator. *Science*, 349(6251):952–955, 2015.

[9] C. F. Ockeloen-Korppi, E. Damskägg, J.-M. Pirkkalainen, M. Asjad, A. A. Clerk, F. Massel, M. J. Woolley, and M. A. Sillanpää. Stabilized entanglement of massive mechanical oscillators. *Nature*, 556(7702):478–482, 2018.

[10] R. D. Delaney, A. P. Reed, R. W. Andrews, and K. W. Lehnert. Measurement of motion beyond the quantum limit by transient amplification. *PRL*, 123(18):183603, 2019.

[11] R. W. Andrews, R. W. Peterson, T. P. Purdy, K. Cicak, R. W. Simmonds, C. A. Regal, and K. W. Lehnert. Reversible and efficient conversion between microwave and optical light. *Nature Physics*, 10:321, 2014.

[12] T. Bagci, A. Simonsen, S. Schmid, L. G. Villanueva, E. Zeuthen, J. Appel, J. M. Taylor, A. Sø rensen, K. Usami, A. Schliesser, and E. S. Polzik. Optical detection of radio waves through a nanomechanical transducer. *Nature*, 507:81, 2014.

[13] L. Midolo, A. Schliesser, and A. Fiore. Nano-opto-electro-mechanical systems. *Nature Nanotechnology*, 13(1):11–18, 2018.

[14] Y. Chu, P. Kharel, W. H. Renninger, L. D. Burkhart, L. Frunzio, P. T. Rakich, and R. J. Schoelkopf. Quantum acoustics with superconducting qubits. *Science*, 358(6360):199–202, 2017.

[15] P. Arrangoiz-Arriola, E. A. Wollack, Z. Wang, M. Pechal, W. Jiang, T. P. McKenna, J. D. Witmer, R. Laer, and A. H. Safavi-Naeini. Resolving the energy levels of a nanomechanical oscillator. *Nature*, 571(7766):537–540, 2019.

[16] A. Bienfait, K. J. Satzinger, Y. P. Zhong, H.-S. Chang, M.-H. Chou, C. R. Conner, É Dumur, J. Grebel, G. A. Peairs, R. G. Povey, and A. N. Cleland. Phonon-mediated quantum state transfer and remote qubit entanglement. *Science*, 364(6438):368–371, 2019.

[17] M. Mirhosseini, A. Sipahigil, M. Kalaee, and O. Painter. Superconducting qubit to optical photon transduction. *Nature*, 588(7839):599–603, 2020.

[18] M. Goryachev, D. L. Creedon, E. N. Ivanov, S. Galliou, R. Bourquin, and M. E. Tobar. Extremely high q-factor mechanical modes in quartz bulk acoustic wave resonators at millikelvin temperature. *AIP Conference Proceedings*, 1633(1):90–92, 2014.

[19] Y. Tsaturyan, A. Barg, E. S. Polzik, and A. Schliesser. Ultracoherent nanomechanical resonators via soft clamping and dissipation dilution. *Nature Nanotechnology*, 12(8):776–783, 2017.

[20] M. Rossi, D. Mason, J. Chen, Y. Tsaturyan, and A. Schliesser. Measurement-based quantum control of mechanical motion. *Nature*, 563(7729):53–58, 2018.

[21] G. S. MacCabe, H. Ren, J. Luo, J. D. Cohen, H. Zhou, A. Sipahigil, M. Mirhosseini, and O. Painter. Nano-acoustic resonator with ultralong phonon lifetime. *Science*, 370(6518):840–843, 2020.

[22] A. Beccari, D. A. Visani, S. A. Fedorov, M. J. Bereyhi, V. Boureau, N. J. Engelsen, and T. J. Kippenberg. Strained crystalline nanomechanical resonators with ultralow dissipation. *arXiv:2107.02124 [cond-mat, physics:quant-ph]*, 2021.

[23] A. Beccari, M. J. Bereyhi, R. Groth, S. A. Fedorov, A. Arabmoheghi, N. J. Engelsen, and T. J. Kippenberg. Hierarchical tensile structures with ultralow mechanical dissipation. *arXiv:2103.09785 [cond-mat, physics:physics, physics:quant-ph]*, 2021. arXiv: 2103.09785.

[24] M. de Wit, G. Welker, K. Heeck, F. M. Buters, H. J. Eerkens, G. Koning, H. van der Meer, D. Bouwmeester, and T. H. Oosterkamp. Vibration isolation with high thermal conductance for a cryogen-free dilution refrigerator. *Review of Scientific Instruments*, 90(1):015112, 2019.

[25] M. L. Gorodetksy, A. Schliesser, G. Anetsberger, S. Deleglise, and T. J. Kippenberg. Determination of the vacuum optomechanical coupling rate using frequency noise calibration. *Opt. Express*, 18(22):23236–23246, 2010.

[26] A. J. Weinstein, C. U. Lei, E. E. Wollman, J. Suh, A. Metelmann, A. A. Clerk, and K. C. Schwab. Observation and interpretation of motional sideband asymmetry in a quantum electromechanical device. *PRX*, 4(4):041003, 2014.

[27] A. H. Safavi-Naeini, J. Chan, J. T. Hill, S. Gröblacher, H. Miao, Y. Chen, M. Aspelmeyer, and O. Painter. Laser noise in cavity-optomechanical cooling and thermometry. *New Journal of Physics*, 15(3):035007, 2013.

[28] T. A. Palomaki, J. W. Harlow, J. D. Teufel, R. W. Simmonds, and K. W. Lehnert. Coherent state transfer between itinerant microwave fields and a mechanical oscillator. *Nature*, 495(7440):210–214, 2013.

[29] M. Reagor, H Paik, G. Catelani, L. Sun, C. Axline, E. Holland, I. M. Pop, N. A. Masluk, T. Brecht, L. Frunzio, M. H. Devoret, Glazman L., and R. J. Schoelkopf. Reaching 10 ms single photon lifetimes for superconducting aluminum cavities. *Applied Physics Letters*, 102(19):192604, 2013.

[30] L. Catalini, Y. Tsaturyan, and A. Schliesser. Soft-Clamped Phononic Dimers for Mechanical Sensing and Transduction. *Physical Review Applied*, 14(1):014041, 2020. Publisher: American Physical Society.

[31] E. Zeuthen, A. Schliesser, A. S. Sø rensen, and J. M. Taylor. Figures of merit for quantum transducers. *Quantum Science and Technology*, 5(3):034009, 2020.

[32] R. Fischer, D. P. McNally, C. Reetz, G. G. T. Assumpção, T. Knief, Y. Lin, and C. A. Regal. Spin detection with a micromechanical trampoline: towards magnetic resonance microscopy harnessing cavity optomechanics. *New Journal of Physics*, 21(4):043049, 2019.

[33] J. KoŠata, O. Zilberberg, C. L. Degen, R. Chitra, and A. Eichler. Spin Detection via Parametric Frequency Conversion in a Membrane Resonator. *Physical Review Applied*, 14(1):014042, 2020. Publisher: American Physical Society.

[34] D. Hälg, T. Gisler, Y. Tsaturyan, L. Catalini, U. Grob, M.-D. Krass, M. Héritier, H. Mattiat, A.-K. Thamm, R. Schirhagl, E. C. Langman, A. Schliesser, C. L. Degen, and A. Eichler. Membrane-Based Scanning Force Microscopy. *Physical Review Applied*, 15(2):L021001, 2021. Publisher: American Physical Society.

[35] D. Carney, G. Krnjaic, D. C. Moore, C. A. Regal, G. Afek, S. Bhave, B. Brubaker, T. Corbitt, J. Cripe, N. Crisosto, A. Geraci, S. Ghosh, J. G. E. Harris, A. Hook, E. W. Kolb, J. Kunjummen, R. F. Lang, T. Li, T. Lin, Z. Liu, J. Lykken, L. Magrini, J. Manley, N. Matsumoto, A. Monte, F. Monteiro, T. Purdy, C. J. Riedel, R. Singh, S. Singh, K. Sinha, J. M. Taylor, J. Qin, D. J. Wilson, and Y. Zhao. Mechanical quantum sensing in the search for dark matter. *Quantum Science and Technology*, 6(2):024002, 2021. Publisher: IOP Publishing.

[36] S. Nimmrichter, K. Hornberger, and K. Hammerer. Optomechanical Sensing of Spontaneous Wave-Function Collapse. *Physical Review Letters*, 113(2):020405, 2014.

[37] X. Zhou, D. Cattiaux, R. R. Gazizulin, A. Luck, O. Maillet, T. Crozes, J.-F. Motte, O. Bourgeois, A. Fefferman, and E. Collin. On-chip thermometry for microwave optomechanics implemented in a nuclear demagnetization cryostat. *Phys. Rev. Applied*, 12(4):044066, 2019.

Bibliography

[Abb+16] B. P. Abbott et al. "Observation of Gravitational Waves from a Binary Black Hole Merger". In: *Phys. Rev. Lett.* 116 (6 Feb. 2016), p. 061102. DOI: 10.1103/PhysRevLett.116.061102 (cit. on p. 1).

[AH10] G. S. Agarwal and S. Huang. "Electromagnetically induced transparency in mechanical effects of light". In: *Phys. Rev. A* 81.4 (Apr. 2010), p. 041803. DOI: 10.1103/PhysRevA.81.041803 (cit. on p. 25).

[And+14] R. W. Andrews et al. "Bidirectional and efficient conversion between microwave and optical light". In: *Nature Physics* 10 (Mar. 2014), p. 321. DOI: 10.1038/nphys2911 (cit. on pp. 3, 20, 84).

[And15] R. W. Andrews. "Quantum Signal Processing with Mechanical Oscillators". Sec. 3.3. PhD thesis. University of Boulder, Colorado, 2015. URL: https://scholar.colorado.edu/phys_gradetds/143 (cit. on p. 15).

[Ans+20] F. Ansaloni et al. "Single-electron operations in a foundry-fabricated array of quantum dots". In: *Nature Communications* 11.1 (Dec. 2020), p. 6399. ISSN: 2041-1723. DOI: 10.1038/s41467-020-20280-3 (cit. on p. 2).

[AKM14] M. Aspelmeyer, T. J. Kippenberg, and F. Marquardt. "Cavity optomechanics". In: *Rev. Mod. Phys.* 86 (4 Dec. 2014), pp. 1391–1452. DOI: 10.1103/RevModPhys.86.1391 (cit. on pp. 7, 18, 89).

[Bag+14] T. Bagci et al. "Optical detection of radio waves through a nanomechanical transducer". In: *Nature* 507 (Mar. 2014), p. 81. DOI: 10.1038/nature13029 (cit. on pp. 3, 20, 84).

[BMS16] A. Z. Barasheed, T. Müller, and J. C. Sankey. "Optically defined mechanical geometry". In: *Phys. Rev. A* 93.5 (May 2016), p. 053811. DOI: 10.1103/PhysRevA.93.053811 (cit. on p. 2).

[Bar+08] R. Barends et al. "Contribution of dielectrics to frequency and noise of NbTiN superconducting resonators". In: *Applied Physics Letters* 92.22 (2008), p. 223502. DOI: 10.1063/1.2937837. eprint: https://doi.org/10.1063/1.2937837 (cit. on pp. 30, 56, 84).

[Bar+16] A. Barg et al. "Measuring and imaging nanomechanical motion with laser light". In: *Applied Physics B* 123.1 (Dec. 2016), p. 8. ISSN: 1432-0649. URL: https://doi.org/10.1007/s00340-016-6585-7 (cit. on p. 69).

[Ber19] N. R. Bernier. "Multimode microwave circuit optomechanics as a platform to study coupled quantum harmonic oscillators". PhD thesis. EPFL, 2019 (cit. on p. 54).

[BM67] V. B. Braginskiĭ and A. B. Manukin. "Ponderomotive Effects of Electromagnetic Radiation". In: *Soviet Journal of Experimental and Theoretical Physics* 25 (Oct. 1967), p. 653. ISSN: 1063-7761. URL: https://ui.adsabs.harvard.edu/abs/1967JETP...25..653B (cit. on p. 1).

[BMT70] V. B. Braginskiĭ, A. B. Manukin, and M. Y. Tikhonov. "Investigation of Dissipative Ponderomotive Effects of Electromagnetic Radiation". In: *Soviet Journal of Experimental and Theoretical Physics* 31 (Jan. 1970), p. 829. ISSN: 1063-7761. URL: https://ui.adsabs.harvard.edu/abs/1970JETP...31..829B (cit. on p. 1).

[Bru+15] A. Bruno et al. "Reducing intrinsic loss in superconducting resonators by surface treatment and deep etching of silicon substrates". In: *Applied Physics Letters* 106.18 (2015), p. 182601. DOI: 10.1063/1.4919761. eprint: https://doi.org/10.1063/1.4919761 (cit. on p. 30).

[Cap20] T. Capelle. "Electromechanical cooling and parametric amplification of an ultrahigh-Q mechanical oscillator". PhD thesis. Sorbonne Université, 2020 (cit. on pp. 15, 61).

[Cap+20] T. Capelle et al. "Probing a Two-Level System Bath via the Frequency Shift of an Off-Resonantly Driven Cavity". In: *Phys. Rev. Applied* 13.3 (Mar. 2020), p. 034022. DOI: 10.1103/PhysRevApplied.13.034022 (cit. on pp. 32, 69, 101).

[CTS20] L. Catalini, Y. Tsaturyan, and A. Schliesser. "Soft-clamped phononic dimers for mechanical sensing and transduction". In: *arxiv* (Mar. 9, 2020). arXiv: 2003.04072v1 [physics.app-ph] (cit. on p. 20).

[Cav80] C. M. Caves. "Quantum-Mechanical Radiation-Pressure Fluctuations in an Interferometer". In: *Phys. Rev. Lett.* 45.2 (July 1980), pp. 75–79. URL: https://link.aps.org/doi/10.1103/PhysRevLett.45.75 (cit. on p. 1).

[Cha+21] S. Chakram et al. "Seamless High-Q Microwave Cavities for Multimode Circuit Quantum Electrodynamics". In: *Phys. Rev. Lett.* 127.10 (Aug. 2021), p. 107701. DOI: 10.1103/PhysRevLett.127.107701 (cit. on p. 2).

[Cha+11] J. Chan et al. "Laser cooling of a nanomechanical oscillator into its quantum ground state". In: *Nature* 478.7367 (Oct. 2011), pp. 89–92. ISSN: 1476-4687. DOI: 10.1038/nature10461 (cit. on p. 2).

[Che+20] J. Chen et al. "Entanglement of propagating optical modes via a mechanical interface". In: *Nature Communications* 11.1 (Feb. 2020), p. 943. ISSN: 2041-1723. DOI: 10.1038/s41467-020-14768-1 (cit. on p. 84).

[Cle+10] A. A. Clerk et al. "Introduction to quantum noise, measurement, and amplification". In: *Rev. Mod. Phys.* 82.2 (Apr. 2010), pp. 1155–1208. DOI: 10.1103/RevModPhys.82.1155 (cit. on p. 9).

[CHP99] P. F. Cohadon, A. Heidmann, and M. Pinard. "Cooling of a Mirror by Radiation Pressure". In: *Phys. Rev. Lett.* 83.16 (Oct. 1999), pp. 3174–3177. DOI: 10.1103/PhysRevLett.83.3174 (cit. on p. 2).

[Coh+20] M. A. Cohen et al. "Optomechanical Microwave Amplification without Mechanical Amplification". In: *Phys. Rev. Applied* 13.1 (Jan. 2020), p. 014028. DOI: 10.1103/PhysRevApplied.13.014028 (cit. on p. 25).

[Col+11] G. D. Cole et al. "Phonon-tunnelling dissipation in mechanical resonators". In: *Nature Communications* 2.1 (Mar. 2011), p. 231. ISSN: 2041-1723. DOI: 10.1038/ncomms1212 (cit. on p. 64).

[Dra14] A. Drachmann. “Proximitizing InAs 2DEG with NbTi through Epitaxial Aluminum”. MA thesis. University of Copenhagen, 2014 (cit. on p. 29).

[EP18] C. Eichler and J. R. Petta. “Realizing a Circuit Analog of an Optomechanical System with Longitudinally Coupled Superconducting Resonators”. In: *Phys. Rev. Lett.* 120.22 (May 2018), p. 227702. DOI: 10.1103/physrevlett.120.227702 (cit. on p. 22).

[Fau+12] T. Faust et al. “Microwave cavity-enhanced transduction for plug and play nanomechanics at room temperature”. In: *Nature Communications* 3.1 (Mar. 2012), p. 728. ISSN: 2041-1723. DOI: 10.1038/ncomms1723 (cit. on p. 15).

[Fis+16] R. Fischer et al. “Optical probing of mechanical loss of a Si_3N_4 membrane below 100 mK”. In: *arxiv* (Nov. 3, 2016). arXiv: 1611.00878v1 [cond-mat.mes-hall] (cit. on pp. 69, 86).

[Fis+19] R. Fischer et al. “Spin detection with a micromechanical trampoline: towards magnetic resonance microscopy harnessing cavity optomechanics”. In: *New Journal of Physics* 21.4 (Apr. 2019), p. 043049. ISSN: 1367-2630. DOI: 10.1088/1367-2630/ab117a (cit. on p. 20).

[FJ+12] N. E. Flowers-Jacobs et al. “Fiber-cavity-based optomechanical device”. In: *Appl. Phys. Lett.* 101.22 (Nov. 2012), p. 221109. ISSN: 0003-6951. DOI: 10.1063/1.4768779 (cit. on p. 2).

[Fog+19] F. Fogliano et al. “Cavity nano-optomechanics in the ultrastrong coupling regime with ultrasensitive force sensors”. In: *arxiv* (Apr. 1, 2019). arXiv: 1904.01140v1 [quant-ph] (cit. on p. 23).

[Gee+12] K. Geerlings et al. “Improving the quality factor of microwave compact resonators by optimizing their geometrical parameters”. In: *Appl. Phys. Lett.* 100.19 (May 2012), p. 192601. ISSN: 0003-6951. DOI: 10.1063/1.4710520 (cit. on p. 9).

[Gel+19] M. F. Gely et al. “Observation and stabilization of photonic Fock states in a hot radio-frequency resonator”. In: *Science* 363.6431 (Mar. 2019), p. 1072. DOI: 10.1126/science.aaw3101 (cit. on p. 22).

[Gha+18] A. H. Ghadimi et al. "Elastic strain engineering for ultralow mechanical dissipation". In: *Science* 360.6390 (May 2018), p. 764. URL: http://science.sciencemag.org/content/360/6390/764.abstract (cit. on pp. 2, 18).

[Gor+10] M. L. Gorodetksy et al. "Determination of the vacuum optomechanical coupling rate using frequency noise calibration". In: *Opt. Express* 18.22 (Oct. 2010), pp. 23236–23246. DOI: 10.1364/oe.18.023236. URL: http://www.opticsexpress.org/abstract.cfm?URI=oe-18-22-23236 (cit. on p. 66).

[Han+20] X. Han et al. "Cavity piezo-mechanics for superconducting-nanophotonic quantum interface". In: *Nature Communications* 11.1 (June 2020), p. 3237. ISSN: 2041-1723. DOI: 10.1038/s41467-020-17053-3 (cit. on p. 3).

[HBY19] D. Hatanaka, A. Bachtold, and H. Yamaguchi. "Electrostatically Induced Phononic Crystal". In: *Phys. Rev. Applied* 11.2 (Feb. 2019), p. 024024. DOI: 10.1103/PhysRevApplied.11.024024 (cit. on p. 2).

[Hea+20] W. Hease et al. "Bidirectional Electro-Optic Wavelength Conversion in the Quantum Ground State". In: *PRX Quantum* 1.2 (Nov. 2020), p. 020315. DOI: 10.1103/PRXQuantum.1.020315 (cit. on pp. 3, 85).

[Hei+14] T. T. Heikkilä et al. "Enhancing Optomechanical Coupling via the Josephson Effect". In: *Phys. Rev. Lett.* 112.20 (May 2014), p. 203603. DOI: 10.1103/PhysRevLett.112.203603 (cit. on p. 15).

[Hen+12] D. Henrich et al. "Geometry-induced reduction of the critical current in superconducting nanowires". In: *Phys. Rev. B* 86.14 (Oct. 2012), p. 144504. DOI: 10.1103/PhysRevB.86.144504 (cit. on p. 33).

[Hig+18] A. P. Higginbotham et al. "Harnessing electro-optic correlations in an efficient mechanical converter". In: *Nature Physics* 14.10 (Oct. 2018), pp. 1038–1042. ISSN: 1745-2481. DOI: 10.1038/s41567-018-0210-0 (cit. on pp. 15, 20, 25, 85).

[Hol+20] J. Holzgrafe et al. "Cavity electro-optics in thin-film lithium niobate for efficient microwave-to-optical transduction". In: *arxiv* (May 2, 2020). arXiv: 2005.00939v2 [quant-ph] (cit. on p. 3).

[Hor+12] H. L. Hortensius et al. “Critical-current reduction in thin superconducting wires due to current crowding”. In: *Appl. Phys. Lett.* 100.18 (Apr. 2012), p. 182602. ISSN: 0003-6951. DOI: 10.1063/1.4711217. URL: https://doi.org/10.1063/1.4711217 (cit. on p. 33).

[ID04] R. Igreja and C. Dias. “Analytical evaluation of the interdigital electrodes capacitance for a multi-layered structure”. In: *Sensors and Actuators A: Physical* 112.2 (2004), pp. 291 –301. ISSN: 0924-4247. DOI: 10.1016/j.sna.2004.01.040. URL: http://www.sciencedirect.com/science/article/pii/S0924424704000779 (cit. on p. 30).

[Jan+17] E. Janitz et al. “High mechanical bandwidth fiber-coupled Fabry-Perot cavity”. In: *Opt. Express* 25.17 (Aug. 2017), pp. 20932–20943. URL: http://www.osapublishing.org/oe/abstract.cfm?URI=oe-25-17-20932 (cit. on p. 2).

[Jos62] B. D. Josephson. “Possible new effects in superconductive tunnelling”. In: *Physics Letters* 1.7 (July 1962), pp. 251–253. ISSN: 0031-9163. URL: https://www.sciencedirect.com/science/article/pii/0031916362913690 (cit. on p. 1).

[Kel+15] J. Kelly et al. “State preservation by repetitive error detection in a superconducting quantum circuit”. In: *Nature* 519.7541 (Mar. 2015), pp. 66–69. ISSN: 1476-4687. DOI: 10.1038/nature14270 (cit. on p. 2).

[Kim08] H. J. Kimble. “The quantum internet”. In: *Nature* 453.7198 (June 2008), pp. 1023–1030. ISSN: 1476-4687. URL: https://doi.org/10.1038/nature07127 (cit. on p. 2).

[Kja+20] M. Kjaergaard et al. “Superconducting Qubits: Current State of Play”. In: *Annu. Rev. Condens. Matter Phys.* 11.1 (Mar. 2020), pp. 369–395. ISSN: 1947-5454. DOI: 10.1146/annurev-conmatphys-031119-050605 (cit. on p. 1).

[Koc+07] J. Koch et al. “Charge-insensitive qubit design derived from the Cooper pair box”. In: *Phys. Rev. A* 76.4 (Oct. 2007), p. 042319. DOI: 10.1103/PhysRevA.76.042319 (cit. on p. 2).

[Kos+20] J. Kosata et al. “Spin Detection via Parametric Frequency Conversion in a Membrane Resonator”. In: *Phys. Rev. Applied* 14.1 (July 2020), p. 014042. DOI: 10.1103/PhysRevApplied.14.014042 (cit. on p. 20).

[LR+21] D. Lago-Rivera et al. "Telecom-heralded entanglement between multimode solid-state quantum memories". In: *Nature* 594.7861 (June 2021), pp. 37–40. ISSN: 1476-4687. DOI: 10.1038/s41586-021-03481-8 (cit. on p. 3).

[Lal20] N. Lalic. *rohdeschwarz*. 2020. URL: https://github.com/Terrabits/rohdeschwarz (cit. on p. 52).

[Lec+15] F. Lecocq et al. "Resolving the vacuum fluctuations of an optomechanical system using an artificial atom". In: *Nature Physics* 11.8 (Aug. 2015), pp. 635–639. ISSN: 1745-2481. DOI: 10.1038/nphys3365 (cit. on p. 79).

[Liu+21] X. Liu et al. "Heralded entanglement distribution between two absorptive quantum memories". In: *Nature* 594.7861 (June 2021), pp. 41–45. ISSN: 1476-4687. URL: https://doi.org/10.1038/s41586-021-03505-3 (cit. on p. 3).

[MM14] J. M. Martinis and A. Megrant. "UCSB final report for the CSQ program: Review of decoherence and materials physics for superconducting qubits". In: *arxiv* (Oct. 21, 2014). arXiv: 1410.5793v1 [quant-ph] (cit. on p. 2).

[Mas+19] D. Mason et al. "Continuous force and displacement measurement below the standard quantum limit". In: *Nature Physics* 15.8 (Aug. 2019), pp. 745–749. ISSN: 1745-2481. DOI: 10.1038/s41567-019-0533-5 (cit. on p. 1).

[MMN03] T. Matsunaga, H. Maezawa, and T. Noguchi. "Characterization of NbTiN thin films prepared by reactive DC-magnetron sputtering". In: *IEEE Transactions on Applied Superconductivity* 13.2 (2003), pp. 3284–3287. ISSN: 1558-2515 (cit. on p. 29).

[Mi+17] X. Mi et al. "Strong coupling of a single electron in silicon to a microwave photon". In: *Science* 355.6321 (Jan. 2017), p. 156. DOI: 10.1126/science.aal2469. URL: http://science.sciencemag.org/content/355/6321/156.abstract (cit. on p. 2).

[Mir+20] M. Mirhosseini et al. "Superconducting qubit to optical photon transduction". In: *Nature* 588.7839 (Dec. 2020), pp. 599–603. ISSN: 1476-4687. DOI: 10.1038/s41586-020-3038-6 (cit. on pp. 3, 85).

[NPT99] Y. Nakamura, Y. A. Pashkin, and J. S. Tsai. "Coherent control of macroscopic quantum states in a single-Cooper-pair box". In: *Nature* 398.6730 (Apr. 1999), pp. 786–788. ISSN: 1476-4687. DOI: 10.1038/19718 (cit. on p. 1).

[Nie+14] M. Niedermayr et al. "Cryogenic surface ion trap based on intrinsic silicon". In: *New Journal of Physics* 16.11 (Nov. 2014), p. 113068. ISSN: 1367-2630. DOI: 10.1088/1367-2630/16/11/113068 (cit. on p. 30).

[NC10] M. A. Nielsen and I. L. Chuang. *Quantum Computation and Quantum Information*. Cambridge University Press, 2010 (cit. on p. 2).

[NBB19] D. Niepce, J. Burnett, and J. Bylander. "High Kinetic Inductance NbN Nanowire Superinductors". In: *Phys. Rev. Applied* 11.4 (Apr. 2019), p. 044014. DOI: 10.1103/PhysRevApplied.11.044014 (cit. on p. 57).

[Nog+16] A. Noguchi et al. "Ground state cooling of a quantum electromechanical system with a silicon nitride membrane in a 3D loop-gap cavity". In: *New Journal of Physics* 18.10 (Oct. 2016), p. 103036. DOI: 10.1088/1367-2630/18/10/103036 (cit. on pp. 15, 30).

[NMG16] R. A. Norte, J. P. Moura, and S. Gröblacher. "Mechanical Resonators for Quantum Optomechanics Experiments at Room Temperature". In: *Phys. Rev. Lett.* 116.14 (Apr. 2016), p. 147202. DOI: 10.1103/PhysRevLett.116.147202 (cit. on p. 2).

[Pag+20] M. A. Page et al. "Gravitational wave detectors with broadband high frequency sensitivity". In: *arxiv* (July 17, 2020). arXiv: 2007.08766v1 [physics.optics] (cit. on p. 86).

[Pal+13] T. A. Palomaki et al. "Coherent state transfer between itinerant microwave fields and a mechanical oscillator". In: *Nature* 495.7440 (Mar. 2013), pp. 210–214. ISSN: 1476-4687. DOI: 10.1038/nature11915 (cit. on p. 22).

[Per+14] M. Pernpeintner et al. "Circuit electromechanics with a non-metallized nanobeam". In: *Appl. Phys. Lett.* 105.12 (Sept. 2014), p. 123106. ISSN: 0003-6951. DOI: 10.1063/1.4896419 (cit. on p. 15).

[Per+20] M. Peruzzo et al. "Surpassing the Resistance Quantum with a Geometric Superinductor". In: *Phys. Rev. Applied* 14.4 (Oct. 2020), p. 044055. DOI: `10.1103/PhysRevApplied.14.044055` (cit. on p. 17).

[Pet+19] G. A. Peterson et al. "Ultrastrong Parametric Coupling between a Superconducting Cavity and a Mechanical Resonator". In: *Phys. Rev. Lett.* 123.24 (Dec. 2019), p. 247701. DOI: `10.1103/PhysRevLett.123.247701` (cit. on pp. 23, 30).

[Pro+15] S. Probst et al. "Efficient and robust analysis of complex scattering data under noise in microwave resonators". In: *Review of Scientific Instruments* 86.2 (Feb. 2015), p. 024706. DOI: `10.1063/1.4907935`. eprint: `https://doi.org/10.1063/1.4907935` (cit. on pp. 9, 81).

[Rab11] P. Rabl. "Photon Blockade Effect in Optomechanical Systems". In: *Phys. Rev. Lett.* 107.6 (Aug. 2011), p. 063601. DOI: `10.1103/PhysRevLett.107.063601` (cit. on p. 23).

[Rea+16] M. Reagor et al. "Quantum memory with millisecond coherence in circuit QED". In: *Phys. Rev. B* 94.1 (July 2016), p. 014506. DOI: `10.1103/PhysRevB.94.014506` (cit. on p. 2).

[Roc+21] F. Rochau et al. "Dynamical Backaction in an Ultrahigh-Finesse Fiber-Based Microcavity". In: *Phys. Rev. Applied* 16.1 (July 2021), p. 014013. DOI: `10.1103/PhysRevApplied.16.014013` (cit. on p. 2).

[RBS19] I. C. Rodrigues, D. Bothner, and G. A. Steele. "Coupling microwave photons to a mechanical resonator using quantum interference". In: *Nature Communications* 10.1 (Nov. 2019), p. 5359. ISSN: 2041-1723. DOI: `10.1038/s41467-019-12964-2` (cit. on p. 15).

[Ros+18] M. Rossi et al. "Measurement-based quantum control of mechanical motion". In: *Nature* 563.7729 (Nov. 2018), pp. 53–58. ISSN: 1476-4687. DOI: `10.1038/s41586-018-0643-8` (cit. on p. 84).

[Ros+19] M. Rossi et al. "Observing and Verifying the Quantum Trajectory of a Mechanical Resonator". In: *Phys. Rev. Lett.* 123.16 (Oct. 2019), p. 163601. DOI: `10.1103/PhysRevLett.123.163601` (cit. on p. 84).

[Rue+18] F. Ruesink et al. "Optical circulation in a multimode optomechanical resonator". In: *Nature Communications* 9.1 (May 2018), p. 1798. ISSN: 2041-1723. DOI: 10.1038/s41467-018-04202-y (cit. on p. 25).

[SN+11] A. H. Safavi-Naeini et al. "Electromagnetically induced transparency and slow light with optomechanics". In: *Nature* 472.7341 (Apr. 2011), pp. 69–73. ISSN: 1476-4687. DOI: 10.1038/nature09933 (cit. on p. 25).

[Sam+16] N. Samkharadze et al. "High-Kinetic-Inductance Superconducting Nanowire Resonators for Circuit QED in a Magnetic Field". In: *Phys. Rev. Applied* 5.4 (Apr. 2016), p. 044004. DOI: 10.1103/PhysRevApplied.5.044004 (cit. on pp. 17, 33).

[Sch+06] A. Schliesser et al. "Radiation Pressure Cooling of a Micromechanical Oscillator Using Dynamical Backaction". In: *Phys. Rev. Lett.* 97.24 (Dec. 2006), p. 243905. DOI: 10.1103/PhysRevLett.97.243905 (cit. on p. 2).

[Sch09] A. Schliesser. "Cavity optomechanics and optical frequency comb generation with silica whispering-gallery-mode microresonators". PhD thesis. Ludwig-Maximilians-Universität München, Oct. 2009. URL: https://www.nbi.dk/~aschlies/thesis.html (cit. on p. 25).

[Sei+21] Y. Seis et al. "Ground State Cooling of an Ultracoherent Electromechanical System". In: (July 12, 2021). arXiv: 2107.05552v2 [quant-ph] (cit. on pp. 74, 75).

[Sha+19] L. Shao et al. "Microwave-to-optical conversion using lithium niobate thin-film acoustic resonators". In: *Optica* 6.12 (Dec. 2019), pp. 1498–1505. URL: http://www.osapublishing.org/optica/abstract.cfm?URI=optica-6-12-1498 (cit. on p. 3).

[Shi+10] T. Shiino et al. "Improvement of the critical temperature of superconducting NbTiN and NbN thin films using the AlN buffer layer". In: *Superconductor Science and Technology* 23.4 (Mar. 2010), p. 045004. DOI: 10.1088/0953-2048/23/4/045004. URL: https://doi.org/10.1088%2F0953-2048%2F23%2F4%2F045004 (cit. on p. 29).

[Sim+19] A. Simonsen et al. "Sensitive optomechanical transduction of electric and magnetic signals to the optical domain". In: *Opt. Express* 27.13 (June 2019), pp. 18561–18578. URL: http://

www.opticsexpress.org/abstract.cfm?URI=oe-27-13-18561 (cit. on p. 20).

[Sin+14] V. Singh et al. "Optomechanical coupling between a multi-layer graphene mechanical resonator and a superconducting microwave cavity". In: *Nature Nanotechnology* 9 (Aug. 2014), p. 820. DOI: 10.1038/nnano.2014.168 (cit. on p. 17).

[Tak+18] K. Takeda et al. "Electro-mechano-optical detection of nuclear magnetic resonance". In: *Optica* 5.2 (Feb. 2018), pp. 152–158. URL: http://www.osapublishing.org/optica/abstract.cfm?URI=optica-5-2-152 (cit. on p. 20).

[Teu+11] J. D. Teufel et al. "Sideband cooling of micromechanical motion to the quantum ground state". In: *Nature* 475 (July 2011). carrier cancellation, p. 359. DOI: 10.1038/nature10261 (cit. on p. 2).

[Tho+08] J. D. Thompson et al. "Strong dispersive coupling of a high-finesse cavity to a micromechanical membrane". In: *Nature* 452.7183 (Mar. 2008), pp. 72–75. ISSN: 1476-4687. DOI: 10.1038/nature06715 (cit. on p. 2).

[Tia12] L. Tian. "Adiabatic State Conversion and Pulse Transmission in Optomechanical Systems". In: *Phys. Rev. Lett.* 108.15 (Apr. 2012), p. 153604. DOI: 10.1103/PhysRevLett.108.153604 (cit. on p. 84).

[Tsa+17] Y. Tsaturyan et al. "Ultracoherent nanomechanical resonators via soft clamping and dissipation dilution". In: *Nature Nanotechnology* 12 (June 2017), p. 776. DOI: 10.1038/nnano.2017.101 (cit. on pp. 2, 18, 33, 38, 70).

[Tuc+20] D. K. Tuckett et al. "Fault-Tolerant Thresholds for the Surface Code in Excess of 5% under Biased Noise". In: *Phys. Rev. Lett.* 124.13 (Mar. 2020), p. 130501. URL: https://link.aps.org/doi/10.1103/PhysRevLett.124.130501 (cit. on p. 2).

[Tó+17] L. Tóth et al. "A dissipative quantum reservoir for microwave light using a mechanical oscillator". In: *Nature Physics* 13.8 (Aug. 2017), pp. 787–793. ISSN: 1745-2481. URL: https://doi.org/10.1038/nphys4121 (cit. on p. 79).

[Val+19] F. Valenti et al. "Interplay Between Kinetic Inductance, Nonlinearity, and Quasiparticle Dynamics in Granular Aluminum Microwave Kinetic Inductance Detectors". In: *Phys. Rev. Applied* 11.5 (May 2019). quasi-particles, p. 054087. DOI: 10.1103/PhysRevApplied.11.054087 (cit. on p. 80).

[Vog+19] T. Vogt et al. "Efficient microwave-to-optical conversion using Rydberg atoms". In: *Phys. Rev. A* 99.2 (Feb. 2019), p. 023832. DOI: 10.1103/PhysRevA.99.023832 (cit. on p. 3).

[Wan+21] H. Wang et al. "Cryogenic single-port calibration for superconducting microwave resonator measurements". In: (Mar. 2, 2021). arXiv: 2103.01491v1 [quant-ph] (cit. on p. 60).

[Wei+10] S. Weis et al. "Optomechanically Induced Transparency". In: *Science* 330.6010 (Dec. 2010), p. 1520. URL: http://science.sciencemag.org/content/330/6010/1520.abstract (cit. on pp. 25, 95).

[Wil+09] D. J. Wilson et al. "Cavity Optomechanics with Stoichiometric SiN Films". In: *Phys. Rev. Lett.* 103.20 (Nov. 2009), p. 207204. DOI: 10.1103/PhysRevLett.103.207204 (cit. on p. 64).

[WR08] I. Wilson-Rae. "Intrinsic dissipation in nanomechanical resonators due to phonon tunneling". In: *Phys. Rev. B* 77.24 (June 2008), p. 245418. URL: https://link.aps.org/doi/10.1103/PhysRevB.77.245418 (cit. on p. 64).

[Xi09] X. X. Xi. "MgB2thin films". In: *Superconductor Science and Technology* 22.4 (Mar. 2009), p. 043001. ISSN: 1361-6668. URL: http://dx.doi.org/10.1088/0953-2048/22/4/043001 (cit. on p. 48).

[Xu+19] M. Xu et al. "Frequency-tunable high-Q superconducting resonators via wireless control of nonlinear kinetic inductance". In: *Appl. Phys. Lett.* 114.19 (May 2019), p. 192601. ISSN: 0003-6951. DOI: 10.1063/1.5098466 (cit. on pp. 33, 57, 80).

[YPR12] P.-L. Yu, T. P. Purdy, and C. A. Regal. "Control of Material Damping in High-Q Membrane Microresonators". In: *Phys. Rev. Lett.* 108 (8 Feb. 2012), p. 083603. DOI: 10.1103/PhysRevLett.108.083603 (cit. on pp. 2, 19, 38).

[YCS15] M. Yuan, M. A. Cohen, and G. A. Steele. "Silicon nitride membrane resonators at millikelvin temperatures with quality factors exceeding 108". In: *Appl. Phys. Lett.* 107.26 (Dec. 2015), p. 263501. ISSN: 0003-6951. DOI: `10.1063/1.4938747` (cit. on p. 63).

[Yua+15] M. Yuan et al. "Large cooperativity and microkelvin cooling with a three-dimensional optomechanical cavity". In: *Nat Commun* 6 (Oct. 2015), p. 8491. DOI: `10.1038/ncomms9491` (cit. on pp. 15, 30).

[Zeu+20] E. Zeuthen et al. "Figures of merit for quantum transducers". In: *Quantum Science and Technology* 5.3 (May 2020), p. 034009. ISSN: 2058-9565. DOI: `10.1088/2058-9565/ab8962` (cit. on p. 2).

[Zho+13] X. Zhou et al. "Slowing, advancing and switching of microwave signals using circuit nanoelectromechanics". In: *Nature Physics* 9.3 (Mar. 2013), pp. 179–184. ISSN: 1745-2481. DOI: `10.1038/nphys2527` (cit. on p. 25).

[Zho+19] X. Zhou et al. "On-chip Thermometry for Microwave Optomechanics Implemented in a Nuclear Demagnetization Cryostat". In: *Phys. Rev. Applied* 12.4 (Oct. 2019), p. 044066. DOI: `10.1103/PhysRevApplied.12.044066` (cit. on p. 63).

[Že+14] M. Žemlička et al. "Superconducting properties of magnesium diboride thin film measured by using coplanar waveguide resonator". In: *8th Solid State Surfaces and Interfaces* 312 (Sept. 2014), pp. 231–234. ISSN: 0169-4332. URL: `http://www.sciencedirect.com/science/article/pii/S016943321401263X` (cit. on p. 48).